

# **Dissipation and recovery in collagen fibrils: modelling and simulations**

*By*

**AMIR SUHAIL**

**PHYS10201704002**

**The Institute of Mathematical Sciences, Chennai**

*A thesis submitted to the*

*Board of Studies in Physical Sciences*

*In partial fulfilment of requirements*

*For the Degree of*

**DOCTOR OF PHILOSOPHY**

*of*

**HOMI BHABHA NATIONAL INSTITUTE**



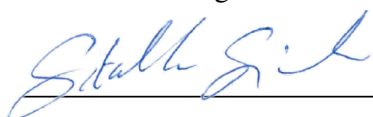
**31-07-2023**



# Homi Bhabha National Institute

## Recommendations of the Viva Voce Board

As members of the Viva Voce Board, we certify that we have read the dissertation prepared by Mr. Amir Suhail entitled "Dissipation and recovery in collagen fibrils: modelling and simulations" and recommend that it maybe accepted as fulfilling the dissertation requirement for the Degree of Doctor of Philosophy.



Date: 27/12/2023

Chair - Sitabhra Sinha



Date: 27/12/2023

Guide/Convener - Rajesh Ravindran



Date: 27/12/2023

Co-Guide - Anuradha Banerjee



Date: 27/12/2023

External Examiner - Jagannath Mondal



Date: 27/12/2023

Member 1 - Satyavani Vemparala



Date: 27/12/2023

Member 2 - Pinaki Chaudhuri



Date: 27/12/2023

Member 3 - Shrihari Gopalakrishna

Final approval and acceptance of this dissertation is contingent upon the candidate's submission of the final copies of the dissertation to HBNI.

I hereby certify that I have read this dissertation prepared under my direction and recommend that it may be accepted as fulfilling the dissertation requirement.

Date: 27/12/2023



Place: IMSc, Chennai

Guide - Rajesh Ravindran

Co-Guide- Anuradha Banerjee



## STATEMENT BY AUTHOR

This dissertation has been submitted in partial fulfilment of requirements for an advanced degree at Homi Bhabha National Institute (HBNI) and is deposited in the Library to be made available to borrowers under rules of the HBNI.

Brief quotations from this dissertation are allowable without special permission, provided that accurate acknowledgement of source is made. Requests for permission for extended quotation from or reproduction of this manuscript in whole or in part may be granted by the Competent Authority of HBNI when in his or her judgment the proposed use of the material is in the interests of scholarship. In all other instances, however, permission must be obtained from the author.



Amir Suhail



## DECLARATION

I, hereby declare that the investigation presented in the thesis has been carried out by me.  
The work is original and has not been submitted earlier as a whole or in part for a degree  
/ diploma at this or any other Institution / University.

  
Amir Suhail



## List of publications arising from the thesis

- Published

1. “Kinetic model description of dissipation and recovery in collagen fibrils under cyclic loading”, **Amir Suhail**, Anuradha Banerjee, R. Rajesh, Physical Review E **106**, 044407 (2022)

- Submitted

1. “Dissipation and recovery in collagen fibrils under cyclic loading: a molecular dynamics study”, **Amir Suhail**, Anuradha Banerjee, R. Rajesh, arXiv:2307.13465



### Contributed presentations

1. Oral presentation on *Kinetic model description of dissipation and recovery in collagen fibrils under cyclic loading* at **19th U.S. National Congress for Theoretical and Applied Mechanics** held in Austin, Texas, USA, June 19-24, 2022.
2. Oral presentation on *Kinetic model description of dissipation and recovery in collagen fibrils under cyclic loading* at **The 10th International Conference on Multiscale Materials Modeling** held in Baltimore, MD, USA, Oct 2-7, 2022.
3. Poster presentation on *Kinetic model description of dissipation and recovery in collagen fibrils under cyclic loading* at **Indian Statistical Physics Community Meeting-2023**, at ICTS, Bangalore Feb 1-3, 2023.

## Conferences and workshops attended

1. **Indian Statistical Physics Community Meeting** - 2023, at ICTS, Bangalore.
2. **Frontiers in non-equilibrium physics** - 2023, at IMSc, Chennai.
3. **Thirsting for theoretical Biology (ONLINE)** - Jan 11-22, 2021 at ICTS Bangalore.
4. **Statistical Biological Physics: From Single Molecule to Cell (ONLINE)** Dec 7-18, 2020 at ICTS Bangalore.
5. **Statistical Physics of Machine Learning** 2020 - Jan 6-10,2020 at ICTS Bangalore.
6. **BANGALORE SCHOOL ON STATISTICAL PHYSICS - X**- June 17-27, 2019 at ICTS Bangalore.
7. **Workshop on Data Analysis and Machine Learning**- May 24-28, 2019 at IISER Tirupati, Andhra Pradesh
8. **Soft Matter Symposium**, 2019, held at Indian Institute of Technology Madras, Chennai Tamil Nadu.
9. **PySangamam**, 2018, a python conference held at Indian Institute of Technology Madras, Chennai Tamil Nadu.
10. **Soft Matter meeting**, 2018, held at SRM University, Chennai Tamil Nadu.



*To My Parents*



## ACKNOWLEDGEMENTS

I want to extend my heartfelt thanks to everyone who played a crucial role in making my PhD journey a success. First and foremost, I am sincerely grateful to my supervisor, Rajesh Ravindran, and my co-guide, Anuradha Banerjee, for their support, guidance, and invaluable contributions throughout this journey. The discussions with them and their feedback have been very insightful, elevating the overall quality of my work and helping me grow as a researcher. I also want to thank David Cesar Malaspina for the very helpful discussion during early days of my Ph.D.

I would like to extend my thanks to my doctoral committee members: Prof. Sitabhra Sinha, Prof. Satyavani Vemparala, Prof. Pinaki Chaudhuri, and Prof. Shrihari Gopalakrishna, for their useful comments and encouragement, which have played a role in broadening my research perspectives. I also had several useful discussions with Prof. Satayani Vemparala and Prof. Purusattam Ray.

I would like to acknowledge the excellent high-performance computing facilities at IMSc and the very supportive administration. I am also thankful to the non-academic staff for all their help in making our lives comfortable at IMSc.

I would like to express my gratitude to all my friends. Playing badminton and participating in various sports at IMSc has been a source of great joy and bonding. The Institute trips have been a source of immense fun and wonderful memories.

Finally, to my family, I want to extend my deepest thanks for your constant love, encouragement, patience, and belief in me. You have been my pillar of strength throughout this journey.

Thank you all!



# Contents

<b>Synopsis</b>	<b>1</b>
<b>1 Introduction</b>	<b>15</b>
1.1 Collagen: Types, Biosynthesis and Significance . . . . .	15
1.2 Hierarchical structure of collagen . . . . .	17
1.3 Mechanical behaviour of collagen molecules and individual fibrils . . . . .	21
1.4 Computational modeling of collagen molecules and individual fibrils . . . . .	23
1.5 Research gap and problem statement . . . . .	27
1.6 Thesis organisation . . . . .	29
<b>2 Simulation techniques</b>	<b>31</b>
2.1 Molecular dynamics Simulation . . . . .	31
2.1.1 Introduction . . . . .	31
2.1.2 Interactions . . . . .	32
2.1.3 Time integration of equation of motion . . . . .	35
2.1.4 Periodic boundary conditions . . . . .	35

2.1.5	Thermostats and barostats . . . . .	36
2.2	Kinetic Monte Carlo Simulation . . . . .	38
<b>3</b>	<b>Kinetic model description of dissipation and recovery in collagen fibrils under cyclic loading</b>	<b>41</b>
3.1	Model . . . . .	42
3.1.1	Kinetic model formulation . . . . .	42
3.1.2	Determination of stress-stretch relation . . . . .	44
3.1.3	Determination of parameters and rates . . . . .	47
3.1.4	Simulation Protocol . . . . .	51
3.2	Results . . . . .	51
3.2.1	Uniaxial loading . . . . .	51
3.2.2	Cyclic loading . . . . .	52
3.3	Conclusions and Discussion . . . . .	58
<b>4</b>	<b>Dissipation and recovery in collagen fibril under cyclic loading: a molecular dynamics study</b>	<b>65</b>
4.1	Model . . . . .	67
4.1.1	Geometry of the collagen fibril model . . . . .	67
4.1.2	Interaction potential and parameters: . . . . .	69
4.1.3	Simulation protocol: . . . . .	72
4.2	Results . . . . .	73
4.2.1	Uniaxial and cyclic loading of fibril model with no-reformation: . . . . .	73

4.2.2	Role of cross-link reformation on fibril recovery . . . . .	81
4.3	Discussion and Conclusions . . . . .	83
<b>5</b>	<b>Conclusions</b>	<b>90</b>



# Synopsis

## Introduction

Collagen, the most abundant protein in vertebrates, is found in several hard and soft tissues, such as, bones, tendons, ligaments, cartilage etc. It plays a vital role in providing mechanical support, strength, flexibility, and mobility to the human body [1]. There are approximately 29 identified types of collagen based on the supramolecular structures, including fibril-forming collagen, network-forming collagen, fibril-associated collagen with interrupted triple helix, transmembrane collagen, and others. Type I collagen, known for forming fibrils, is the most abundant among all collagen types. Each collagen type contributes to tissue integrity and function: for instance, type I provides support and flexibility to bones, tendons, and skin; Type II supports joints; Type V is involved in fibrillation, etc. [2]. Collagen has a hierarchical structure with tropocollagen as the fundamental protein molecule. The diverse mechanical behavior of collagen based tissues is a direct consequence of the differences in their hierarchical structures. Understanding the mechanical properties of collagen at different length scales is not only essential to gain a comprehensive understanding of biological tissues but also crucial for various biomedical applications like tissue engineering, wound healing, drug delivery, disease diagnosis, treatment optimization and monitoring, etc. [3,4].

Collagen molecules, typically of length  $\approx 300$  nm, self assemble in a staggered manner to form collagen fibrils of diameters ranging between 10s to 100s of nm. The staggered arrangement of collagen molecules creates periodically repeating gap and overlap regions

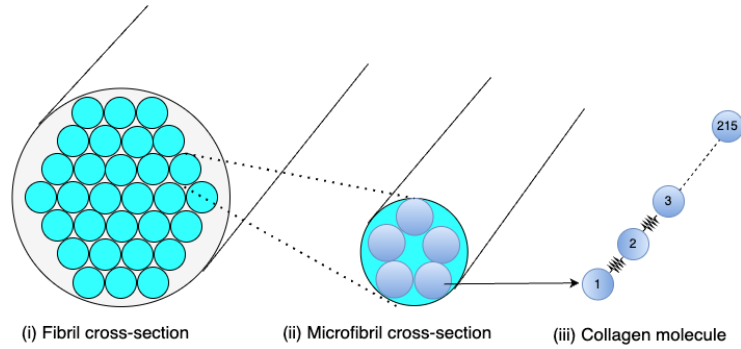


Figure 1: Cross-sectional view of hierarchical structure of the fibril: (i) fibril, (ii) microfibril, and (iii) molecule.

along the length of the fibril, giving rise to the characteristic D-period ( $67 \text{ nm}$ ) of the fibril. The fibril structure is further stabilized by intermolecular enzymatic covalent cross-linking (ECL) that form at the non-helical ends (telopeptides). The cross-sectional view of collagen fibril hierarchy is shown in Fig 1.

The mechanical response of collagen has been studied at various length scales in experiments. The molecular basis of toughness of collagenous tissues was established by identifying the basic mechanisms of energy dissipation during pulling of collagen molecules using atomic force microscopy [5]. The force extension response shows multiple drops, which were attributed to breaking of sacrificial bonds and release of hidden lengths. When a time delay was introduced between pulling cycles, partial recovery was observed, suggesting the reformation of sacrificial bonds. At the collagen molecule's length scale, X-ray diffraction has directly linked sacrificial bonds or crosslinks to the folding back of the molecule at the C-terminal telopeptides [6].

The mechanical response of the fibril depends on several factors like source of the specimen, hydration, environmental condition, extent and type of cross-links, and pH, etc.. The collagen fibrils from human patella tendon exhibit a characteristic three phase stress-strain behavior. An initial rise in modulus followed by a plateau and in the final phase further increase in stresses and modulus, hypothesized to be a consequence of maturity of cross-links, before final failure. A similar three phase behaviour has also been observed in fibril from calf skin [7]. Simulations at multiple length scales have provided interesting

insights into various aspects of deformation and failure of collagen ranging from atomistic length scales, focusing on individual tropocollagen molecules, to continuum length scales for collagen fibrils. Using atomistic simulations, the influence of hydration, mineralisation, viscoelastic properties, heterogeneity, etc. has been addressed at the molecular and microfibril scales. The role of cross-link density, including enzymatic and advanced glycation end-products cross-links, degradation, and mineralisation on the stress-strain response has also been studied using full three dimensional coarse grain models of collagen fibrils.

## **Research gap and problem statement**

Collagen is subjected to cyclic loads during exercise and routine body movements. While the response of collagen to monotonically increasing loads is comprehensively investigated, the response to cyclic loads, resulting dissipation, and recovery are comparatively much less studied. In a recent study, Liu et. al. [7] conducted displacement controlled cyclic loading experiments on single collagen fibrils obtained from calf skin, within all three regimes of stress strain response of fibril. The collagen fibrils were subjected to 10 cycles of loading up to a predetermined stretch ratio,  $\lambda_{max}$ , followed by unloading to zero force. This loading protocol is referred to as series 1 loading. Subsequently, the fibrils were allowed to relax for 1 hour. After relaxation, the fibrils underwent another 10 loading cycles with the same  $\lambda_{max}$ , referred to as series 2 loading. Finally, the fibrils were monotonically loaded until they reached final failure. The stress-stretch response of fibrils showed energy dissipation, moving hysteresis loops and associated residual strains. With increasing number of loading cycles, the dissipation of energy during hysteresis decreases while the residual strain increases and both finally saturate to their respective steady state values. Collagen fibrils also showed recovery in residual strain and as well as in capacity to dissipate energy when allowed to relax at zero force. These observations led to the hypothesis that reformable sacrificial bonds within the fibrils may be responsible for these

characteristics. Furthermore, the cyclically loaded fibrils exhibited greater strength and toughness compared to fibrils subjected to monotonic loading. This enhancement was believed to be due to permanent molecular rearrangements, although the specific mechanism behind these improvements was not fully understood.

In the thesis, we aim to comprehensively model and understand the mechanical response of single collagen fibrils under cyclic loading. In the first part of the study, we develop a minimal kinetic model for a collagen fibril incorporating presence of hidden loops and stochastic fragmentation as well as reformation of sacrificial bonds. This model effectively explains and qualitatively reproduces experimental features, including moving hysteresis loops, the time evolution of residual strain, and recovery on relaxation. In the second part of the thesis, we approach the problem from a microscopic perspective, utilizing existing molecular dynamics models [8,9] to account for experimental observations during cyclic loading. We also incorporate the reformation of cross-links in our model to evaluate its potential in explaining recovery and the increase in strength that may result from cross-link reorganisation. We show that the coarse grained model is also able to describe well the experimental data.

## **Kinetic model description of dissipation and recovery in collagen fibrils under cyclic loading**

The kinetic model [10] is a generic dynamical model that incorporates the role of sacrificial bonds, assuming that the sacrificial bonds result in regions of the polymer not being loaded. When these bonds break, there is a sudden drop in load as the hidden length is released, as shown in Fig 2. The experimental observations, like moving hysteresis loops and residual strain accumulation, were thought to be related to the presence of sacrificial bonds within the collagen fibril. Based on this hypothesis, we ask if a suitably formulated kinetic model can explain the observed experimental features. Within the framework of

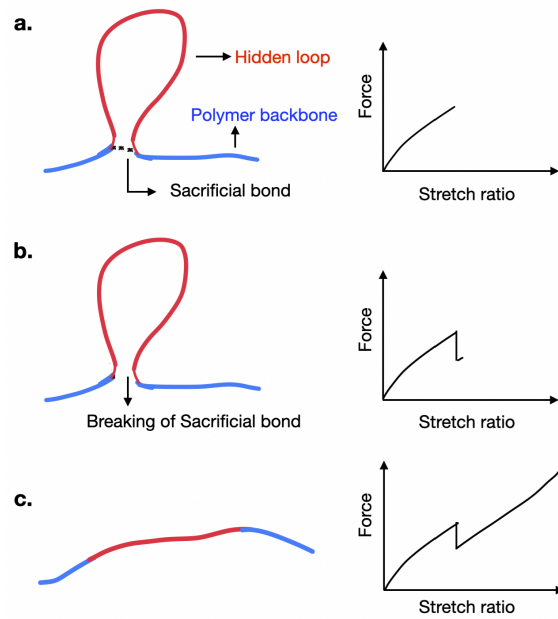


Figure 2: (a) Schematic of a polymer with a single sacrificial bond (dotted line), corresponding hidden loop (shown in red) and the corresponding force-stretch ratio response. (b) As the sacrificial bond breaks, the force drops due to release of the hidden length. (c) Force rises again as the polymer is extended further.

the kinetic model, we treat the collagen fibril as a linear polymeric chain that has hidden lengths secured by sacrificial bonds. The two primary ingredients of the model are: a reference stress-stretch relation for the available length of the polymer and stochastic formation and fragmentation of sacrificial bonds. The reference stress-stretch relation is first established from molecular dynamics simulations of an existing coarse-grain fibril model [9]. The kinetic model incorporates formation and breakage of sacrificial bonds and the corresponding release of hidden lengths at force-dependent rates based on Bell's theory. We estimated the model parameters by comparing with available experimental data and used kinetic Monte Carlo methods to simulate the cyclic loading experiment.

Our model qualitatively reproduces the main features of the experiment such as time evolution of hysteresis loops, energy dissipation, peak stress and residual strain etc. It is shown that these quantities approach their respective steady states exponentially with the number of loading cycles. We find that the characteristic cycle number associated with this exponential decay is in close agreement with the characteristic cycle number extracted

from the reported experimental data. The breaking of sacrificial bonds is responsible for hysteresis (energy dissipation) and the corresponding release of hidden lengths appears as residual strain. The magnitude of hysteresis, peak stress and residual strain after first cycle is proportional to maximum stretch ratio  $\lambda_{max}$ . The recovery of the fibril is proportional to the relaxation time and spontaneous formation and breaking of sacrificial bonds at zero force is a possible healing mechanism in the collagen fibril. The presence of a characteristic cycle number has significance in the description of the time dependent cyclic response of collagen. In particular, it has the potential of being utilised for comparison of fibril response across animals, ages, stages of disease, level of hierarchy, response to medication, etc. This is a promising area for future experimental investigation.

Kinetic model captures the essential physics and explain the key features of cyclic loading experiment of a single collagen fibril. However, it does not explain the increase in strength of the fibril post cyclic loading as observed in the experiment. It is a minimal model and does not account for complex geometrical structure of collagen fibril. To address this, our next step is to explore a microscopic model of collagen fibrils that incorporates dynamical sacrificial bonds (cross-links).

## **Dissipation and recovery in collagen fibrils under cyclic loading: a molecular dynamics study**

In this part of thesis, we approach the problem of cyclic loading of individual collagen fibril from microscopic point view. The aim of this work is to understand the molecular mechanism of deformation and recovery during cyclic loading. We first utilise the existing molecular dynamics models, specifically [9] to account for observed experimental features. We then extend this model to incorporate the reformation of cross-links or sacrificial bonds that aid in recovery and evaluate its potential to explain experimental findings such as recovery upon relaxation and increased strength that may result from cross-link

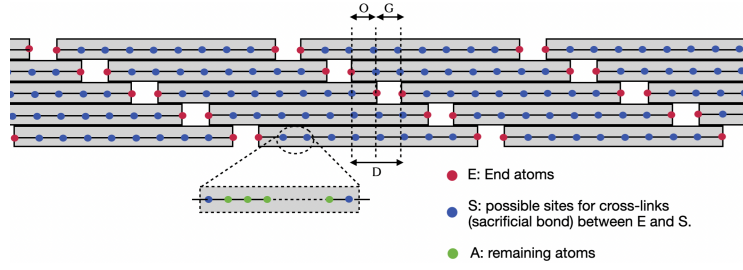


Figure 3: Schematic diagram showing the longitudinal arrangement of collagen molecules in a microfibril. Gap and overlap region represented by 'G' and 'O' respectively and D-period is shown by 'D'.

reformation and reorganisation.

In our model, each collagen molecule within a fibril is modeled as a bead spring polymer with three types of beads: end beads (designated as cross-linker beads E), potential cross-linking sites (S), and normal beads (A), as shown in Fig 3. Specifically, the E-S cross-links can be reformed during the relaxation period based on distance criteria. We use molecular dynamics simulations to mimic cyclic loading experiments by deforming the simulation box at a constant strain rate.

The model reproduces the key features of the experiment such as moving hysteresis loops, residual strains, peak stress and partial recovery on relaxation. The material parameters after relaxation were shown improve with relaxation bringing out the role of extent of cross-linking in determining the macroscopic response. The different parameters of the macroscopic response, such as peak stress, residual strain, dissipation, and number of cross-links approach the steady state values exponentially fast, characterized by a characteristic cycle number  $c^*$ . This behavior is consistent with what was observed in the analysis of the kinetic model as well as seen in the experiment [7]. We found that the  $c^*$ , becomes independent of the  $\lambda_{\max}$ , approximately equal to 5, when  $\lambda_{\max}$  lies within the regions where cross-links break, while it remains high at the lower boundary of this region. This observation is further supported by the dependence of  $c^*$  on cross-link density  $\beta$ . Further, the value of  $c^* \approx 5$  is same as that obtained for the kinetic model as well as in the experiment.

We investigate the post-cyclic loading recovery of the fibril model by allowing the fibril to relax and permitting cross-links to reform during the relaxation process. We observe  $\approx 50\%$  recovery in residual strain across different stretch ratios, comparable with the results of the experiment [7]. We do not find full recovery, thus there is presumably plastic deformation. This is because cross-links form while the strain is reducing at zero force, thereby arresting further decrease in strain. Plastic deformation is consistent with the viscoelastic-plastic modeling approach of Ref. [11], and the experimental results [7], but different from the kinetic model where full recovery occurs if the fibril is relaxed for infinite time as no geometrical constraints are accounted for in the kinetic model. To study the effect of cross-link reformation during relaxation, we compared the response to monotonic loading of two fibrils: one was subjected to monotonic loading immediately after cyclic loading, while the other was relaxed and then subjected to monotonic loading. We demonstrate an increase in strength and toughness in the fibril that underwent relaxation compared to the fibril that is not relaxed. The recovery is quantified and is shown to be more for larger stretch ratios  $\lambda_{\max}$ .

# List of Figures

1	Cross-sectional view of hierarchical structure of the fibril: (i) fibril, (ii) microfibril, and (iii) molecule. . . . .	2
2	(a) Schematic of a polymer with a single sacrificial bond (dotted line), corresponding hidden loop (shown in red) and the corresponding force-stretch ratio response. (b) As the sacrificial bond breaks, the force drops due to release of the hidden length. (c) Force rises again as the polymer is extended further. . . . .	5
3	Schematic diagram showing the longitudinal arrangement of collagen molecules in a microfibril. Gap and overlap region represented by 'G' and 'O' respectively and D-period is shown by 'D'. . . . .	7
1.1	The hierarchical structure of collagen. Amino acids are the basic units of collagen molecule which then assemble into fibril to form fibers and higher tissues like tendons, bones, etc [28]. Used with permission from Nano Letters. . . . .	17
1.2	Simplified structure of collagen fibril. Used with permission from [35]. . . . .	19

1.3	(A) Cross-sectional view of fibril. (B) D-staggered collagen molecule segment shown in crystallographic unit cell. (C) Collagen Microfibril (D) Non-helical telopeptide regions of collagen molecule [40]. Copyright (2006) by The National Academy of Sciences of the USA. (E) Schematic of the U-shape folded conformation of telopeptides during cross-link formation [6, 41]. Used with permission from Journal of the Mechanical Behavior of Biomedical Materials. . . . .	20
1.4	(A) The three phase stress-strain response of collagen fibril from human patella tendon on tensile loading [50], adopted with permissions from Biophysics Journal. (B). The stress-strain response of the collagen fibril from calf skin on tensile loading also shows typical three phase behaviour [7], adapted with permission from Acta Biomaterialia. . . . .	22
1.5	Overview of multiscale modelling approach for (a) collagen molecules and (b) collagen fibrils/microfibrils. . . . .	25
1.6	(a) Stress-stretch response of the collagen fibril on cyclic loading within regime II. (b) Zoomed version of point (a). (c) Evolution of residual or inelastic strain (d) Elastic modulus (e) Hysteresis (energy dissipation) with the number of loading cycle for both series 1 and series 2 loading [7]. Adapted with permission from Acta Biomaterialia. . . . .	28
2.1	Lenard-Jones potential. . . . .	34
3.1	(a) Schematic of a polymer with a single sacrificial bond (dotted line), corresponding hidden loop (shown in red) and the corresponding force-stretch ratio response. (b) As the sacrificial bond breaks, the force drops due to release of the hidden length. (c) Force rises again as the polymer is extended further. . . . .	43

3.2	(a) Cross-sectional view of coarse grained MD model of collagen fibril. (b) Cross-sectional view of a single microfibril. (c) A single collagen molecule as a bead spring linear polymer. . . . .	44
3.3	Stress-stretch relation $\sigma(\lambda)$ obtained from MD simulations of a fibril in which breakage of bonds (including backbone and other enzymatic cross-links) is disallowed. The data is fitted to a polynomial of degree nine. The $x$ -axis has been shifted to ignore the knee region. . . . .	45
3.4	(a) Schematic of evolution of available length during a series of cycles followed by relaxation at zero force. (b) Relaxation dynamics of fibril of length $L_c$ (with no sacrificial bonds). At long time fibril equilibrates to initial experimental length $L_{a,0}$ . Relaxation curve averaged over 1000 runs. . . . .	46
3.5	(a) The mean stress-strain response of the polymer under monotonic loading obtained using kinetic model. It shows three distinct regions which are roughly demarcated by the vertical dotted lines. $\lambda_1^{max}$ , $\lambda_2^{max}$ and $\lambda_3^{max}$ correspond to the maximum strain applied in the three different cyclic loading protocols. (b) The mean number of sacrificial bonds for a given strain for monotonic loading. . . . .	50
3.6	The macroscopic stress-stretch response for cyclic loading for (a) $\lambda^{max} = 1.1$ (region-I), (b) $\lambda^{max} = 1.2$ (region-II), and (c) $\lambda^{max} = 1.3$ (region-III). In all the three cases, the response shows moving hysteresis loops which saturate with loading cycles for both series 1 (first 10 cycles) and series 2 (next 10 cycles after 60 minutes relaxation at $F = 0$ ) loading. . . . .	50

3.7	The variation of number of sacrificial bonds with loading cycles for both series 1 and series 2 and for different stretch ratios, $\lambda^{max}$ . The dashed line corresponds to discontinuity due to relaxation before series 2 loading. After relaxation, there is a partial recovery in number of sacrificial bonds for all $\lambda^{max}$ . Color scheme used for cycles is same as in Fig. 3.6 . . . . .	53
3.8	The evolution of residual strain with number of loading cycles for both series 1 and series 2 for different stretch ratios, $\lambda^{max}$ . The magnitude and final saturated value of residual strain depends on the maximum stretch ratio, $\lambda^{max}$ . . . . .	54
3.9	The evolution of energy dissipation with number of loading cycles for both series 1 and series 2 and for different stretch ratios, $\lambda^{max}$ . The data from 2nd cycle onward is zoomed and shown in the inset figure. . . . .	55
3.10	The variation of the deviation of (a) residual strain and (b) area of hysteresis loop from their respective steady state values with number of loading cycles. The corresponding experimental data from Liu et. al. (2018) [7] are shown with squares. Both quantities approaches steady state exponentially. The best fits are shown by dashed lines. . . . .	56
3.11	The variation of characteristic cycle $c^*$ with the maximum stretch ratio, $\lambda^{max}$ obtained for (a) residual strain and (b) energy dissipation. . . . .	56
3.12	The variation of peak stress with number of loading cycles for different $\lambda_1^{max}$ , before (series 1) and after relaxation (series 2). Peak values of stress depends on $\lambda^{max}$ and show a partial recovery on relaxation (series 2). . . . .	57
3.13	Elastic modulus $E_1$ remains invariant to cyclic loading for both series and in all three regions while $E_2$ (for region-II and III) becomes constant after first cycle and then remains invariant to cyclic loading. . . . .	58

4.1	(a) Schematic diagram showing the longitudinal arrangement of collagen molecules in a microfibril. Gap and overlap region represented by 'G' and 'O' respectively and D-period is shown by 'D'. (b) Cross-sectional view of the hierarchical structure of the fibril: (i) fibril, (ii) microfibril, and (iii) molecule. . . . .	68
4.2	The stress-strain response of the collagen fibril model to applied uniaxial strain for different percentages of cross-links ( $\beta$ ) present. Data are averaged over 5 independent runs for each curve for same initial configurations.	74
4.3	The number of cross-links at a given uniaxial strain for different percentages of cross-links ( $\beta$ ) present. The red dots represent stretch ratios corresponding to peak stress in Fig. 4.2. Data are averaged over 5 independent runs for each curve for same initial configurations. . . . .	75
4.4	The stress-strain response of the collagen fibril model for strain controlled cyclic loading of a typical realization with $\beta = 100\%$ and maximum stretch ratio $\lambda_{\max} = 1.36$ . . . . .	75
4.5	Time evolution of the number of cross-links under cyclic loading, corresponding to the stress-strain response shown earlier in Fig. 4.4. . . . .	76
4.6	The average number of broken cross-links per cycle under cyclic loading, based on ten runs. . . . .	77
4.7	The evolution of residual strain with the number of loading cycles, averaged over ten runs. . . . .	77
4.8	The evolution of energy dissipation with the number of loading cycles, averaged over ten runs. . . . .	78
4.9	The variation of peak stress with the number of loading cycles, averaged over ten runs. . . . .	78

4.10	The variation of characteristic cycle, $c^*$ with the maximum stretch, $\lambda_{\max}$ . For the MD model, $c^*$ extracted from $\sigma_{\max}$ , residual strain and dissipation are shown. The stretch ratios for the kinetic model data and experimental data have been rescaled and are as reported in Ref. [97]. . . . .	80
4.11	The variation of characteristic cycle, $c^*$ , extracted from $\sigma_{\max}$ , with the cross-link percentage, $\beta$ , for $\lambda_{\max} = 1.345$ . . . . .	80
4.12	Time evolution of (a) number of cross-links and (b) stretch ratio for during relaxation at zero force after 10 cycles for different $\lambda_{\max}$ . . . . .	82
4.13	Comparison of (a) peak stress, $\sigma_{\max}$ and (b) toughness of a fibril subjected to monotonic loading with and without relaxation after being loaded for 10 cycles. Cross-links reform during the relaxation process. . . . .	83
4.14	Comparison of (a) residual strain (b) total number of cross-links of a fibril subjected to monotonic loading with and without relaxation after being loaded for 10 cycles. Cross-links reform during the relaxation process. . . . .	84
4.15	The (a) residual strain, (b) hysteresis, (c) peak stress and (d) number of broken bonds per cycle approach their respective steady state values ex- ponentially fast. The data are for $\lambda_{\max} = 1.36$ . . . . .	88
4.16	(a) The stress strain response (b) evolution of energy dissipation and (c) number of broken cross-links per cycle (d) residual strain under cyclic loading for $\lambda_{\max} = 1.35$ . . . . .	89

# Chapter 1

## Introduction

### 1.1 Collagen: Types, Biosynthesis and Significance

Collagen is the most abundant protein in vertebrates. It is found in several load-bearing tissues like bones, teeth, tendons, ligaments, and in other tissues like skin, eyes cornea, etc [1, 2]. Currently, there are approximately 29 identified types of collagen based on the supramolecular structures formed by collagen molecules. These types include fibril-forming collagen, network-forming collagen, fibril-associated collagen with interrupted triple helix (FACIT), transmembrane collagen, and others [2, 12]. Type I collagen, which forms fibrils, is the most abundant among all collagen. Each collagen type consists of a triple helical region at the fundamental level, which is made up of three alpha chains. There are approximately 25 alpha chains that combine in triplet and give rise to around 29 different types of currently known collagen [13]. Each collagen type contributes to the structural integrity, strength, and proper functioning of specific tissues within the body. For example, Type I collagen provides structural support, strength, and flexibility to tissues such as the skin, bones, and tendons. Type II collagen plays a crucial role in providing support to joints, type V plays a role in fibrillation, etc. [2, 14, 15]. The most common types of collagen along with their tissue distribution are summarized in Table 1.1.

	Type	Molecular formula	Polymerized form	Tissue distribution
<b>Fibril-Forming (fibrillar)</b>	I	$[\alpha 1(I)]_2\alpha 2(I)$	fibril	bone, skin, tendons, ligaments, cornea (represent 90% of total collagen of the human body)
	II	$[\alpha 1(II)]_3$	fibril	cartilage, intervertebral disc, notochord, vitreous humor in the eye
	III	$[\alpha 1(III)]_3$	fibril	skin, blood vessels
	V	$[\alpha 1(V)]_2\alpha 2(V)$ and $\alpha 1(V)\alpha 2(V)\alpha 3(V)$	fibril (assemble with type I)	same as type I
	XI	$\alpha 1(XI)\alpha 2(XI)\alpha 3(XI)$	fibril (assemble with type II)	same as type II
<b>Fibril-associated</b>	IX	$\alpha 1(IX)\alpha 2(IX)\alpha 3(IX)$	lateral association with type II fibril	cartilage
	XII	$[\alpha 1(XII)]_3$	lateral association with type I fibril	tendons, ligaments
<b>Network</b>	IV	$[\alpha 1(IV)]_2\alpha 2(IV)$	Sheet-like network	basal lamina
	VII	$[\alpha 1(VII)]_3$	anchoring fibrils	beneath stratified squamous epithelia

Table 1.1: Most common collagen types and their tissue distribution, taken from Ref. [13].

Collagen biosynthesis occurs in specialized cells called fibroblasts and is a complex process that involves several intra and extracellular processes [16, 17]. It involves transcription and translation of collagen genes to form pre-procollagen molecules inside the cell, and post-translational modifications. These modifications include removal of the signal peptide, hydroxylation of lysine and proline residues, and glycosylation. The modified pro-alpha chains assemble into a triple helix to form procollagen and transported outside the cell, where the ends of the procollagen are cleaved by enzymes called collagen peptidases, resulting in the formation of tropocollagen. These tropocollagen molecules then self-assemble to form fibrils.

Collagenous tissues exhibit a hierarchical structure, offering essential mechanical support, strength, flexibility, and mobility necessary for the optimal functioning of the human

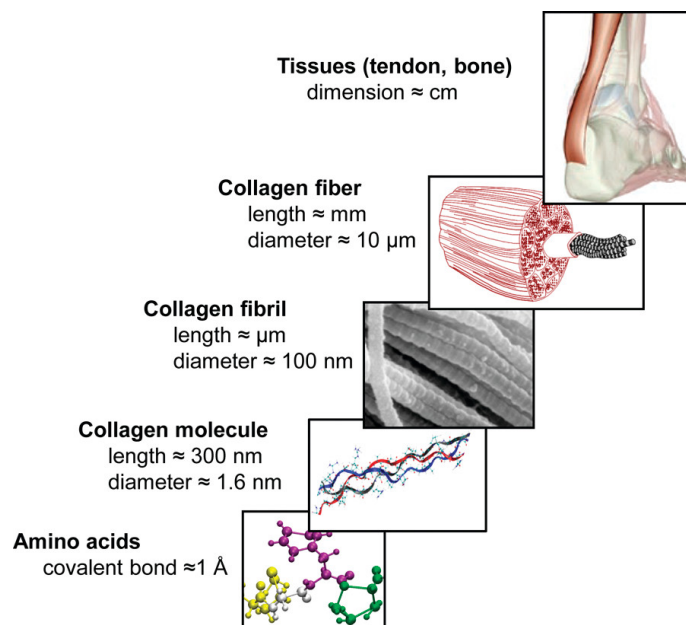


Figure 1.1: The hierarchical structure of collagen. Amino acids are the basic units of collagen molecule which then assemble into fibril to form fibers and higher tissues like tendons, bones, etc [28]. Used with permission from Nano Letters.

body. Collagen, being a key component in the extracellular matrix (ECM), also plays a vital role in cell behaviour [18], migration [19], differentiation [20], and wound healing [21] etc. However, mutations in the amino acid sequence of collagen can have significant implications on the mechanical properties at all scales [22, 23]. Such mutations have been associated with a range of diseases and conditions, including osteoporosis, osteogenesis imperfecta, Ehlers-Danlos syndrome, and more [24, 25]. It is important to understand the mechanical properties of collagen at all scale in order to gain comprehensive understanding of biological tissues [3, 26]. Understanding mechanical properties of collagen is also crucial for various biomedical application like tissue engineering, wound healing, drug delivery, disease diagnosis and monitoring, etc [4, 13, 27].

## 1.2 Hierarchical structure of collagen

The hierarchical structure of collagen is shown in Fig 1.1. Collagen molecules typically have a length of approximately 300nm and a diameter of around  $\approx 1.5nm$ . Each collagen

molecule consists of three left-handed polypeptide chains (*alpha* chains), which coil up along a common axis to form a right-handed triple helix. The composition of triple helix chains in collagen depends on the specific collagen type, which can be either a homotrimer or a heterotrimer. In the case of collagen type I, which is the primary focus of this thesis, it is a heterotrimer composed of two  $\alpha_1$  chains and one  $\alpha_2$  chain. The sequence of alpha chains in the triple helix is characterized by repeating units of Gly-X-Y, where X and Y frequently consist of proline and 4-hydroxyproline amino acids, respectively [29]. The stability of the triple helix is attributed to the presence of glycine at every third residue, along with hydrogen bonding and electrostatic interactions involving lysine residues [30]. Apart from the central major helical region, collagen molecules have two short non-helical regions called N and C telopeptides at both ends. These telopeptides are remnants left after the cleavage of propeptides during biosynthesis [6, 17].

At the next level of hierarchy, tropocollagen molecules self-assemble to form long collagen fibrils with diameters ranging from tens to hundreds of nanometers. The simplified structure, as shown in Fig. 1.2, illustrates the packing of collagen molecules within a fibril along the longitudinal direction. These fibrils are further composed of multiple microfibrils, each consisting of five collagen molecular strands [31, 32]. Within a microfibril, the collagen molecules align in a staggered manner along a common axis, resulting in alternating regions of low and high density known as the gap and overlap regions, respectively [33, 34]. This staggered arrangement gives rise to the observed banding pattern in the collagen fibril with a periodicity of  $67nm$ . The lengths of the gap and overlap regions are  $0.54D$  and  $0.46D$ , respectively, where  $D$  ( $67nm$ ) represents the characteristic period equal to the sum of the gap and overlap regions.

The fibril structure is further stabilize by the formation of enzymatic cross-links between collagen molecules. The enzymatic reaction is initiate by the enzyme lysyl oxidase, which acts on specific lysine amino acids at the non-helical ends of a collagen molecule (N and C telopetides) [36]. The resulting allysine then reacts with a specific lysine of an

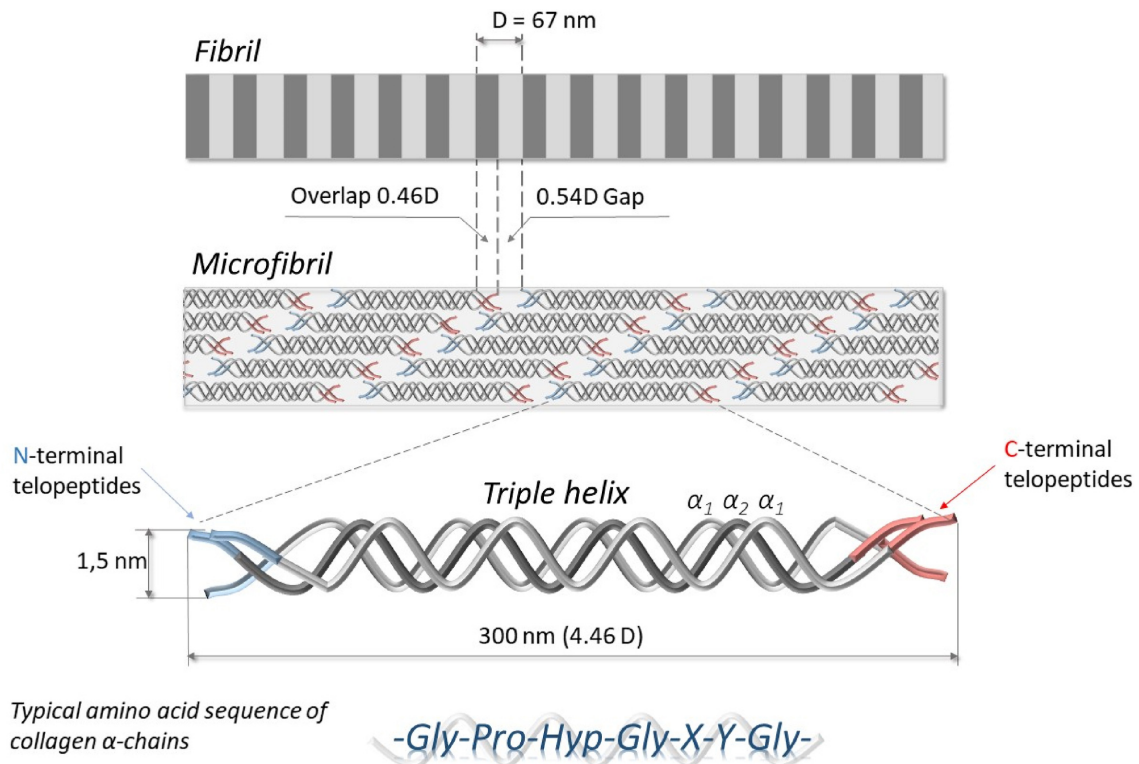


Figure 1.2: Simplified structure of collagen fibril. Used with permission from [35].

adjacent molecule, forming an immature divalent intermolecular bond [37]. With time, these divalent cross-links further react with another telopeptide aldehyde group to form a trivalent mature bond, linking three tropocollagen molecules together [38,39]. It has been shown using x-ray diffraction that these telopeptides take a folded conformation during cross-link formation [6].

The full crystallographic description of type I fibrillar collagen supermolecular structure was presented by Orgel et al. [40] in 2006, see Fig 1.3. This 3D model has become one of the most widely used and recognized models for the purpose of modeling and simulating fibrillar collagen. The collagen molecules are arranged in a quasi-hexagonal pattern when viewed in cross-section, forming the fibril (see Fig 1.3 A). Five collagen molecules are depicted within a single unit cell, representing a microfibril. The lateral arrangement of collagen molecules within a microfibril is not entirely straight; instead, the molecules exhibit kinks and wavy structures. Additionally, the collagen molecules are interdigitated into each other with a right-handed twist (as illustrated in Fig 1.3 C). Fig 1.3 D and E

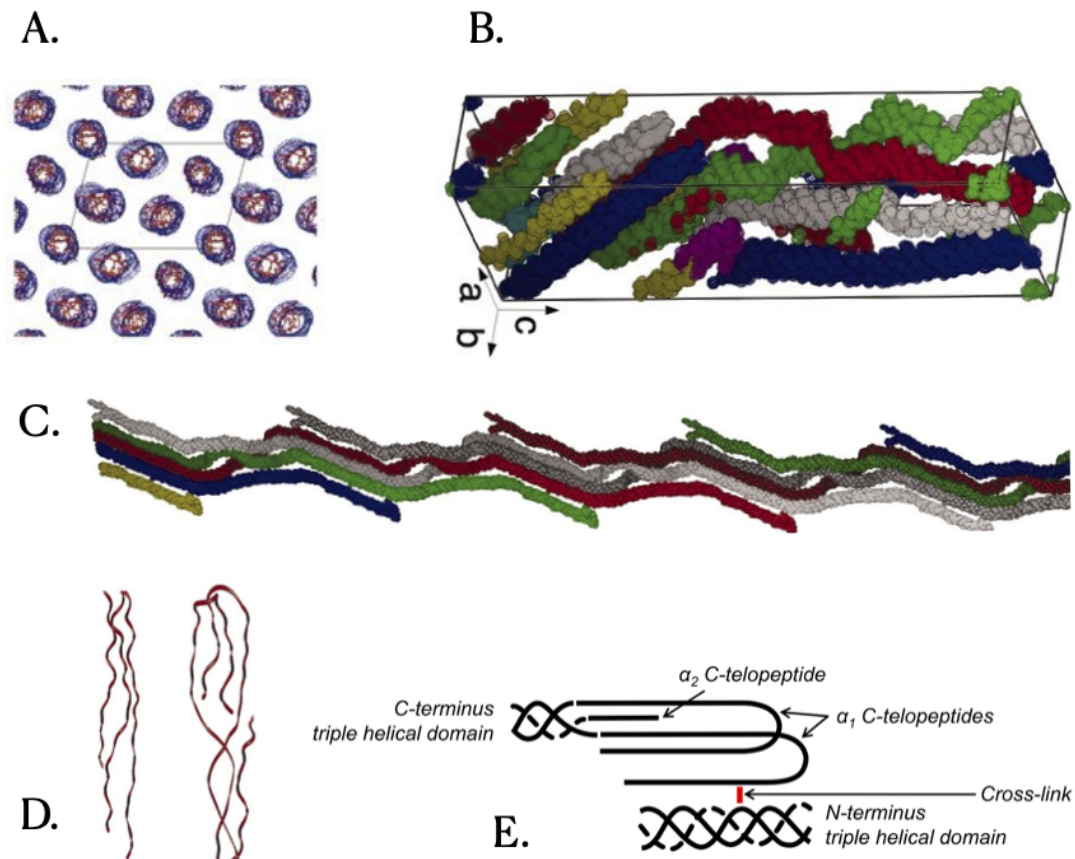


Figure 1.3: (A) Cross-sectional view of fibril. (B) D-staggered collagen molecule segment shown in crystallographic unit cell. (C) Collagen Microfibril (D) Non-helical telopeptide regions of collagen molecule [40]. Copyright (2006) by The National Academy of Sciences of the USA. (E) Schematic of the U-shape folded conformation of telopeptides during cross-link formation [6,41]. Used with permission from Journal of the Mechanical Behavior of Biomedical Materials.

illustrate the structure of telopeptides and schematic of their folded conformation during cross-link formation, respectively.

The structural organization of collagen is universal up to the collagen fibril level. However, beyond that point, diverse structural arrangements occur to accommodate the specific requirements of different tissues. For example, in tendons these collagen fibril forms fibers and then fascicles [42], mineralisation of fibrils occur in bones [43], forms highly ordered orthogonal array in cornea [44,45], etc. In this thesis, we focus on type I collagen.

### **1.3 Mechanical behaviour of collagen molecules and individual fibrils**

Collagen is known for its outstanding mechanical properties. At the smallest length scale, the mechanical response of the collagen molecules has been determined using AFM and optical tweezers experiments [5,46–49]. The molecular basis of the toughness of collagenous tissues was established by identifying the basic mechanisms of energy dissipation during the pulling of collagen molecules. Thompson et al. [5] conducted AFM experiments, pulling collagen molecules soaked in  $Ca^{+2}$  ions from a glass slab at a constant velocity and returning the tip to within 50 *nm* of the surface. The force-extension curve of bovine Achilles tendon collagen showed a saw-tooth pattern, with multiple force drops as extension increased. These drops were attributed to the rupture of intermolecular sacrificial bonds and the release of hidden lengths, ensuring backbone integrity while dissipating a significant amount of energy. Further, a delay of 100s before the next cycle was shown to result in an almost 50% recovery in the capacity of energy dissipation, suggesting reformation of the sacrificial bonds during the waiting interval. Sun et al. [46] used optical tweezers to pull single collagen molecules at small forces. The results fit well with the Worm-Like Chain (WLC) model, showing a persistence length of  $14.5 \pm 7.3$  *nm* and a contour length of  $309 \pm 41$  *nm*. The estimated elastic modulus from the persistence length

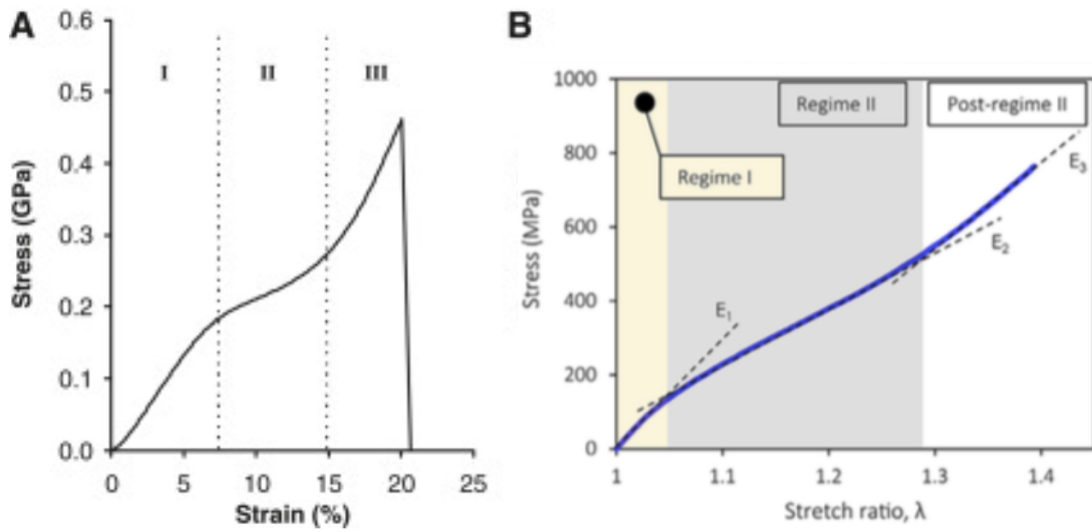


Figure 1.4: (A) The three phase stress-strain response of collagen fibril from human patella tendon on tensile loading [50], adopted with permissions from Biophysics Journal. (B). The stress-strain response of the collagen fibril from calf skin on tensile loading also shows typical three phase behaviour [7], adapted with permission from Acta Biomaterialia.

is between  $0.35 - 12 \text{ GPa}$ . Bozec et al. [48] performed force spectroscopy experiments on collagen molecules, and in 18% of their samples, they observed a discontinuity in the force-extension response. The region before the discontinuity fit well with the Worm-Like Chain (WLC) model, but beyond the discontinuity, it did not. This suggests that the curvature of the peak contains two mechanical behaviors, where the WLC model can effectively model one but not the other. This shows that collagen molecules exhibit entropic elasticity at lower forces and energetic elasticity at higher forces.

At the fibril scale, the mechanical properties of individual collagen fibrils have been primarily studied using experimental techniques such as Atomic Force Microscopy (AFM) [23, 50–52] and Microelectromechanical Systems (MEMS) [7, 53–55]. The mechanical response of the fibril depends on several factors like source of the specimen, hydration, environmental condition, cross-links density and pH, etc., [50, 51, 53, 54, 56, 57]. Svensson et. al. [50], studied the influence of enzymatic cross-links (ECLs) on the fracture mechanics of collagen fibrils upon tensile loading. The collagen fibrils from the human patella tendon exhibit a characteristic three-phase stress-strain behavior (Fig 1.4 A). It

begins with an initial rise in modulus, followed by a plateau, and in the final phase, experiences a further increase in stresses and modulus, hypothesized to be a consequence of the maturity of cross-links, before reaching failure [50]. In contrast, collagen from the rat tail tendon, a non-load bearing tissue, displays only two phases, with a plateau in the stress-strain leading to failure. Similarly, the collagen fibril from calf skin also demonstrates a typical three-phase behavior in the stress-strain response to tensile loading (Fig 1.4 B).

In addition to enzymatic cross-links (ECLs), Advanced Glycation Endproducts (AGEs) can also develop within the fibril through glycation reactions. Unlike ECLs, the precise location of AGEs within the collagen molecules is not yet fully known, but they form along the length of the collagen molecules. AGEs are known to occur as a result of aging and diabetes [58,59]. These cross-links contribute to the stiffening of the fibril but causing a loss of plasticity and toughness [60]. The degree of cross-linking, involving both ECLs and AGEs, between tropocollagen molecules has been shown to have a significant impact on the fibril's mechanical response [50,54,61,62].

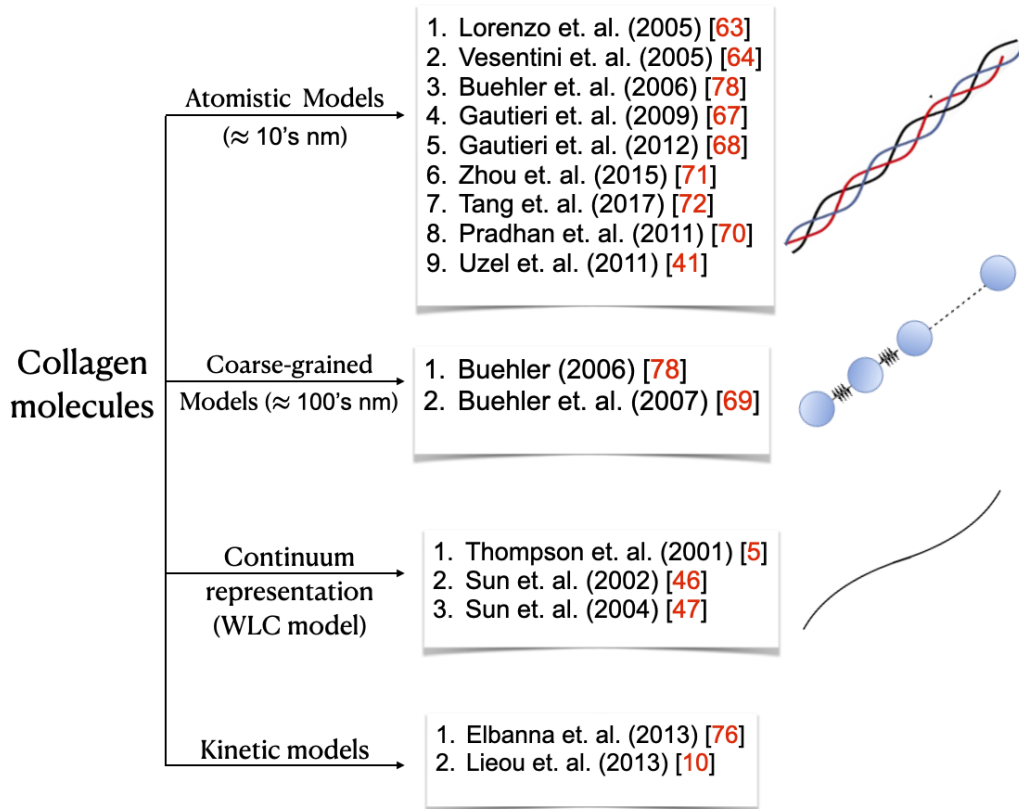
## **1.4 Computational modeling of collagen molecules and individual fibrils**

The modeling of collagen molecules and fibrils has been addressed at various length scales. In Fig. 1.5, we have illustrated an overview of the multiscale modeling approach. Simulations at multiple length scales have provided interesting insights into various aspects of deformation and failure of collagen, ranging from atomistic length scales, focusing on individual tropocollagen molecules, to continuum length scales for collagen fibrils [63–66]. These earlier simulations were based on short  $\approx 8nm$  collagen-like peptides from x-ray crystallography. At the level of tropocollagen molecules, three main deformation mechanisms are observed: molecular unwinding, breaking of hydrogen bonds, and

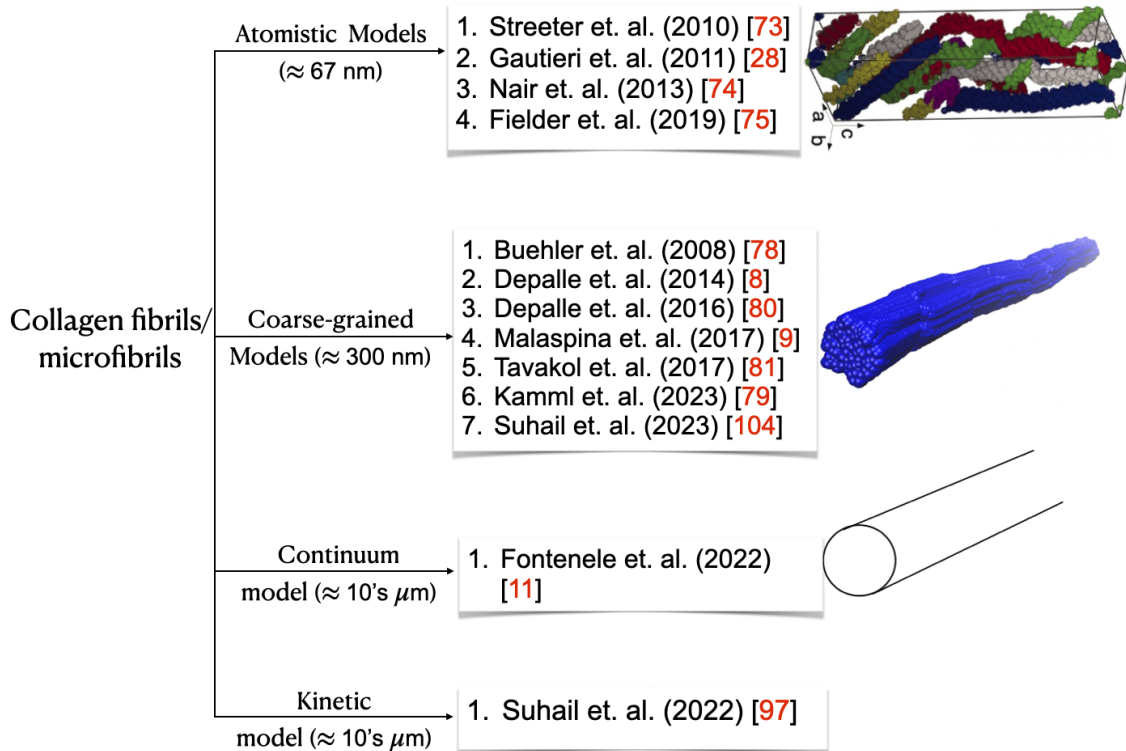
backbone stretching. The force-extension response of tropocollagen molecules depends on the deformation rate and also show viscoelastic behaviour [67,68]. Mesoscopic molecular model, derived from atomistic studies of tropocollagen, of ultra-long tropocollagen molecule showed the transition from entropic elasticity at small deformations to energetic elasticity at large deformations [69].

The pioneering work by Orgel et al. [40] in developing a full three-dimensional x-ray crystallographic model of the full-length collagen molecule and its molecular packing within microfibrils marked a significant advancement in collagen modeling and simulations. Subsequent studies have observed differences in the mechanical response between short and full-length collagen molecules [70]. To gain further insights, all-atom steered molecular dynamics simulations were used to investigate the mechanical properties of collagen molecule across different segments, revealing substantial heterogeneity along the length [71,72].

The full-length model of the collagen molecule serves as the foundation for constructing the microfibril model. By wrapping a single collagen molecule around in a crystallographic unit cell with periodic boundary conditions, it mimics the collagen microfibril or the core of the fibril [73]. This detailed atomistic model of the fibril core has proven instrumental in studying the role of various factors, such as hydration [28], mineralization [74], and their combined effects [75] on mechanical properties of the fibril. The dry microfibril exhibits a higher Young's modulus of approximately 1.8 – 2.25 GPa, compared to the hydrated state with around 1.2 GPa [28]. Notably, the microfibril's Young's modulus is approximately 10 times smaller than that of single molecules, highlighting the diversity in properties as a consequence of collagen's hierarchical structure. Uzel et. al. [41], incorporated the U-shaped enzymatic cross-link structure [6] between C-terminal segment from one molecule and helical segment from another molecule into an all-atomistic model. The chains with cross-links showed improved mechanical response. This U-shape structure has an equivalence with the structure of sacrificial bonds [76]. Additionally, the



(a)



(b)

Figure 1.5: Overview of multiscale modelling approach for (a) collagen molecules and (b) collagen fibrils/microfibrils.

mechanical properties of the fibril, such as tensile modulus and stress-bearing capability, have been found to increase with higher mineralisation density [74]. Moreover, increased hydration leads to stress-strain nonlinearity, but the presence of mineral content in hydrated fibrils reduces this effect during tensile stress [75].

The collagen molecules are long, with thousands of amino acids in each chain of the triple helix. It is computationally challenging to deal with more than one molecule with full atomistic details, making it impractical to simulate the entire fibril using atomistic simulations. Using mesoscopic molecular model with idealized two-dimensional representation of collagen fibril, large deformations without catastrophic failure were shown to be possible due to molecular stretching as well as other competing mechanisms such as intermolecular sliding and breaking of cross-links between collagen molecules [77]. Depalle et al. [8] proposed a more realistic coarse-grained model of collagen fibril, which considered the full three-dimensional structure of the fibril and incorporated enzymatic cross-links at their physiological locations. The parameters for this model were derived through a bottom-up approach from atomistic simulations of short collagen molecules in earlier studies [65, 69, 78]. By distinguishing between mature and immature cross-link properties, the model successfully reproduced the three-phase stress-strain response observed in experiments [50]. A similar molecular dynamics (MD) simulations of a three-dimensional model explored the effects of degradation on the overall mechanical response of the fibril [9]. The study considered three types of degradation, including surface, volume, and cross-link removal, and demonstrated that even with minor degradation, significant changes in mechanical properties were observed, highlighting the importance of molecular organization in collagen fibrils. Recently, there have been advancements in modelling collagen fibrils by incorporating advanced glycation end-products (AGEs) in addition to enzymatic (ECLs). A high content of the AGEs led to an increase in the strength of the fibril, but it fails abruptly because of backbone failure and doesn't dissipate much energy through cross-link breakage [79]. The degree of cross-linking, including both ECLs and AGEs between tropocollagen molecules, has been shown to have a

significant impact on the material's mechanical response [50, 54, 61, 62, 79]. The extent of the mineralisation also enhance mechanical properties of the fibril [80, 81].

## 1.5 Research gap and problem statement

Collagen is subjected to cyclic loads during various body movements and physical activities, such as exercise and everyday motion. While the response of collagen to monotonically increasing loads is comprehensively investigated, the response to cyclic loads, resulting dissipation, and recovery are comparatively much less studied, ranging from single fibril scale [7, 52, 55, 82] to macroscopic tissue length scale [83–87]. For isolated collagen fibril, Shen et. al. [55] performed fatigue test on isolated collagen fibrils and reported four different stress-strain response: linear to failure, perfectly plastic, perfectly plastic-strain hardening, and nonlinear strain softening. All fibrils exhibited significant hysteresis and a residual strain (strain at zero force). A recovery in residual strain was also observed, which was dependent on the amount of time spent at zero force. Similar features have also been observed in experiments at tissue length scale [85, 86].

In a recent experimental study, Liu et. al. [7] conducted displacement controlled cyclic loading experiments on single collagen fibrils obtained from calf skin, within all three regimes (see Fig 1.4 B) of the stress-stretch response. The stress-stretch reponse of fibril on cyclic loading within regime II is shown in Fig. 1.6. The collagen fibrils were subjected to 10 cycles of loading up to a predetermined stretch ratio,  $\lambda_{max}$ , followed by unloading to zero force. This loading protocol is referred to as series 1 loading. Subsequently, the fibrils were allowed to relax for 1 hour. After relaxation, the fibrils underwent another 10 loading cycles with the same  $\lambda_{max}$ , referred to as series 2 loading. Finally, the fibrils were monotonically loaded until they reached final failure. The stress-stretch response of fibrils showed energy dissipation, moving hysteresis loops and associated residual strains (Fig. 1.6 a). With increasing number of loading cycles, the dissipation during hysteresis

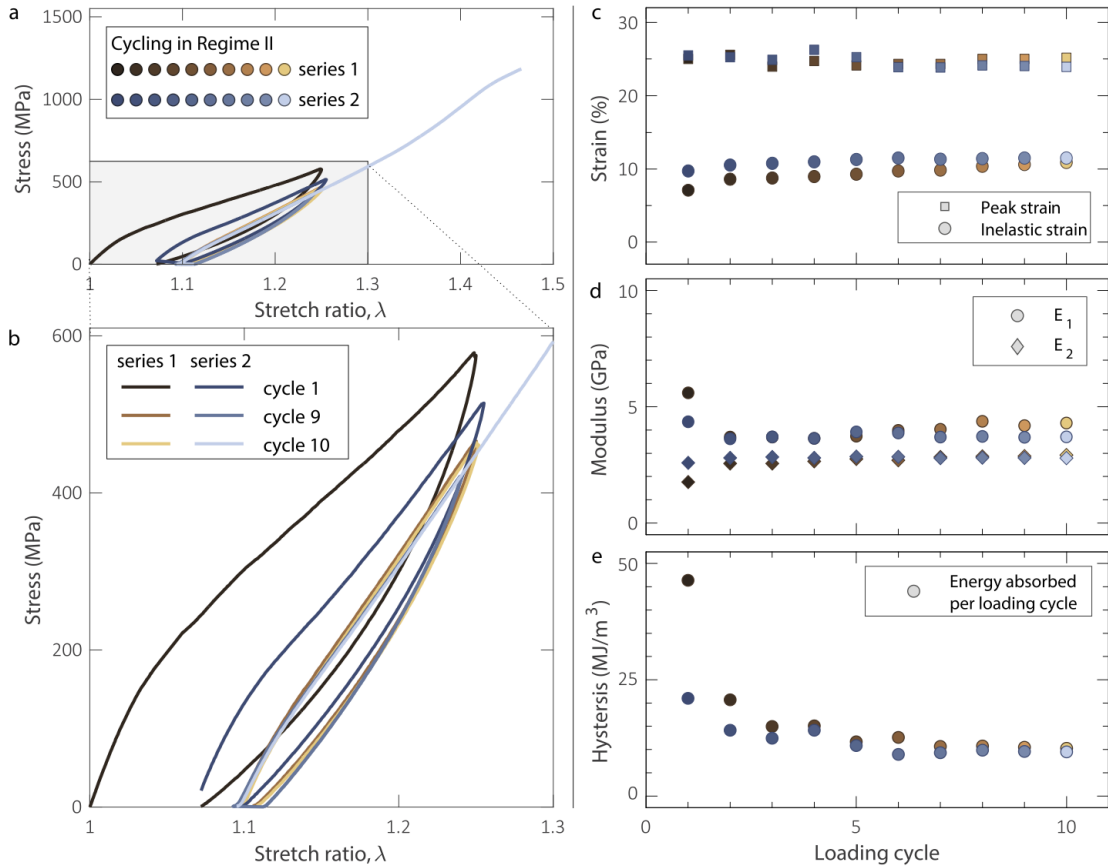


Figure 1.6: (a) Stress-stretch response of the collagen fibril on cyclic loading within regime II. (b) Zoomed version of point (a). (c) Evolution of residual or inelastic strain (d) Elastic modulus (c) Hysteresis (energy dissipation) with the number of loading cycle for both series 1 and series 2 loading [7]. Adapted with permission from Acta Biomaterialia.

decreases while the residual strain increases and both finally saturate to their respective steady state values. Collagen fibrils also showed recovery in residual strain and as well as in capacity to dissipate energy when allowed to relax at zero force (Fig. 1.6 c, e). It was conjectured that these features could be due to the existence of reformable sacrificial bonds within the fibrils. Finally, the fibrils which were cyclically loaded showed an increase in strength and toughness, compared to monotonically loaded fibrils. However, the exact mechanism responsible for these enhancements remains unknown and is speculated to involve permanent molecular rearrangements within the fibril structure. With respect to modeling cyclic response of collagen, there are recent advances in understanding of the energy dissipation and wave propagation properties of collagen at molecular, microfibril level due to transient loading using fully atomistic models [88–90] and continuum constitutive model [11].

## 1.6 Thesis organisation

This thesis is organised into five chapters. In this chapter, we provide an overview of collagen, its biosynthesis, and its significance. We also explore the hierarchical organization of collagen, drawing insights from experimental studies and computer simulations. As we proceed, we focus our attention on the central research problem of this thesis, which is to comprehensively model and understand the response of a single collagen fibril under cyclic loading conditions.

In Chapter- 2, we have briefly introduced the tools used in this thesis to perform simulations. We discuss the fundamentals of molecular dynamics simulations, covering aspects such as interaction potentials, boundary conditions, thermostats, etc. We also discuss another important simulation technique called kinetic Monte Carlo simulations and its principles and applications.

In Chapter- 3, we introduce kinetic model formalism and develop a kinetic model for

a collagen fibril, incorporating hidden loops, stochastic fragmentation, and reformation of sacrificial bonds. Model reproduces characteristic features observed in experimental data, including moving hysteresis loops, time evolution of residual strains and energy dissipation, and recovery on relaxation. The approach to the steady state is controlled by a characteristic cycle number for both residual strain and energy dissipation, aligning well with reported experimental data.

In Chapter- 4, we address the cyclic loading response of the fibril from a microscopic perspective by modifying an existing coarse-grained molecular dynamics model for collagen fibril. The model, initially with cross-linked collagen molecules, is extended to incorporate the reformation of cross-links, allowing for potential fibril recovery. We show that our model successfully replicates the key features observed in experimental data. In addition, it also provides an explanation for the non-zero steady-state hysteresis and plastic deformation observed in the experiment. We also show that the characteristic cycle number, describing the approach towards steady state, has a value similar to that in experiments and in the kinetic model. We also highlight the influence of the degree of cross-linking on key macroscopic response features to cyclic loading.

In Chapter- 5, we finally conclude the thesis with a comprehensive summary of the results obtained, followed by a discussion on the future directions and exploring how the results of this thesis can be extended for new advancements in the field.

# Chapter 2

## Simulation techniques

In this chapter, a brief introduction to both molecular dynamics (MD) simulations and kinetic Monte Carlo simulations is given. More details can be found in the Ref. [91–93]

### 2.1 Molecular dynamics Simulation

#### 2.1.1 Introduction

Molecular dynamics (MD) is a powerful computational technique for simulating the motion of particles interacting with each other via an interaction potential. MD provides useful insights into the structural dynamics, thermodynamics, and kinetics of many systems by performing simulations at the atomic scale. The fundamental principle of molecular dynamics simulations lies in solving Newton's equations of motion for each atom in the system. For example, consider a system of  $N$  particles interacting with each other with a potential  $U(\mathbf{r})$ . The force on  $i_{th}$  particle is given by

$$F_i = m_i \ddot{\mathbf{r}}_i = -\nabla_i U(\mathbf{r}), \quad (2.1)$$

where,  $m_i$  is the mass and  $\ddot{\mathbf{r}}_i$  is acceleration of the particle. By numerically integrating the above equations with appropriate boundary conditions and initial conditions over small time steps, one can follow the trajectories of atoms and obtain their positions and velocities at each time step, allowing the simulation of the system's behavior over time.

In the context of biological systems and materials science, molecular dynamics simulations have become an indispensable tool for understanding the behavior of complex biomolecules, such as proteins, and lipids, as well as the mechanical properties of materials like polymers, nanomaterials, etc. Here, we provide an overview of molecular dynamics simulations, including their underlying principles, force fields, integration methods, boundary conditions, etc.

### 2.1.2 Interactions

The interaction potential, also known as the force field, is a central component that governs the interactions between particles (atoms, molecules, or ions) in the simulated system. The interaction potential describes the potential energy associated with the pairwise interactions between particles, which influences their behavior and governs the dynamics of the system. The interaction potential typically consists of bonded and non-bonded interactions.

$$U = U_{bonded} + U_{non-bonded}, \quad (2.2)$$

The bonded interactions typically include bond stretching (bonded pairs of atoms moving closer or farther), angle bending (angular deformations around bond centers), and dihedral (torsional) rotations. These interactions are often described by harmonic or more complex potential functions. The non-bonded interactions includes Van der Waals interactions, electrostatic interaction, hydrogen bonding etc. The choice of potential or force field depends on the nature of the system. There are several known force fields used in atomic and molecular simulation such as CHARMM, AMBER, etc.

In the context of this thesis, collagen molecules are modelled as neutral bead-spring polymers. We have considered only bond stretching and angle bending in bonded interactions and the Van der Waals interactions using Lenard Jones potential for non-bonded pairs. The most general form of interaction potential for any neutral polymer is given below:

### **Bonded potential:**

The bond stretching potential energy function describes the interactions between the directly bonded beads. A common choice for bond stretching is the harmonic potential:

$$U_{\text{bond}}(r) = \frac{1}{2}k_{\text{bond}}(r - r_{\text{eq}})^2, \quad (2.3)$$

where,  $U_{\text{bond}}$  is the bond stretching potential energy,  $k_{\text{bond}}$  is the bond stretching force constant (bond stiffness),  $r$  is the current bond length, and  $r_{\text{eq}}$  is the equilibrium bond length. The bending potential energy function describes the interactions between three consecutive beads in a polymer and quantifies the energy associated with deviation of bond angle from its equilibrium value. A common choice for bending interaction is also the harmonic potential:

$$U_{\text{angle}}(\theta) = \frac{1}{2}k_{\text{angle}}(\theta - \theta_{\text{eq}})^2, \quad (2.4)$$

where,  $U_{\text{angle}}$  is the bending potential energy,  $k_{\text{angle}}$  is the bending force constant,  $\theta$  is the current bond angle, and  $\theta_{\text{eq}}$  is the equilibrium bond angle.

### **Non-bonded potential:**

The non-bonded interactions are typically modelled using the Lennard-Jones (LJ) potential for Van der Waals interactions and the Coulombic potential for electrostatic interactions. The LJ potential, as shown in Fig. 2.1, is widely used in molecular simulations to describe the non-bonded interactions between neutral atoms/beads. It captures both attractive Van der Waals forces and repulsive excluded volume effects. The potential is

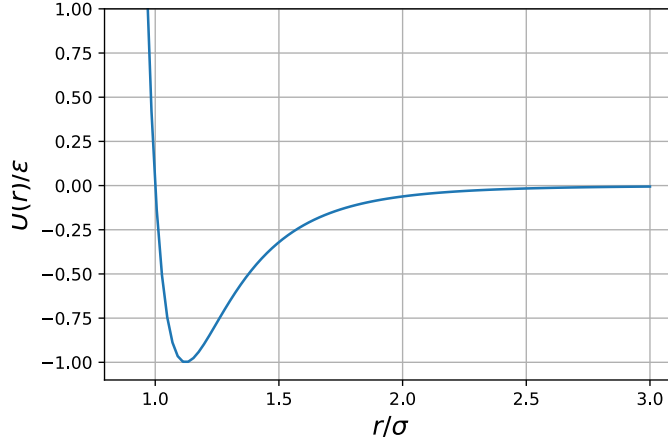


Figure 2.1: Lennard-Jones potential.

given by:

$$U_{\text{LJ}}(r_{ij}) = 4\epsilon \left[ \left( \frac{\sigma}{r_{ij}} \right)^{12} - \left( \frac{\sigma}{r_{ij}} \right)^6 \right], \quad (2.5)$$

where,  $U_{\text{LJ}}$  is the Lennard-Jones potential energy,  $\epsilon$  is the depth of the potential, determining the strength of the interaction,  $\sigma$  is the finite distance at which the inter-particle potential is zero (size of the bead), and  $r_{ij}$  is the distance between the centers of two interacting particles. The LJ potential has an attractive term ( $\propto r^{-6}$ ) dominating at large distances and a repulsive term ( $\propto r^{-12}$ ) dominating at short distances. The balance between these terms leads to a stable potential well at the equilibrium distance ( $r_{\text{min}} = 2^{1/6}\sigma$ ), representing the most stable configuration between particles with  $U_{\text{LJ}}(r_{\text{min}}) = -\epsilon$ . The Lennard-Jones (LJ) potential represents a long-range interaction between particles. To enhance computational efficiency, the potential is truncated at a cutoff distance of  $r_c = 2.5\sigma$ , beyond which the force is considered negligible, set to zero, and shifted ( $U_{\text{LJ}}(r) - U_{\text{LJ}}(r_c)$ ) to avoid discontinuity in potential energy at the cut-off distance.

### 2.1.3 Time integration of equation of motion

The equation of motion for system of N interacting particles can be written as:

$$m_i \ddot{\mathbf{r}}_i = \sum_{i \neq j} \mathbf{F}_{ij}, \quad (2.6)$$

where,  $m_i$  is the mass of  $i_{th}$ ,  $r_i$  is the position of particle and  $F_{ij}$  force between  $i_{th}$  and  $j_{th}$  particle. These equations of motion are solved using an integrator to determine the positions and velocities of particles. One of the most used integrator in molecular dynamics simulations is the velocity-Verlet algorithm [94]. It has an error of the order of  $\delta t^4$ , where  $\delta t$  is the time step. At time  $t + \delta t$ , the velocity-Verlet algorithm update the positions and velocities as follows:

$$\mathbf{r}_i(t + \delta t) = \mathbf{r}_i(t) + \mathbf{v}_i(t)\delta t + \frac{\mathbf{F}_i(t)}{2m_i}\delta t^2, \quad (2.7)$$

$$\mathbf{v}_i(t + \delta t) = \mathbf{v}_i(t) + \frac{\delta t}{2m_i} (\mathbf{F}_i(t + \delta t) + \mathbf{F}_i(t)), \quad (2.8)$$

By iteratively applying these equations for each time step, the velocity-Verlet algorithm calculates the positions and velocities of particles, allowing the simulation to progress in time. This integrator ensures both accuracy and stability, preserving energy conservation and volume in phase space, making it a favored and widely adopted choice for Molecular Dynamics (MD) simulations.

### 2.1.4 Periodic boundary conditions

In Molecular Dynamics simulations, we often want to study the behavior of a system that is much larger than what we can directly simulate. However, simulating such a large system with billions of particles would be computationally impractical. Periodic Boundary Conditions (PBC) enable simulating a small box of particles, where particles that reach one edge reappear on the opposite side. This wraps the system around itself, creating

an effective simulation of an infinite system. PBC reduces edge or finite size effects and allows studying bulk properties accurately.

PBC, on the other hand, allows particles to interact not only within their own simulation box, but also with particles in periodic replica boxes, resulting in an endless series sum of interactions. The minimum image convention is used to simplify computations for systems having short-range interactions. This convention concentrates on interactions between a particle and its nearest neighbour or periodic image, effectively reducing the infinite series to a finite one and increasing the efficiency of the calculations. The interaction cutoff ( $r_c$ ) must be less than half the length of the box ( $L/2$ ) for appropriate results. We can effectively simulate short-range interactions using the minimum image convention without needing to include interactions with all particles in the system.

### **2.1.5 Thermostats and barostats**

In molecular dynamics simulations, when we simply integrate the equations of motion, we are essentially simulating the system in a microcanonical ensemble where the total energy is conserved. However, in many real-world scenarios, we are interested in simulating systems under different conditions, such as at a constant temperature or constant pressure, which correspond to the canonical (NVT) or isothermal-isobaric (NPT) ensembles, respectively. Various methods have been developed to achieve these conditions, allowing for simulations in the canonical (NVT) or isothermal-isobaric (NPT) ensembles. The following is a brief introduction to some of the most used methods.

#### **Langevin thermostat**

The Langevin thermostat introduces both a frictional force and a random force to the particle's momenta, ensuring that the simulation reaches and maintains the desired temperature. It utilizes stochastic forces to control the temperature of a particle moving in the presence bath of smaller particles. These smaller particles create a damping force,

represented by  $-\gamma_i p_i$ , where  $\gamma_i$  is the friction coefficient and  $p_i$  is the momentum of the  $i_{th}$  particle. Additionally, the kinetic energy of the smaller particles leads to random kicks given to the larger particle. In summary, the Langevin thermostat modifies the equations of motion for each particle as follows:

$$\frac{dp_i}{dt} = F_i - \gamma_i p_i + \eta_i(t), \quad (2.9)$$

where  $F_i$  is the force acting on atom  $i$  due to the interaction potential,  $\gamma_i$  is the damping factor (friction coefficient), and  $R_i(t)$  is a zero-averaged random force. The random force has the property:

$$\langle \eta_i(0)\eta_i(t) \rangle = 2m_i\gamma_i k_B T \delta(t), \quad (2.10)$$

where  $T$  is the desired temperature,  $k_B$  is the Boltzmann constant,  $m_i$  is the mass of the particle, and  $\delta(t)$  is the time-step. This thermostat is useful to mimic implicit solvent.

## Nose-Hoover thermostat

The Nose-Hoover thermostat, proposed by Nose [95] and further modified by Hoover [96]. This deterministic algorithm introduces an additional degree of freedom ( $s$ ), which mimic a heat bath. The extended Lagrangian of the system is given by:

$$L = \sum_{i=1}^N \frac{m_i s^2 \dot{q}_i^2}{2} - U(q) + \frac{Q \dot{s}^2}{2} - g k_B T \ln s, \quad (2.11)$$

where  $m_i$  is the mass of the  $i_{th}$  particle,  $q_i$  is its coordinate,  $Q$  is the mass associated with  $s$ ,  $g$  is the number of degrees of freedom of the system, and  $k_B$  is the Boltzmann constant. The equations of motion for the particles are then described by:

$$\frac{dq_i}{dt} = \frac{p_i}{m_i s^2}, \quad \frac{dp_i}{dt} = -\frac{\partial U}{\partial q_i}, \quad \frac{ds}{dt} = \frac{p_s}{Q}, \quad \frac{dp_s}{dt} = m_i s^2 \frac{B}{k_B T} - g k_B T, \quad (2.12)$$

## 2.2 Kinetic Monte Carlo Simulation

Kinetic Monte Carlo (KMC) simulation is a computational technique used to simulate the time evolution of complex processes in nature. Unlike molecular dynamics, which involves solving classical equations of motion and tracking individual atomic movements, KMC focuses on the stochastic behavior of macroscopic events and their probabilities. Its flexible time step adapts to different processes' timescales, enhancing computational efficiency. It is particularly useful for investigating the kinetics of processes that occur via random events and are influenced by probabilities, such as diffusion, adsorption, desorption, chemical reactions, etc. KMC simulations can handle large systems and long timescales, providing detailed information about the kinetics and non-equilibrium behavior of the system.

In KMC simulations, the system is represented by a network of discrete states, and transitions between these states occur probabilistically. Each state represents a specific configuration or arrangement of particles, and the transitions between states correspond to elementary processes or events that can take place in the system, such as breaking of a bond or diffusion of a particle, etc. The basic steps of a Kinetic Monte Carlo simulation are as follows:

1. **Initialization:** The initial state of the system is set up with a given configuration of particles.
2. **Events identification:** All possible elementary processes (events) that can occur in the current state are identified. These events could include diffusion of particles, chemical reactions, or other transformations.
3. **Rate calculation:** The rates of all individual events (e.g., a specific particle movement or a single reaction), denoted by  $k_i$  are calculated. These rates, in general, can depend on force, activation energy, temperature, etc. The sum of the rates of all

events is denoted by  $R$ , such that

$$R = \sum_i k_i, \quad (2.13)$$

4. **Time step:** An appropriate time step  $\Delta t$  is chosen to ensure that only one event occurs during each time step. A common approach is to set  $\Delta t$  based on the fastest event in the system, typically as:

$$\Delta t = \frac{0.1}{R}, \quad (2.14)$$

5. **Event Execution:** The probabilities ( $k_i \Delta t$ ) of all the events are calculated, and an event is selected based on a random number decision to be executed, and the system is updated according to the changes associated with that event. For example, particles may move to neighbouring lattice sites, undergo chemical reactions, or change their internal states.
6. **Time Update:** The simulation time is incremented by the generated time increment  $\Delta t$ .
7. **Repeat:** Steps 2 to 6 are repeated, generating a sequence of events and updating the system until a specified simulation time is reached or a certain number of events have occurred. This give a single trajectory of the system.



## Chapter 3

# Kinetic model description of dissipation and recovery in collagen fibrils under cyclic loading

The content of this chapter is published in Ref. [97].

This chapter aims to explain the key experimental features observed during cyclic loading experiments, as described in Sec 1.5. These features include the time evolution of hysteresis loops and residual strain, among others. They are thought to be connected to the presence of sacrificial bonds within the collagen fibril, forming the basis of our model's hypothesis. To achieve this, we adopt the kinetic model approach, which incorporates sacrificial bonds.

Dynamic sacrificial bonds within polymers have been successfully incorporated in simplified models called kinetic models. The saw-toothed stress-strain response of collagen molecules has been simulated using deterministic kinetic models of a worm-like chain with additional sacrificial bonds whose breakage results in the release of a hidden length, resulting in a drop in force [10, 76]. Historically, two state kinetic models have been used

to describe the force-extension response of single protein pulling experiments [98–100]. Here, within the framework of kinetic models, we develop a minimal stochastic kinetic model for collagen fibrils that incorporates dynamic reformable sacrificial bonds with hidden lengths. We show that the proposed model is able to reproduce the main qualitative features of the cyclic loading experiment [7], suggesting that the essential physics is captured by the kinetic model. By choosing realistic model parameters, we reproduce key quantitative features of the experimental data.

## 3.1 Model

### 3.1.1 Kinetic model formulation

We first describe the basis of kinetic models and how they incorporate the dynamic formation and breaking of sacrificial bonds. We then give the details of the specific kinetic model that we develop for simulating the cyclic response of a fibril.

Consider a linear polymer whose contour length, in the absence of sacrificial bonds, is  $L_c$ . Let bond length be  $b$  such that number of monomers are  $N = L_c/b$ . Each sacrificial bond creates a hidden loop that prevents a part of polymer backbone from taking any load, as shown schematically in Fig. 3.1. When hidden loops are present, the available length  $L_a$ , of the polymer backbone is less than  $L_c$  and is given by

$$L_a = L_c - \sum_i \ell_i, \quad (3.1)$$

where  $\ell_i$  is the length of the  $i$ th hidden loop. The length of the hidden loops are chosen from a distribution  $P(\ell)$ .

We denote the stress-stretch relation of the polymer by  $\sigma(\lambda)$ , where  $\lambda$  is the stretch (note that  $\lambda = 1 + \epsilon$ , where  $\epsilon$  is the strain). We assume that  $\sigma(\lambda)$  increases monotonically with

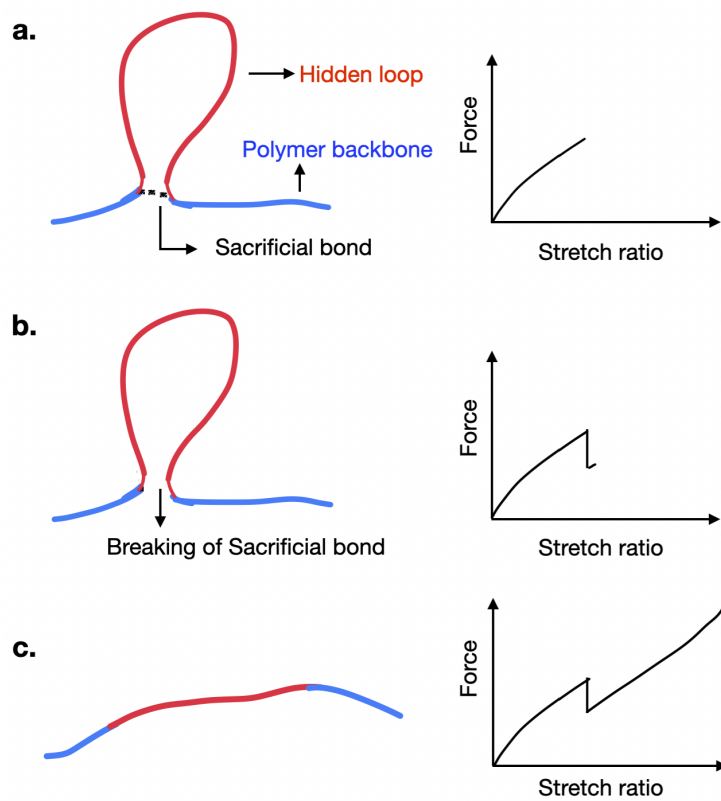


Figure 3.1: (a) Schematic of a polymer with a single sacrificial bond (dotted line), corresponding hidden loop (shown in red) and the corresponding force-stretch ratio response. (b) As the sacrificial bond breaks, the force drops due to release of the hidden length. (c) Force rises again as the polymer is extended further.

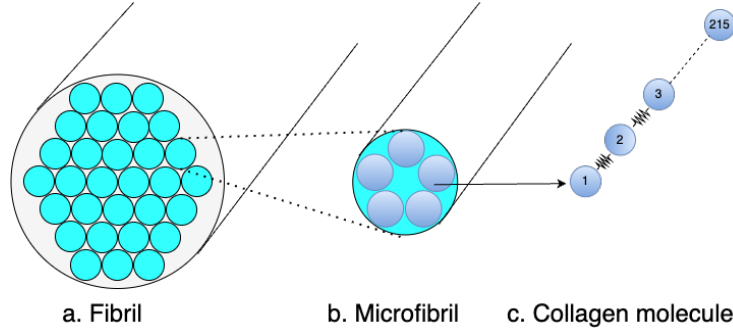


Figure 3.2: (a) Cross-sectional view of coarse grained MD model of collagen fibril. (b) Cross-sectional view of a single microfibril. (c) A single collagen molecule as a bead spring linear polymer.

$\lambda$ . Sacrificial bonds are created and broken with rates  $k_b$  and  $k_f$  which are in general dependent on the force acting on the polymer. For a given macroscopic extension, when a sacrificial bond is created,  $L_a$  decreases, thus increasing the strain, and hence the force. Similarly, when a sacrificial bond breaks,  $L_a$  increases, thus decreasing strain, and hence there is a drop in force. The rates of formation,  $k_b$ , and fragmentation,  $k_f$ , of sacrificial bonds have been earlier modeled [10], according to Bell's theory [101], as

$$k_f = \alpha_0 \exp\left(\frac{F\Delta x_f}{k_B T}\right), \quad (3.2)$$

$$k_b = \beta_0 \exp\left(\frac{-F\Delta x_b}{k_B T}\right), \quad (3.3)$$

where  $\alpha_0$  and  $\beta_0$  are rates of fragmentation and formation of sacrificial bonds at zero force,  $\Delta x_f$  and  $\Delta x_b$  are distances to transition state,  $F$  is the force felt by the sacrificial bond,  $k_B$  is the Boltzmann's constant and  $T$  is the temperature.

### 3.1.2 Determination of stress-stretch relation

We now describe the implementation of the kinetic model for a collagen fibril. A fibril consists of a collection of collagen molecules that are linked to each other through enzymatic crosslinks. Within the kinetic model framework, we treat the collagen fibril as a coarse grained linear polymer. The crosslinks are treated as dynamic sacrificial bonds

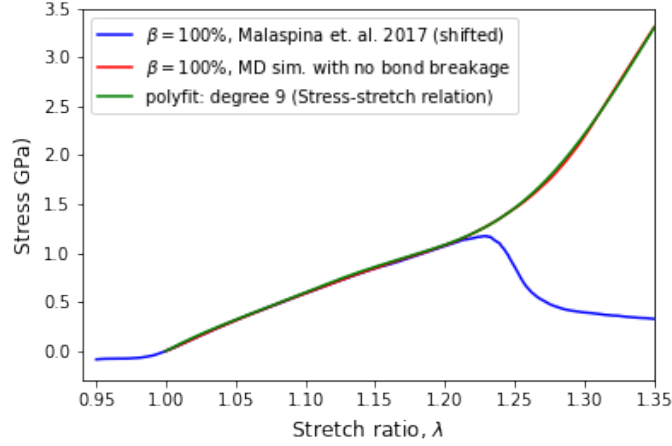


Figure 3.3: Stress-stretch relation  $\sigma(\lambda)$  obtained from MD simulations of a fibril in which breakage of bonds (including backbone and other enzymatic cross-links) is disallowed. The data is fitted to a polynomial of degree nine. The  $x$ -axis has been shifted to ignore the knee region.

that can be created or broken with rates described in Eqs. (3.2) and (3.3).

To first establish the stress-stretch response of collagen fibril without any creating or fragmentation dynamics, we use an existing coarse grained three dimensional MD model [9], but here we disallow any fragmentation of crosslinks. In the coarse grained MD model (as in Ref. [9]), shown schematically in Fig. 3.2, each collagen molecule is represented by a linear bead-spring model of 215 beads [see Fig. 3.2(c)]. To create a microfibril, five collagen molecules are arranged in a staggered manner along the longitudinal direction such that the arrangement is a pentagon in the cross-sectional view [see Fig. 3.2(b)]. A repeated hexagonal arrangement of multiple microfibrils forms a fibril [see Fig. 3.2(a)]. Within each microfibril, the collagen molecules are inter-connected through cross-links. We considered the case of hundred percent cross-linking ( $\beta = 100\%$ ), which implies that the terminal ends of all collagen molecules form crosslinks with neighbouring molecules. A detailed description of the model, the values of the parameters used, and details of simulation are provided in Appendix A.

The stress-stretch relation  $\sigma(\lambda)$ , where  $\lambda = x/L_a$  and  $x$  is the end-to-end distance of the polymer, obtained from MD simulations is shown in Fig. 3.3, where for bench-marking,

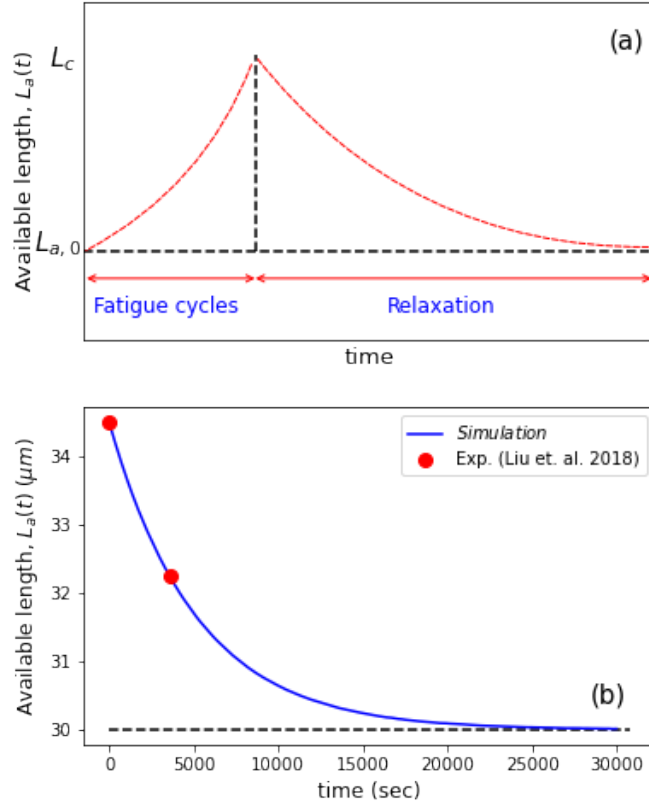


Figure 3.4: (a) Schematic of evolution of available length during a series of cycles followed by relaxation at zero force. (b) Relaxation dynamics of fibril of length  $L_c$  (with no sacrificial bonds). At long time fibril equilibrates to initial experimental length  $L_{a,0}$ . Relaxation curve averaged over 1000 runs.

we have compared the data with the results of Ref. [9], where crosslinks break beyond a threshold strain. For convenience of use in the kinetic model, we fit a ninth order polynomial

$$\sigma(\lambda) = \sum_{n=1}^9 a_n (\lambda - 1)^n, \quad (3.4)$$

to the data.

### 3.1.3 Determination of parameters and rates

We now describe how to determine model parameters:  $L_c$ ,  $P(\ell)$ ,  $\alpha_0$  and  $\beta_0$ . At zero force, sacrificial bonds form and break spontaneously with rates  $\beta_0 L_a/b$  and  $\alpha_0 N_b$  respectively, where  $N_b$  is the number of sacrificial bonds present at any instant. At steady state, rate of fragmentation and formation of bonds should be equal, implying

$$\alpha_0 \langle N_b \rangle = \frac{\beta_0 \langle L_{a,0} \rangle}{b}, \quad F = 0, \quad (3.5)$$

where the zero in the subscript of  $L_{a,0}$  denotes the reference time after steady state is reached, taken to be  $t = 0$ . Also,  $\langle L_{a,0} \rangle = L_c - \langle N_b \rangle \langle \ell \rangle$  where  $\langle \ell \rangle$  and  $\langle N_b \rangle$  are the average loop size and the average number of loops respectively. Substituting for  $\langle L_{a,0} \rangle$  in Eq. (3.5), we obtain

$$\langle N_b \rangle = \frac{L_c \beta_0}{\alpha_0 b + \beta_0 \langle \ell \rangle}, \quad (3.6)$$

$$\frac{L_c}{L_{a,0}} = 1 + \frac{\beta_0 \langle \ell \rangle}{\alpha_0 b}. \quad (3.7)$$

We estimate  $L_c/\langle L_{a,0} \rangle$  from the experimental data [7]. To do so, we assume that after 20 cycles, most of the sacrificial bonds are broken and hidden lengths appear as residual strain. Equating the ratio  $L_c/\langle L_{a,0} \rangle$  to the experimental residual extension of  $\approx 1.15$  after 20 cycles, as shown in Fig. 5(c) of Ref. [7], we obtain  $L_c/\langle L_{a,0} \rangle = 1.15$ . The initial length of the fibril is known to be  $\langle L_{a,0} \rangle = 30 \mu m$ , thus fixing  $L_c$ . The inter-monomer distance  $b$  is chosen to be  $b = 1.4 \text{ nm}$ , equal to the inter-bead distance in the MD model [9]. To choose the distribution of the hidden loop sizes, we proceed as follows. In kinetic models for collagen, the loop sizes were chosen proportional to the contour length of the polymer [10, 76]. However, in fibrils, we expect the hidden length released from breakage of sacrificial bonds (representing a cumulative effect of cross-links at MD length scale [8, 9] and the U-shaped telopeptides at the atomistic scale [6]) to be order of a few

monomer lengths, as the equilibrium distance of cross-links ( $\approx 10 \text{ \AA}$ ) is less than the equilibrium distance of the LJ potential ( $\approx 16.5 \text{ \AA}$ ). We assume the hidden loops to be on an average four monomer lengths.

We make the choice of  $P(\ell)$  to be a uniform distribution  $U[2b, 6b]$ . We will argue that this choice is consistent with the MD-model for fibrils, as well as show that the results are not sensitive to the choice as long as the perturbations to  $P(\ell)$  are not significant. With this choice of  $P(\ell)$ , we obtain  $\langle \ell \rangle = 4b$ .

On substituting these values of  $L_c/\langle L_{a,0} \rangle$ ,  $b$  and  $\langle \ell \rangle$  in Eq. (3.7), we obtain  $\beta_0/\alpha_0 = 0.0375$ . Then from Eq. (3.6), we obtain  $\langle N_b \rangle / (L_c/b) \approx 0.0326$ . We now argue that this number that follows from the experimental residual strain has the correct order of magnitude. The kinetic model represents a fibril with diameter of a single microfibril, such that 215 monomers in the kinetic model represents  $215 \times 5$  monomers of the microfibril. A molecule in the microfibril has two crosslinks. This corresponds to 10 sacrificial bonds per 215 monomers in the kinetic model or equivalently we expect  $\langle N_b \rangle / (L_c/b) \approx 0.047$ . Among these, some will be broken at zero force, and the calculated result  $\langle N_b \rangle / (L_c/b) \approx 0.0326$  makes sense.

Knowing the ratio  $\beta_0/\alpha_0 = 0.0375$ , we would like to now fix the values of  $\alpha_0$  and  $\beta_0$ . For this, we use the fact that as part of the cyclic loading experiment [7], recovery of residual strain is also studied. In the experiment, the fibril is cyclically loaded for 10 cycles followed by relaxation at zero force for 60 minutes, as shown schematically in Fig. 3.4(a). We will choose an  $\alpha_0$  for which the relaxation time matches with the experimental data. For doing so, we take a polymer of length  $L_c$  with no sacrificial bonds which roughly mimics the state after 10 cycles. We then equilibrate the system at zero force. After equilibration, the available length is  $L_{a_0}$ , as shown in Fig 3.4(b). The relaxation dynamics from our model matches well with the experiment (experimental data shown as solid circles) for  $\alpha_0 = 1.69 \times 10^{-4} s$ , as shown in Fig 3.4(b).

Finally, we describe how we fix the parameters  $\Delta x_f$  and  $\Delta x_b$ , as defined in Eqs. (3.2) and

Table 3.1: The parameters for the kinetic model for collagen fibril.

Parameter	Description	Value
$L_{a,0}$	available length at zero force	$30 \mu m$
$L_c$	contour length	$1.15 L_{a,0}$
$b$	bond length	$1.4 nm$
$P(\ell)$	loop size distribution	$U[2b, 6b]$
$\langle \ell \rangle$	mean loop size	$4b$
$\beta_0$	formation rate of sacrificial bonds at zero force	$6.32 \times 10^{-6} s^{-1}$
$\alpha_0$	fragmentation rate of sacrificial bonds at zero force	$1.69 \times 10^{-4} s^{-1}$
$\Delta x_f$	distance to transition state	$.01 nm$
$\Delta x_b$	distance to transition state	$0$
$v$	pulling velocity	$125 nm/s$
$T$	temperature	$298 K$

(3.3). The force  $F$  in these equations is the force felt by the sacrificial bonds. Since the sacrificial bonds or crosslinks are between different collagen chains and transverse to the direction of loading, we have no direct way of measuring  $F$ . Instead, we approximate it by the force in a chain. In the MD simulations, the force in a chain is  $\sigma A_0/185$ , where  $A_0$  is the cross-sectional area of the fibril, and 185 is the number of chains. We then treat  $\Delta x_f$  as a parameter. Note that  $\Delta x_f$  controls when the stretch ratio at which fragmentation of sacrificial bonds is enhanced. We perform a parametric study of the dependence of the stress-stretch response for uniaxial loading on  $\Delta x_f$ . We choose that value of  $\Delta x_f$  for which the strain at which deviation from the initial linear behavior coincides with that in the experiment. Using this procedure, we converge on  $\Delta x_f$  to be .01 nm. We notice that the formation rate is low and during the pulling experiment, there are very few reformations of sacrificial bonds. We therefore choose  $\Delta x_b$  to be zero, and check that even if a non-zero value is chosen, the results do not change.

The values of the different parameters are summarized in Table 3.1.

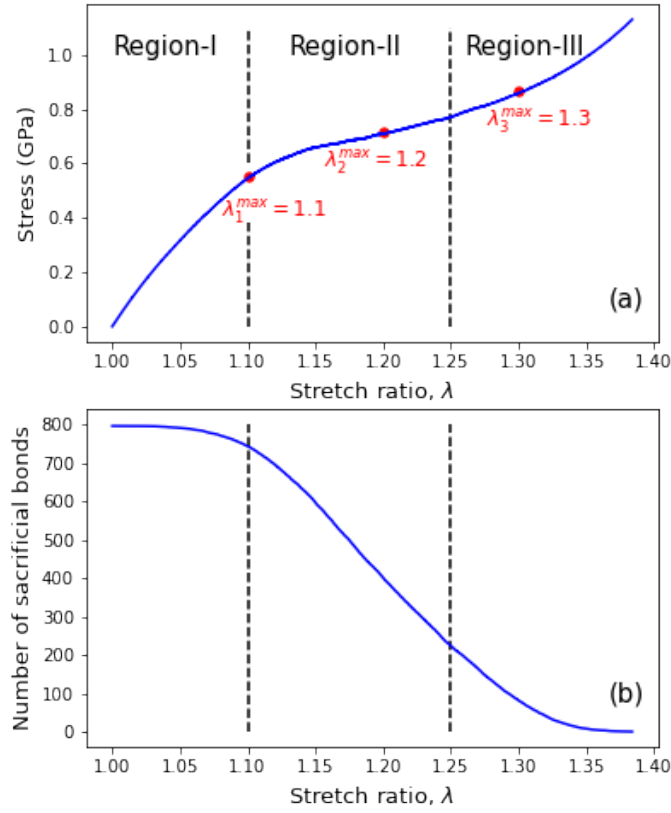


Figure 3.5: (a) The mean stress-strain response of the polymer under monotonic loading obtained using kinetic model. It shows three distinct regions which are roughly demarcated by the vertical dotted lines.  $\lambda_1^{max}$ ,  $\lambda_2^{max}$  and  $\lambda_3^{max}$  correspond to the maximum strain applied in the three different cyclic loading protocols. (b) The mean number of sacrificial bonds for a given strain for monotonic loading.

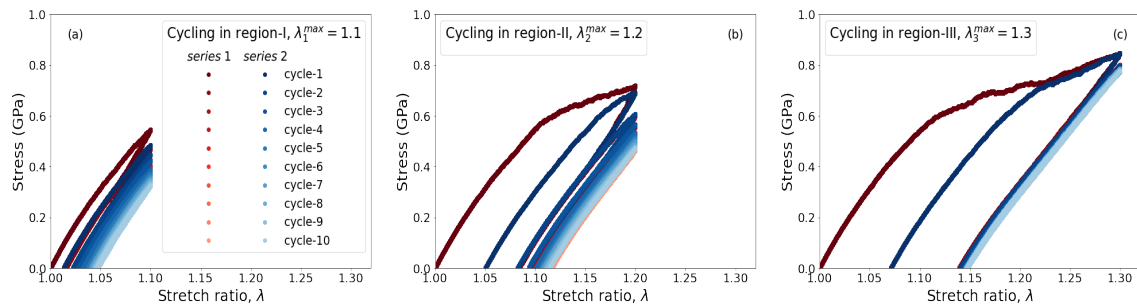


Figure 3.6: The macroscopic stress-stretch response for cyclic loading for (a)  $\lambda^{max} = 1.1$  (region-I), (b)  $\lambda^{max} = 1.2$  (region-II), and (c)  $\lambda^{max} = 1.3$  (region-III). In all the three cases, the response shows moving hysteresis loops which saturate with loading cycles for both series 1 (first 10 cycles) and series 2 (next 10 cycles after 60 minutes relaxation at  $F = 0$ ) loading.

### 3.1.4 Simulation Protocol

The system evolves in time through constant time steps  $dt$ . In this time interval, the probabilities of fragmentation ( $p_f$ ) and formation ( $p_b$ ) of sacrificial bonds are given by  $p_f = k_f N_b(t) dt$  and  $p_b = k_b N_f(t) dt$  where,  $N_f(t) = L_a(t)/b$  is the number of free sites and  $N_b(t)$  is the number of sacrificial bonds. The time step  $dt$  is chosen such that the probabilities are much smaller than 1 at all times. Whenever a sacrificial bond forms, a hidden loop of length  $\ell$  is assigned from distribution  $P(\ell)$ . When a sacrificial bond breaks, a hidden length of a randomly chosen loop is released. The available length gets updated as  $L_a \pm \ell$  depending on breaking/formation event of sacrificial bonds. The rates are also updated depending on the current force and current  $L_a$ .

We start with a polymer of length  $L_c$  with zero sacrificial bonds and equilibrate the system at zero force. After equilibration, to do cyclic loading, we pull at a constant velocity such that  $v = dx/dt$ , where  $x = \lambda L_a(t)$  is the end to end distance. The time-dependent stress  $\sigma(x, L_a(t))$  is calculated using Eq. (3.4) and the corresponding rates are determined. The polymer is pulled up to a pre-decided stretch ratio  $\lambda^{max}$  after which the pulling velocity is reversed to  $-v$ , and the polymer is stretched back to zero force. This completes one loading cycle.

## 3.2 Results

### 3.2.1 Uniaxial loading

To establish the effectiveness of the proposed kinetic model, we first simulate response of the fibril chain polymer to monotonically increasing load. The average macroscopic response obtained from 16 realizations is shown in Fig. 3.5(a). For each run, the system is first equilibrated at zero force, after which displacement (end to end distance) is

increased at a constant velocity of  $125 \text{ nm/s}$ . The macroscopic response exhibits three distinct regions: an initial region (region-I) where stress increases linearly with strain, an intermediate region where stress is weakly increasing with strain (region-II) and a final region where the stress increases non-linearly with strain (region-III). These qualitative features, of three distinct regions, of the macroscopic response are consistent with what has been observed in pulling experiments of collagen fibril [7, 50].

The existence of three distinct regimes is better understood in terms of the number of the intact sacrificial bonds at any given strain. In Fig. 3.5(b), we show the mean number of sacrificial bonds for a given applied strain. For small strains, corresponding to region-I there is only a marginal decrease from its initial equilibrium value. Further increase in strain, corresponding to region-II, results in a sharp decrease in the number of sacrificial bonds, thereby releasing hidden lengths and causing relaxation in the stresses. Finally all sacrificial bonds are broken in region-III. The change in slope of the stress-strain curve in region-II occurs due to breaking of sacrificial bonds.

### 3.2.2 Cyclic loading

We next simulate the cyclic loading patterns reported in Ref. [7] to compare the characteristic features of the mechanical response seen in the experiment with our simulations. Cyclic load is applied such that in each cycle the chain is stretched upto a maximum stretch ratio,  $\lambda^{max}$ . As in Ref. [7], we also consider  $\lambda^{max}$  to lie in the three distinct regimes by choosing it to be  $\lambda^{max} = 1.1, 1.2, 1.3$  (the corresponding positions on the macroscopic response is shown by red circles in Fig. 3.5(a)) and these stretch ratios are representative points of regions I, II and III. The fibril is subjected to cyclic loading using the protocol described in Sec. 3.1.4 with pulling speed  $v = 125 \text{ nm/s}$ , chosen to be same as in experiment [7]. The polymer is subjected to 10 loading cycles (series 1) and then relaxed at zero force for 60 minutes, and then subjected to 10 more loading cycles (series 2).

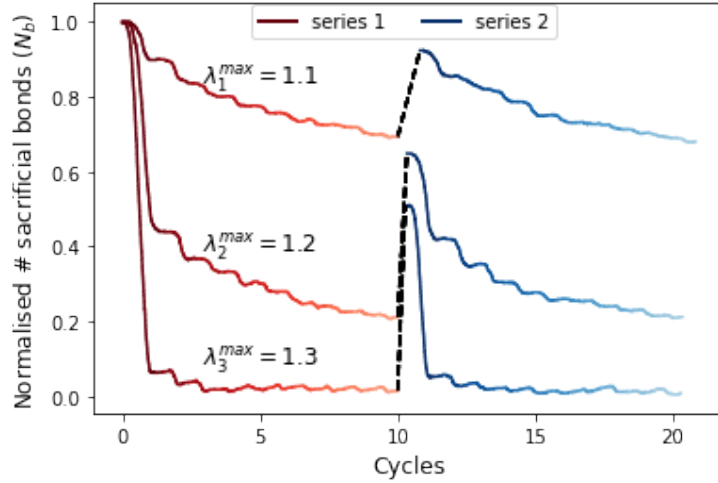


Figure 3.7: The variation of number of sacrificial bonds with loading cycles for both series 1 and series 2 and for different stretch ratios,  $\lambda^{max}$ . The dashed line corresponds to discontinuity due to relaxation before series 2 loading. After relaxation, there is a partial recovery in number of sacrificial bonds for all  $\lambda^{max}$ . Color scheme used for cycles is same as in Fig. 3.6

We first present results for the variation of the stress-stretch curve with cycles. The stress-stretch ratio curves show hysteresis, as evident in Fig. 3.6. The first cycle exhibits hysteresis as well as residual strain at a completely unloaded state. Further cycling results in the subsequent hysteresis loops to shift to the right implying accumulation of residual strains. The hysteresis loops eventually tend to reach a steady state with number of cycles for both the series and for all three representative values of  $\lambda^{max}$ . These features from the simulations of the kinetic model are consistent with the observed trends in the experiment [7].

In the associated number of intact sacrificial bonds, shown in Fig. 3.7 with fading shades of red and blue for series 1 and 2 respectively, the progressive breakage patterns with increasing cycles is clearly evident. For  $\lambda^{max} = 1.1$ , the first cycle results in breakage of 10% bonds and in subsequent 9 cycles there is a further gradual reduction in sacrificial bonds, slowly reaching a steady state. During the waiting interval, bonds reform (shown with dashed line). The cyclic loading of series 2 causes the number of sacrificial bonds to gradually decrease again. For  $\lambda_2^{max}$ , however, most of the breakage occurs in the first cycle as the number of shows a dramatic decrease (by more than 50%). Subsequent cycles

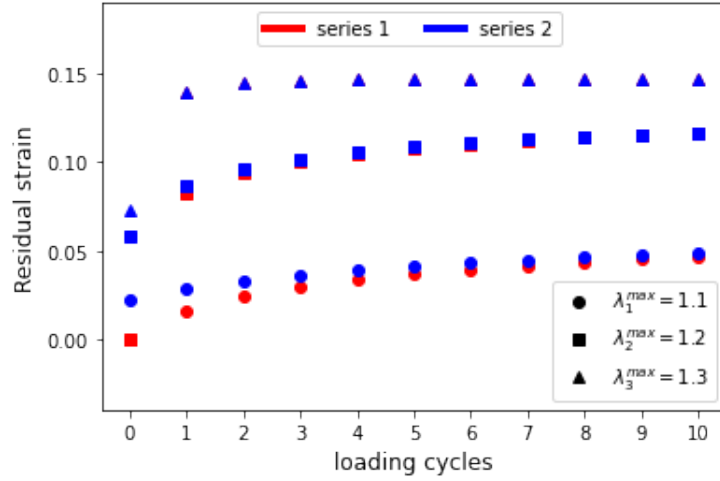


Figure 3.8: The evolution of residual strain with number of loading cycles for both series 1 and series 2 for different stretch ratios,  $\lambda^{max}$ . The magnitude and final saturated value of residual strain depends on the maximum stretch ratio,  $\lambda^{max}$ .

show comparatively lower rate of breakage per cycle. Interestingly, for a similar waiting interval, the reformation of bonds is significantly higher than for  $\lambda_1^{max}$  and this could be attributed to the comparatively larger available length from more number of broken bonds. For the cyclic loads with  $\lambda_3^{max}$ , first cycle results in breakage of more than 90% of the sacrificial bonds. Since most bonds are already broken further cycling does not affect the overall status of intact bonds appreciably. Waiting period recovers 50% of the initial bonds which again break primarily in the first cycle of the series 2.

The residual strain accumulates with increasing cycles and reaches a steady state for both series 1 and series 2 loading for all three  $\lambda^{max}$  (see Fig. 3.8). During the relaxation period between the two series, the residual strain reduces by approximately 50%. The magnitude of the residual strain when steady state is reached depends on  $\lambda^{max}$  (see Fig. 3.8). It can be seen that the steady state residual strains follows the order of  $\lambda_3^{max} > \lambda_2^{max} > \lambda_1^{max}$ , in agreement with the experiments [7]. The residual strain increasing with  $\lambda^{max}$  is due to the larger number of sacrificial bonds breaking in the first cycle itself for higher  $\lambda^{max}$ , as shown in Fig. 3.7. It can also be seen that number of sacrificial bonds reform during relaxation which accounts for recovery in residual strain.

The energy dissipated per cycle (area under the loading-unloading curve) decreases with

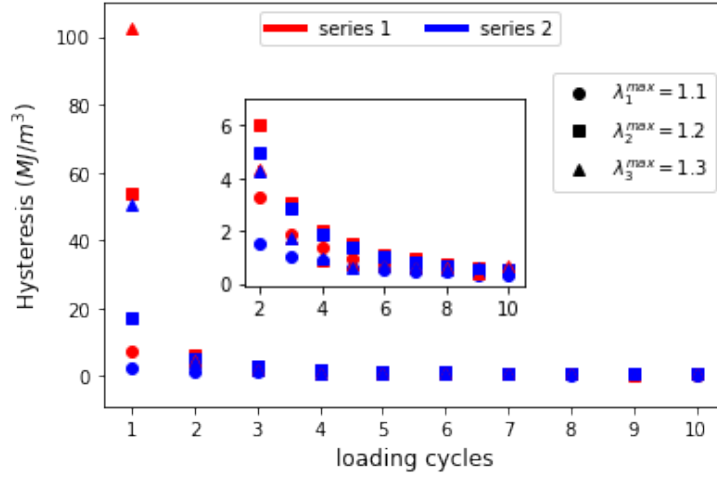


Figure 3.9: The evolution of energy dissipation with number of loading cycles for both series 1 and series 2 and for different stretch ratios,  $\lambda^{max}$ . The data from 2nd cycle onward is zoomed and shown in the inset figure.

increase in the number of cycles and reaches steady state for both series 1 and series 2 loading (see Fig. 3.9) for all chosen stretch ratios. There is a partial recovery in energy dissipation after relaxation as seen from first cycle of series 2 loading (see Figs. 3.6 and 3.9). The area of the hysteresis loop after the first cycle also follows the pattern  $\lambda_3^{max} > \lambda_2^{max} > \lambda_1^{max}$ . This is because the first cycle of region-III has maximum number of sacrificial bond breaking compared to the other two regions, as evident from Fig. 3.7. Restoration of sacrificial bonds on relaxation accounts for recovery in energy dissipation.

We now quantify the approach of residual strain and energy dissipation to their respective steady state values. We find that the deviation of residual strain and energy dissipation from their steady state value has an exponential decrease to zero with number of loading cycles (see Fig. 3.10, where the data for  $\lambda^{max} = 1.1$  and  $\lambda^{max} = 1.2$  are shown). We extract the experimental data for these quantities from Ref. [7] and find that the exponential decrease is also seen in experiment (see Fig. 3.10). This allow us to determine a characteristic cycle number  $c^*$  defined as:

$$\epsilon_r(c) - \epsilon_r(\infty) \propto e^{-c/c^*}, \quad (3.8)$$

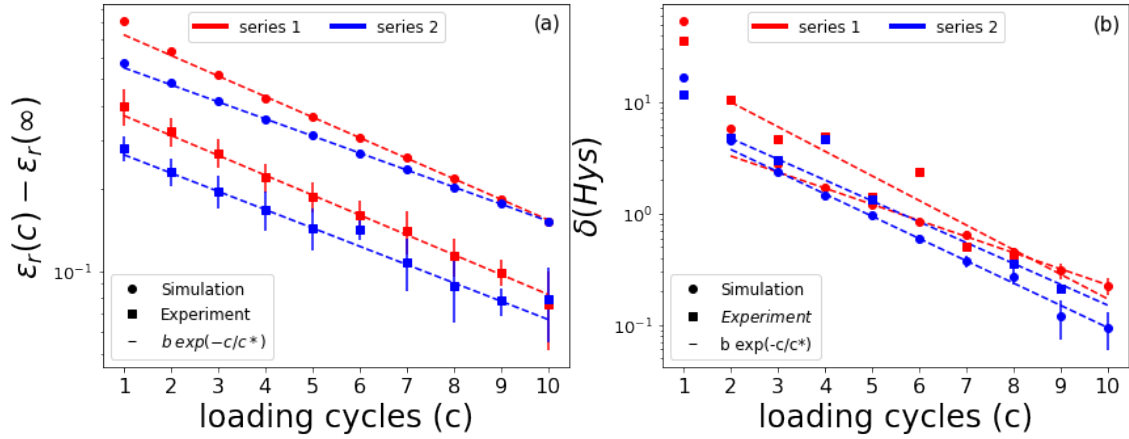


Figure 3.10: The variation of the deviation of (a) residual strain and (b) area of hysteresis loop from their respective steady state values with number of loading cycles. The corresponding experimental data from Liu et. al. (2018) [7] are shown with squares. Both quantities approaches steady state exponentially. The best fits are shown by dashed lines.

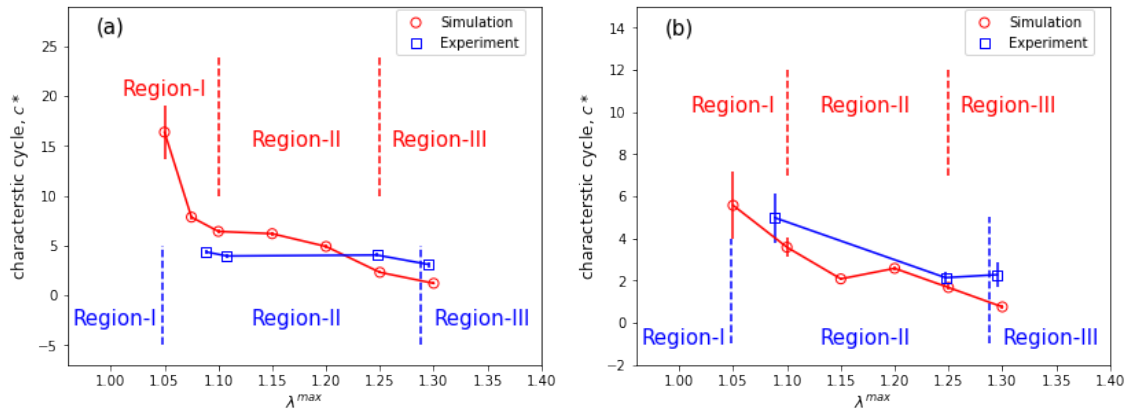


Figure 3.11: The variation of characteristic cycle  $c^*$  with the maximum stretch ratio,  $\lambda^{max}$  obtained for (a) residual strain and (b) energy dissipation.

where  $\epsilon_r(c)$  is residual strain at cycle  $c$ ,  $\epsilon_r(\infty)$  is the steady state value of residual strain.

We compare the characteristic number of cycles,  $c^*$ , obtained for residual strain from simulations and experiments of Liu et al. [7] in Fig. 3.11(a). We use the average  $c^*$  of series 1 and 2 for the both simulations and experimental data. Since  $c^*$  is not quoted in the experiments, we fit the extracted experimental data to obtain  $c^*$ . From simulations, for small  $\lambda^{max}$ , in regime I, we find the polymeric chain takes larger number of cycles ( $\approx 16$ ) to reach steady state. This large value of  $c^*$  for small stretch ratio is understood as ideally, polymer should take infinite cycles to reach steady state within elastic regime.

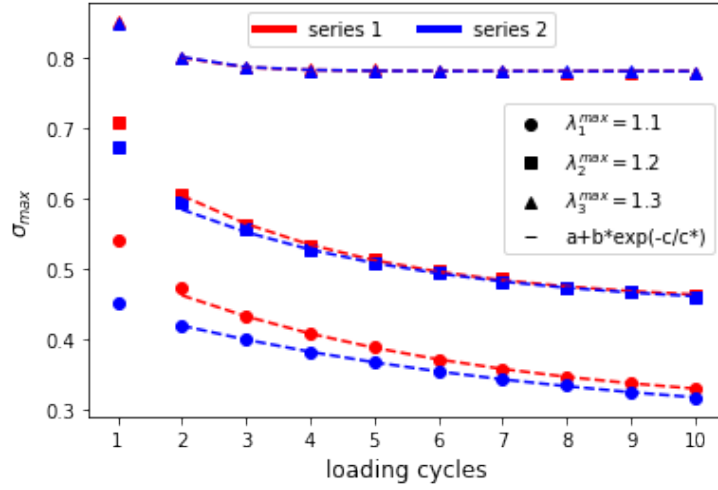


Figure 3.12: The variation of peak stress with number of loading cycles for different  $\lambda_1^{max}$ , before (series 1) and after relaxation (series 2). Peak values of stress depends on  $\lambda^{max}$  and show a partial recovery on relaxation (series 2).

With increasing  $\lambda^{max}$ ,  $c^*$  decreases. In region II, the steady state is reached at significantly lower cycles ( $\approx 5$ ) and there is marginal decrease with increasing  $\lambda^{max}$ . Further increase in  $\lambda^{max}$ , corresponding to region III, shows again a further drop in  $c^*$  implying faster approach to steady state in stress-lambda response. Experimental data compares very well in the region II as it also exhibits marginal change with increasing  $\lambda^{max}$ , and in region III there is decrease in  $c^*$  with increasing  $\lambda^{max}$ .

We also compare the value of characteristic cycle  $c^*$ , obtained for energy dissipation from simulations and the extracted experimental data as shown in Fig. 3.11(b). We obtain a similar trend of  $c^*$  with  $\lambda^{max}$  for energy dissipation also. The value of  $c^*$  is large in region-I, then it decreases with  $\lambda^{max}$ , it shows some plateau in region-II and then further decreases sharply in region-III. Again, we see a good match with experimental results.

Finally, we study two more quantities studied in the experiment: peak stress and elastic modulus. The peak stress (stress at  $\lambda^{max}$ ) decreases with number of cycles for both series 1 and 2 and for all three stretch ratios (see Fig. 3.12). It also approaches the steady state exponentially. The peak stress in the first cycle in a particular region depends on choice of  $\lambda^{max}$  and follows the order:  $\sigma(\lambda_3^{max}) > \sigma(\lambda_2^{max}) > \sigma(\lambda_1^{max})$ .

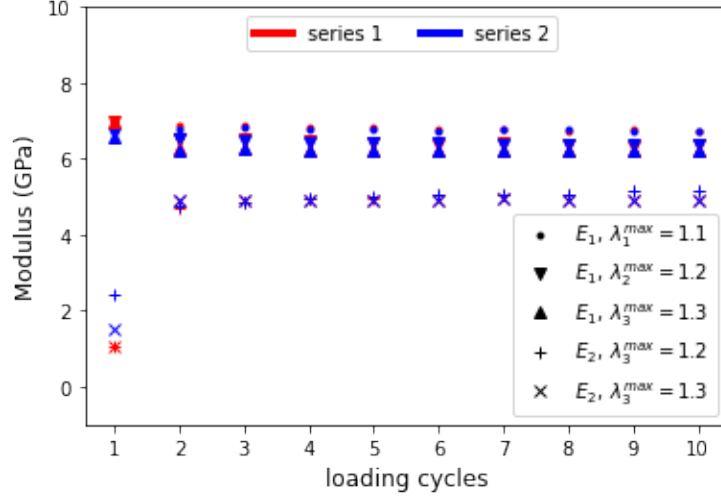


Figure 3.13: Elastic modulus  $E_1$  remains invariant to cyclic loading for both series and in all three regions while  $E_2$  (for region-II and III) becomes constant after first cycle and then remains invariant to cyclic loading.

We define two elastic moduli  $E_1$  and  $E_2$  in accordance with the experimental study [7]. The elastic modulus  $E_1$  is calculated from the slope of the stress-stretch (Fig. 3.6) curve up to  $\lambda \approx 1.02$  while  $E_2$  is calculated from the slope (where  $d\sigma/d\lambda \approx \text{constant}$ ) of the stress-stretch curve in region-II. We find that  $E_1$  is not affected by cyclic loading for all three stretch ratios while  $E_2$  becomes a constant after the first loading cycle and then remains invariant to cyclic loading for  $\lambda_2^{max}$  and  $\lambda_3^{max}$  in both series loading (see Fig. 3.13). However, the extent of transition region between region-I to region-II decreases with cycles within  $\lambda^{max} = 1.2, 1.3$  (see Fig. 3.6(b) and (c)) and these features are also observed in the experiment. Our results are in good agreement with the cyclic loading experiment (see Figs. 3, 4, 5 in Ref. [7]).

### 3.3 Conclusions and Discussion

Experimentally, the stress-stretch response of a single collagen fibril subject to cyclic loading [7, 55] within a fixed stretch ratio  $\lambda$  is known to show moving hysteresis loops and residual strains that increase and saturate with number of cycles. The fibril is known to show recovery in energy dissipation as well as residual strains on relaxation. These

features were thought to be related to the presence of sacrificial bonds within the fibril [7]. To test this hypothesis, we develop a stochastic kinetic model specifically for collagen fibril. The model treats the collagen fibril to be a polymeric chain that has hidden lengths secured by sacrificial bonds. The two primary ingredients of the model are: a reference stress-stretch relation for the available length of the polymer and stochastic formation and fragmentation of sacrificial bonds. The reference stress-stretch relation is first established from molecular dynamics simulations of an existing coarse-grain fibril model [9]. The kinetic model incorporates formation and breakage of sacrificial bonds and release of hidden lengths based on Bell's theory. We estimated the model parameters by comparing with available experimental data and used kinetic Monte Carlo methods to simulate the cyclic loading experiment.

The model qualitatively reproduces the main features of the experiment such as time evolution of hysteresis loops, energy dissipation, peak stress and residual strain etc. It is shown that these quantities approach their respective steady states exponentially with the number of loading cycles. We find that the characteristic cycle number associated with this exponential decay is in close agreement with the characteristic cycle number extracted from the reported experimental data. The breaking of sacrificial bonds is responsible for hysteresis (energy dissipation) and the corresponding release of hidden lengths appears as residual strain. The magnitude of hysteresis, peak stress and residual strain after first cycle is proportional to maximum stretch ratio  $\lambda^{max}$ . The recovery of the fibril is proportional to the relaxation time and spontaneous formation and breaking of sacrificial bonds at zero force is a possible healing mechanism in the collagen fibril.

The presence of a characteristic cycle number has significance in the description of the time dependent cyclic response of collagen. In particular, it has the potential of being utilised for comparison of fibril response across animals, ages, stages of disease, level of hierarchy, response to medication, etc. This is a promising area for future experimental investigation.

While generalizing the kinetic model to other biological polymeric materials or collagen types, careful consideration should be given to its core assumptions and mechanisms, like whether these systems share similar features, such as sacrificial bonds and hidden lengths. A validation of the system through simulation data or experiments will be crucial to knowing the nature of hidden lengths and loops and determining whether they arise from physical attributes or emerge from entanglements and de-entanglements. The force law, which is an important ingredient in the kinetic model, is also material-specific. A knowledge of phenomenology is required while generalizing the kinetic model to other systems, and existing MD simulations can give an idea of inputs to the model.

The kinetic model is able to reproduce the majority of the characteristic features of the fatigue experimental data in Ref. [7], thus providing an insight into the essential mechanisms at work. It is a minimal model that does not explicitly take into account the geometrical features of the model, including complex hierarchical structure and biochemical environments. The strength of sacrificial bonds is known to depend on the type of ionic environment [5]. The kinetic model is based on a macroscopic force law determined from a microscopic model restricting bond breaking. In a real-life scenario, during loading, a complex stress field could result at the fibril level depending on load path selection and load partitioning in the fibril because of its hierarchical structures. However, as the kinetic model captures key features of the experiment, these details may not be relevant or may be averaged out at this scale.

One feature that kinetic model is not able to explain is the experimental observation that the strength of a fibril, that has undergone cyclic loading, is increased. This suggests that while the model effectively captures key features of the mechanical response, it may not fully account for all the mechanisms at play. This increased strength could be due to permanent rearrangement of molecules inside the fibril, making the feature history-dependent. It is to be noted that reformation of sacrificial bonds, as in the present kinetic model, can only lead to recovery of strength up to the virgin sample, which is independent

of past history. It is possible that the observed gain in strength may be accounted for by a three-dimensional model of a fibril incorporating detailed microscopic interactions. It would thus be of interest to develop a coarse grained model for the fibril that incorporates sacrificial bonds. In addition, it will provide a microscopic basis for the validity of the kinetic model, as well as allow for a determination of parameters. A microscopic model would also have a characteristic relaxation time, which is assumed to be zero in the present kinetic model, which will have an additional contribution to the hysteretic response.

Interestingly, at tissue scale also, the stress-strain response exhibits moving hysteresis loops, residual strain, etc [85]. Linka et. al. [102], proposed a constitutive damage model that reproduces the experimental results of the tendon overloading experiment [85]. The kinetic model described in this chapter, with suitable modifications, would also be ideally suited to explain the results at tissue level.

## Appendix A: Coarse grained collagen fibril model

In this appendix, we describe the coarse-grained model for the fibril that we have used for MD simulations. The model is from Ref. [8, 9].

A collagen molecule is represented by 215 beads connected with spring to each other. The distance between two consecutive bead is  $b = 1.4 \text{ nm}$ , which is roughly equals to the diameter of collagen molecule. Five collagen molecules are arranged in staggered manner in z-direction while in pentagonal geometry in x-y plane to form a microfibril, as shown in Fig 3.2. This staggered arrangement of collagen molecules give rise to the characteristic D-period of collagen fibril ( $67\text{nm}$ ). The diameter of a single microfibril is  $\approx 3.5 \text{ nm}$ . Terminal beads of each tropocollagen molecule forms a divalent or trivalent cross-link within a microfibril. In divalent cross-link, end beads of a molecule forms a single connection with a nearest bead from it's neighbouring molecule while in case of trivalent cross-link, the end beads forms two connection with the closest beads from it's nearest and next-nearest collagen molecule. These terminal connections represents the enzymatic cross-links in fibril. We have considered the case with hundred percent cross-link ( $\beta = 100\%$ ), which means all the terminal ends will form a cross-links with their neighbouring molecule. The ratio of trivalent (33%) and divalent (66%) cross-links has been kept fixed. Now, 37 of these microfibrils are arranged in a hexagonal close packing to represent a collagen fibril. The length and diameter of fibril model are  $343.6 \text{ nm}$  and  $25.9 \text{ nm}$  respectively. The periodic boundary conditions has been used to mimic the fibril of infinite length. Periodic boundary condition ensures the D-periodicity of the fibril structure.

The non bonded interaction between beads of fibril is given by Lenard-Jones potential as :

$$U_{LJ} = 4\epsilon \left[ \left( \frac{\sigma}{r} \right)^{12} - \left( \frac{\sigma}{r} \right)^6 \right], \quad (3.9)$$

where  $r$  is the distance between interacting beads and  $\sigma$  is the distance parameter and  $\epsilon$  is

Table 3.2: The parameters for the MD-model of fibril.

Model parameters	Value
$\epsilon$ - LJ energy parameter ( $kcal\ mol^{-1}$ )	6.87
$\sigma$ - LJ distance parameter ( $\text{\AA}$ )	14.72
$\theta_0$ - Equilibrium bending angle ( <i>degree</i> )	180
$k_\theta$ - Bending strength constant ( $kcal\ mol^{-1}\ rad^{-2}$ )	14.98
$r_0$ - Equilibrium distance (tropocollagen) [ $\text{\AA}$ ]	14.00
$r_1$ - critical hyperelastic distance (tropocollagen) [ $\text{\AA}$ ]	18.20
$r_{break}$ - bond breaking distance (tropocollagen)	21.00
$k_{T0}$ - Stretching strength constant (tropocollagen) [ $kcal\ mol^{-1}\ \text{\AA}^{-2}$ ]	17.13
$k_{T1}$ - Stretching strength constant (tropocollagen) [ $kcal\ mol^{-1}\ \text{\AA}^{-2}$ ]	97.66
$r_0$ - Equilibrium distance (divalent crosslink) [ $\text{\AA}$ ]	10.00
$r_1$ - critical hyperelastic distance (divalent crosslink) [ $\text{\AA}$ ]	12.00
$r_{break}$ - bond breaking distance (divalent crosslink)	14.68
$k_{T0}$ - Stretching strength constant (divalent crosslink) [ $kcal\ mol^{-1}\ \text{\AA}^{-2}$ ]	0.20
$k_{T1}$ - Stretching strength constant (divalent crosslink) [ $kcal\ mol^{-1}\ \text{\AA}^{-2}$ ]	41.84
$r_0$ - Equilibrium distance (trivalent crosslink) [ $\text{\AA}$ ]	8.60
$r_1$ - critical hyperelastic distance (trivalent crosslink) [ $\text{\AA}$ ]	12.20
$r_{break}$ - Bond breaking distance (trivalent crosslink)	14.89
$k_{T0}$ - Stretching strength constant (trivalent crosslink) [ $kcal\ mol^{-1}\ \text{\AA}^{-2}$ ]	0.20
$k_{T1}$ - Stretching strength constant (trivalent crosslink) [ $kcal\ mol^{-1}\ \text{\AA}^{-2}$ ]	54.60
$m$ - mass of tropocollagen bead [ <i>a.m.u</i> ]	1358.7

energy parameter (depth of potential).

The bending energy ( $U_\theta$ ) between three consecutive beads of collagen molecule is given by harmonic interaction as :

$$U_\theta = k_\theta(\theta - \theta_0)^2 \quad (3.10)$$

where  $k_\theta$  is bending strength and  $\theta_0$  is equilibrium angle.

The interaction between bonded beads is defined by a bi-harmonic potential as:

$$F_{bond} = -\frac{\partial U_{bond}}{\partial r} = \begin{cases} k_{T0}(r - r_0) & \text{for } r < r_1, \\ k_{T1}(r - r_0) & \text{for } r_1 \leq r < r_{break}, \\ 0 & \text{for } r > r_{break}. \end{cases} \quad (3.11)$$

where  $r_0$  is the equilibrium distance between two beads,  $k_{T0}$  and  $k_{T1}$  are spring constants between distances 0 to  $r_1$  and 0 to  $r_{break}$ .

The simulations were performed using LAMMPS [103]. Time step was set to  $\Delta t = 10 \text{ fs}$ , and the equations of motion were integrated with langevin thermostat with drag coefficient  $1000 \text{ fs}$  and temperature  $310 \text{ K}$ . The fibril was equilibrated for  $20 \text{ ns}$  and then a constant strain rate of  $10^7 \text{ s}^{-1}$  was applied. All the parameters used in simulation are given in Table 3.2. These parameters have been developed for collagen molecules in Refs. [65,78] and specifically for the fibril model in Refs. [8,9].

# Chapter 4

## **Dissipation and recovery in collagen fibril under cyclic loading: a molecular dynamics study**

The content of this chapter is from Ref. [104].

This chapter aims to explain the key experimental features observed during cyclic loading experiments, as described in Sec 1.5 using a microscopic approach.

Different approaches have been used to model the macroscopic response of fibrils under cyclic loading. In last chapter, we proposed a kinetic model for collagen fibrils that takes into account the presence of hidden loops, stochastic fragmentation, and the stochastic reformation of sacrificial bonds [97]. This kinetic model was a generalisation of the kinetic model for collagen molecules that incorporated sacrificial bonds and hidden lengths [10, 76]. The kinetic model for fibril successfully replicated the key features observed in experimental data [7], including the movement of hysteresis loops, the time evolution of residual strains and energy dissipation, and the recovery observed during relaxation. We demonstrated that the approach towards reaching a steady state is influenced

by a characteristic cycle number for both residual strain and energy dissipation, and our findings were consistent with the experimental data of Ref. [7]. Within a continuum mechanics approach, a constitutive model was proposed that accounts for both viscoelastic and plastic deformations [11]. The model parameters were fitted using experimental data, and the experimental phenomena was well-reproduced by the model. The model predicts plastic deformation, and improved performance after relaxation.

Both modeling approaches discussed above are at the macroscopic level. The kinetic model is a minimal representation that does not incorporate the geometric properties of the collagen fibril. While it captures the dominant energy dissipation mechanism due to breaking of cross-links (sacrificial bonds), it fails to capture plastic deformation as well as non-zero steady state hysteresis loops observed in experiments. The continuum models [11] are based on phenomenological laws that have a substantial number of parameters that have to be fitted to the experimental data. While it is a powerful tool for large scale analysis, it is not possible to gain an insight into the molecular basis of the dissipation and recovery mechanisms. Here, we approach the problem of cyclic loading from the microscopic point of view using molecular dynamics (MD) simulations.

In this chapter, we build upon existing MD models [8,9] to account for the experimental features observed during cyclic loading. We show that existing models of fibrils, when subjected to cyclic loading, are able to reproduce the time evolution of hysteresis loops and the accumulation of residual strains, as observed [7] in macroscopic responses of collagen fibrils subjected to cyclic loading. However, these models cannot account for the recovery of the collagen fibril on relaxation. We incorporate dynamic cross-link reformation into the MD model during relaxation and demonstrate that this feature allows us to reproduce experimental findings such as recovery upon relaxation. Further, this reformation of cross-links increases the strength compared to the strength of the fibril post cyclic loading. We also show that the characteristic cycle number, describing the approach towards steady state, has a value similar to that in experiments. Compared to earlier kinetic

models, the MD model is able to obtain non-zero steady state hysteresis loops and account for plastic deformation, as observed in experiments.

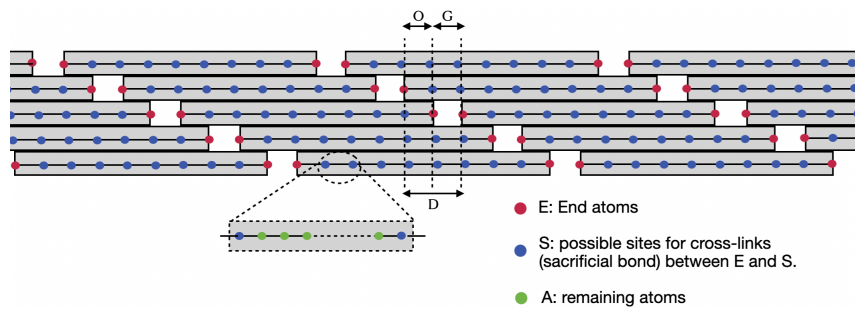
## 4.1 Model

### 4.1.1 Geometry of the collagen fibril model

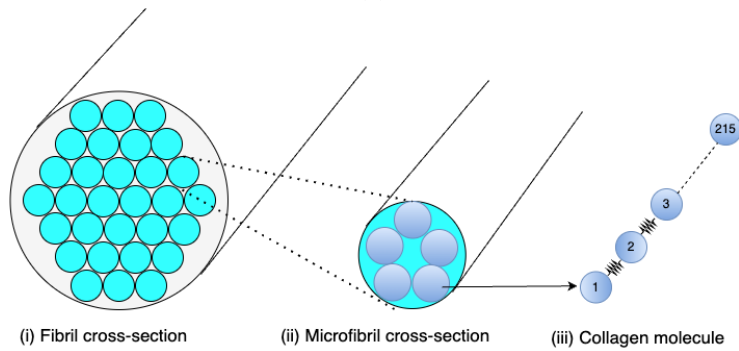
We first describe the geometric details of coarse-grained fibril model and how cross-links or sacrificial bonds that break and reform are incorporated into the model. The model is a modification of existing three dimensional coarse grained models for collagen fibrils in the literature [8,9].

A collagen molecule is represented by a linear bead-spring polymer of 217 beads, as shown in Fig. 4.1b(iii). The distance between two consecutive beads is  $b \approx 1.4$  nm. In a microfibril, five collagen molecules are arranged parallel to each other but in a staggered fashion longitudinally, as shown in Fig. 4.1a, and in a pentagonal geometry along transverse direction, as shown in Fig. 4.1b(ii). The diameter of a single microfibril is  $\approx 3.5$  nm. 37 of these microfibrils, arranged in hexagonal closed packing, represents a collagen fibril, as shown in Fig. 4.1b(i). The staggered arrangement of collagen molecules results in a repeating gap and overlap region which give rise to the characteristic D-period (67 nm) of the collagen fibril.

It is known that collagen molecules self-assemble into fibril structure and end regions of collagen molecules (called telopeptides) forms enzymatic cross-links with their neighboring molecules to further stabilize the structure. This indicates that the end regions must have a high affinity for specific regions on the collagen molecule in order for self assembly to result in fibril formation with a precise D period. In line with this concept, we consider three types of beads ( $E$ ,  $S$  and  $A$ ) in each collagen molecule, as shown in Fig. 4.1a. ‘ $E$ ’ (shown in red) represents the end beads of each collagen molecule, ‘ $S$ ’ (shown in blue)



(a)



(b)

Figure 4.1: (a) Schematic diagram showing the longitudinal arrangement of collagen molecules in a microfibril. Gap and overlap region represented by 'G' and 'O' respectively and D-period is shown by 'D'. (b) Cross-sectional view of the hierarchical structure of the fibril: (i) fibril, (ii) microfibril, and (iii) molecule.

represents the possible sites for cross-link formation ( $E$ - $S$  sacrificial bond) and ‘ $A$ ’ (not shown) represents the remaining atoms in each molecule. In our model, the location of potential cross-linking sites (‘ $S$ ’ beads) is chosen such that self-assembly could in principle lead to a fibril structure with a  $\approx 67$  nm ( $D$ ) periodicity, which is well accepted number for type I collagen fibrils. However, variations exist across tissues and collagen types, and uncertainties of the order of 2 nm have been reported in the value of  $D$ -period [105–107]. Based on this, the ratio of the  $D$ -period to the bond length ( $D/b$ ) is calculated to be approximately 48. Therefore, 48 bonds correspond to a single  $D$  period. In addition, the arrangement of collagen molecules in a microfibril indicates that the second, third, fourth, and fifth molecules are staggered by  $D$ ,  $2D$ ,  $3D$ , and  $4D$ , respectively. As a result, beads with indices 49, 97, 145, and 193 are classified as  $S$  type. We have also chosen the gap and overlap regions as  $G = O = 0.5D$ , which is equivalent to 24 bond lengths ( $b$ ). Consequently, beads with indices 25, 49, 73, 97, 121, 145, 169, and 193 in each collagen molecule are considered to be type  $S$ , as shown by the blue beads in Fig. 4.1a. Our choice of  $G = 0.5D$  is close to the experimental value of  $G \approx 0.54D$  [28, 33]. Our choice ensures the possibility of cross-linking sites being symmetric with respect to the two ends of the collagen molecules. Thus, self assembly of these molecules will automatically result in the well-known periodically staggered pattern of the molecules in a fibril. This choice of gap and overlap, however results in slightly higher value of peak stress as compared to the earlier simulations with different gap and overlap regions [8, 9].

#### 4.1.2 Interaction potential and parameters:

The interaction potentials and parameters closely follow that of Refs. [8, 9]. The interaction between all directly bonded beads including backbone of collagen molecules and the

cross-links is given by a biharmonic potential as:

$$F_{bond} = -\frac{\partial U_{bond}}{\partial r} = \begin{cases} k_{T0}(r - r_0), & r < r_1, \\ k_{T1}(r - r_0), & r_1 \leq r < r_{break}, \\ 0, & r > r_{break}. \end{cases} \quad (4.1)$$

where  $r_0$  is the equilibrium distance between two beads,  $r_1$  is the hypercritical distance,  $r_{break}$  is the bond-breaking distance and  $k_{T0}$  and  $k_{T1}$  are spring constants. The bending interaction between triplet of consecutive beads along the backbone of each collagen molecule is given by a bending potential:

$$U_\theta = \frac{1}{2}k_\theta(\theta - \theta_0)^2, \quad (4.2)$$

where  $k_\theta$  is bending strength and  $\theta_0$  is equilibrium angle. There is no bending interaction in triplets that includes the cross-linking beads (*S*-type). The interaction between all non-bonded beads is given by Lennard-Jones potential as:

$$U_{LJ} = 4\epsilon \left[ \left( \frac{\sigma}{r} \right)^{12} - \left( \frac{\sigma}{r} \right)^6 \right], \quad r < r_c = 2.5\sigma, \quad (4.3)$$

where  $r$  is the distance between beads,  $\epsilon$  is the strength of the potential (energy parameter),  $\sigma$  is the diameter of monomer and  $r_c$  is the cut-off distance. The numerical values of the different parameters are given in Table 3.1.

The interaction between all non-bonded beads is given by Lennard-Jones potential as:

$$U_{LJ} = 4\epsilon \left[ \left( \frac{\sigma}{r} \right)^{12} - \left( \frac{\sigma}{r} \right)^6 \right] \quad r_c = 2.5 \sigma, \quad (4.4)$$

where  $r$  is the distance between beads,  $\epsilon$  is the strength of the potential (energy parameter),  $\sigma$  is the diameter of monomer and  $r_c$  is the cut-off distance. The parameter details for all the described interactions is given in Table 3.1. These parameters were deter-

Table 4.1: The parameters for the coarse-grained MD-model of fibril.

Model parameters	Value
$\epsilon$ - LJ energy parameter (kcal mol <sup>-1</sup> )	6.87
$\sigma_1$ - LJ distance parameter for all non-bonded beads (except <i>E-S</i> pairs)(Å)	14.72
$\sigma_2$ - LJ distance parameter for <i>E-S</i> pairs (Å)	10.0
$\theta_0$ - Equilibrium bending angle (degree)	180
$k_\theta$ - Bending strength constant (kcal mol <sup>-1</sup> rad <sup>-2</sup> )	14.98
$r_0$ - Equilibrium distance (tropocollagen) [Å]	14.00
$r_1$ - critical hyperelastic distance (tropocollagen) [Å]	18.20
$r_{break}$ - bond breaking distance (tropocollagen)	21.00
$k_{T0}$ - Stretching strength constant (tropocollagen) [kcal mol <sup>-1</sup> Å <sup>-2</sup> ]	17.13
$k_{T1}$ - Stretching strength constant (tropocollagen) [kcal mol <sup>-1</sup> Å <sup>-2</sup> ]	97.66
$r_0$ - Equilibrium distance (divalent cross-link) [Å]	10.00
$r_1$ - critical hyperelastic distance (divalent cross-link) [Å]	12.00
$r_{break}$ - bond breaking distance (divalent cross-link) [Å]	14.68
$k_{T0}$ - Stretching strength constant (divalent cross-link) [kcal mol <sup>-1</sup> Å <sup>-2</sup> ]	0.20
$k_{T1}$ - Stretching strength constant (divalent cross-link) [kcal mol <sup>-1</sup> Å <sup>-2</sup> ]	41.84
$m$ - mass of tropocollagen bead [a.m.u]	1358.7

mined through all-atom simulations of a small collagen stretch using a bottom-up approach, considering crystallographic water and a skin of water around each tropocollagen molecule [78].

We utilized LAMMPS commands such as `fix bond/break` for bond breaking and `fix bond/react` for bond reformation. These commands are well-explained in the LAMMPS documentation [103]. In brief, when bonds break, the bonded interaction is turned off, and corresponding beads interact only with the LJ potential. The reverse is true for bond reformations.

To implement reformation, we consider ‘*E*’ and ‘*S*’ type atoms as special atoms. When a pair of ‘*E*’ and ‘*S*’ atoms approach closer than a certain distance say  $r'$ , a cross-link or bond can form between them, provided neither of the participating beads is part of any existing cross-link. Once a bond is formed, the new *E-S* bond is assigned the same parameters as those of a divalent cross-link. We set  $r' = 14\text{Å}$ , which is smaller than  $r_{break} = 14.68\text{Å}$  and LJ distance parameter for non-bonded *E-S* pairs to be ( $\sigma_2 = 10\text{Å}$ ). In earlier models [8, 9] LJ parameter ( $\sigma_1 = 14.72\text{Å}$ ) was the same for all non-bonded pairs.

If the  $E$ - $S$  bond had length  $\sigma_1$ , two non-bonded atoms will typically not come closer than  $\sigma_1 = 14.72\text{\AA}$ , which is larger than both the bond breaking distance ( $r_{break} = 14.68\text{\AA}$ ) for divalent cross-link and also  $r'$ . The equilibrium distance  $r_{min} = 2^{\frac{1}{6}}\sigma_1 = 16.52\text{\AA}$  is also greater than  $r_{break}$ . For bond reformation to take place, the distance between non-bonded  $E$ - $S$  pairs must be less than or equal to  $r'$ . With  $\sigma_2$ ,  $r_{min}$  is  $11.22\text{\AA}$ , allowing for the reformation of  $E$ - $S$  bonds.

### 4.1.3 Simulation protocol:

The simulation were performed using LAMMPS [103]. Time step was set to  $10\text{ fs}$ . The fibril model used in the simulations had an initial cross-link percentage of  $\beta$ , which indicates the fraction of end molecules that are cross-linked. Periodic boundary conditions with a box size of length  $(L + G)$  is used to mimic the fibril of infinite length with alternative gap and overlap regions, where  $L$  is length of collagen molecule. No explicit solvent has been considered during simulations. The system is first equilibrated for  $20\text{ ns}$  at zero pressure in the NPT ensemble with Nose-Hoover thermostat and barostat settings of  $298\text{ K}$  and  $0\text{ Pa}$ , respectively. The choice of NPT ensemble during equilibration is motivated by the fact that the fibril relaxation in the experiment was conducted at zero force. The relaxation times for the thermostat and barostat are fixed to  $1$  and  $10\text{ ps}$ . A constant strain rate of  $10^7\text{ s}^{-1}$  was then applied along fibril length, and the equations of motion were integrated with a Langevin thermostat using a drag coefficient of  $1\text{ ps}$ . For the cyclic loading simulation, the box was deformed up to a fixed strain ( $\lambda_{max}$ ) and then the direction of the applied strain rate was reversed to continue deformation until the force reached zero, which completed one loading cycle.

## 4.2 Results

### 4.2.1 Uniaxial and cyclic loading of fibril model with no-reformation:

We first examine the macroscopic behavior of the coarse-grained model and its dependence on the extent of cross-linking, under monotonically increasing applied strain. The box was subjected to a constant uniaxial strain rate of  $10^7 \text{ s}^{-1}$  along the longitudinal direction ( $z$ -axis). Initially, a fraction  $\beta$ , out of the maximum possible cross-links allowed, were created. For this analysis, cross-links, once broken, were not allowed to reform for benchmarking with earlier studies. The stress-strain response observed for different  $\beta$ , shown in Fig. 4.2, shows an initial linear behavior, followed by a non-linear regime, and a final sharp drop after peak stress. The initial linear regime is independent of  $\beta$ , while the non-linear regime, depending on  $\beta$ , shows a combination of hardening as well as softening regimes. When the extent of cross linking is large, the response is predominantly hardening, whereas for low extent of cross linking, it is predominantly softening. Further, we observe that for large strains, the stresses are independent of  $\beta$ . These observations are consistent with earlier results. We note that, for  $\beta < 100\%$ , the stress-strain response could depend on cross-linking configuration. We have chosen initial cross-linking configuration for each  $\beta$  randomly.

The key features of the macroscopic response can be better understood in terms of the number of the intact cross-links at any given strain (see Fig. 4.3). For small strains, the number of cross-links shows no noticeable change until the strain corresponding to peak load (see Fig. 4.2) is reached. Further deformation results in a sharp decrease in the number of intact cross-links which correlates well with the sharp decrease in the stresses seen earlier. For even larger deformations, the number of cross-links again do not noticeably change with strain, though the stationary values depend on the given  $\beta$ , even though the stresses were seen to be independent of  $\beta$  at these strains. This can be attributed to the

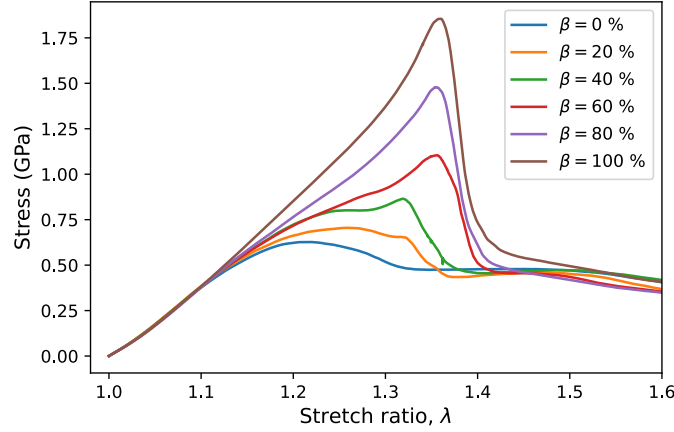


Figure 4.2: The stress-strain response of the collagen fibril model to applied uniaxial strain for different percentages of cross-links ( $\beta$ ) present. Data are averaged over 5 independent runs for each curve for same initial configurations.

resistance offered by the chains sliding past each other to be similar irrespective of the remaining intact cross-links.

We now examine the dissipative response of the fibril to cyclic loading for the case  $\beta = 100\%$ , when all the end atoms are cross-linked to a neighboring atom. We perform cyclic loading simulation with maximum stretch ratio  $\lambda_{\max} = 1.36$ , using the protocol described in Sec. 4.1.3. We choose this particular  $\lambda_{\max} = 1.36$  as it falls in the regime where cross-links are actively breaking (see Fig. 4.3). The fibril is subjected to 10 loading-unloading cycles as in the experiment of Ref. [7]. The stress-strain curves show the presence of dissipative hysteresis loops (see Fig 4.4) in which the maximum stress as well as dissipation per cycle changes with increasing number of cycles. Furthermore, a residual strain is observed consistent with experimental data. The associated hysteresis loops shift to the right with number of loading cycles showing accumulation of residual strain. These results reproduce features that were observed in cyclic loading experiment of fibrils [7].

To gain insight into the microscopic mechanism behind the features of the hysteresis loops in Fig. 4.4, we examine the associated time evolution of the number of cross-links, as shown in Fig. 4.5. During the initial cycles, a higher fraction of the cross-links break.

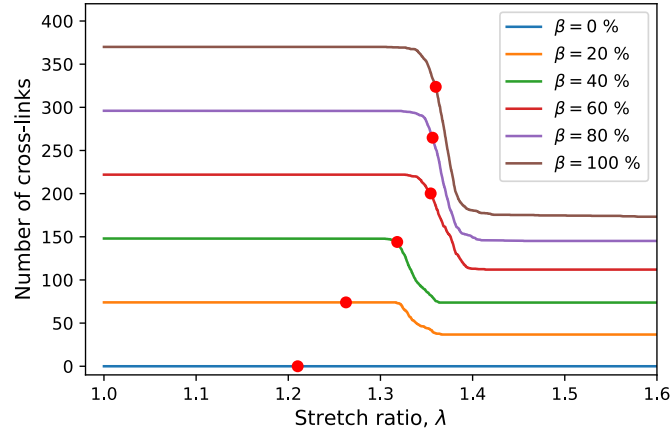


Figure 4.3: The number of cross-links at a given uniaxial strain for different percentages of cross-links ( $\beta$ ) present. The red dots represent stretch ratios corresponding to peak stress in Fig. 4.2. Data are averaged over 5 independent runs for each curve for same initial configurations.

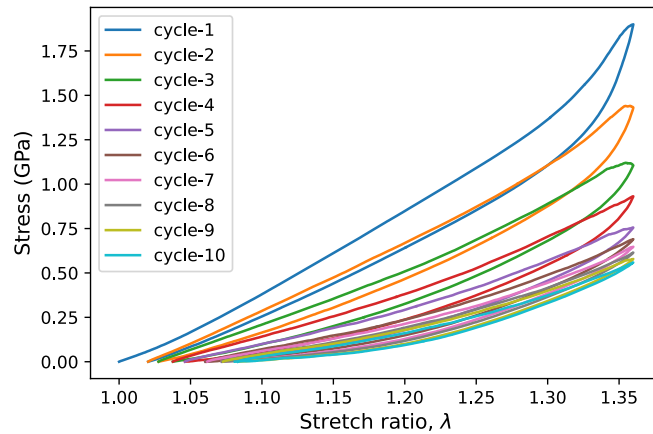


Figure 4.4: The stress-strain response of the collagen fibril model for strain controlled cyclic loading of a typical realization with  $\beta = 100\%$  and maximum stretch ratio  $\lambda_{\max} = 1.36$ .

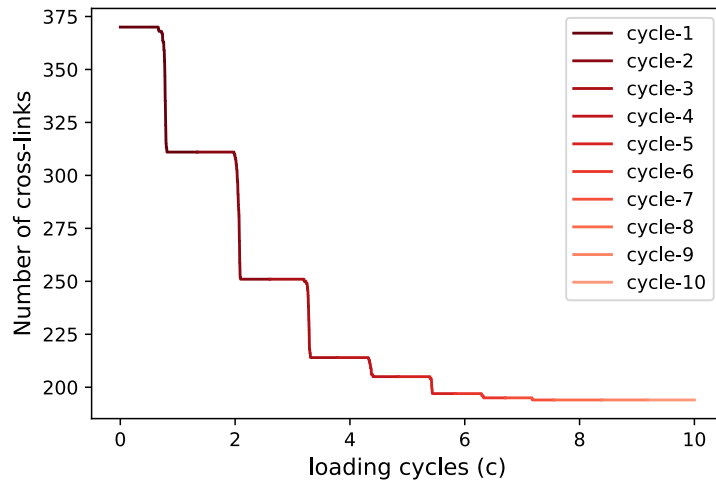


Figure 4.5: Time evolution of the number of cross-links under cyclic loading, corresponding to the stress-strain response shown earlier in Fig. 4.4.

However, as the number of cycles increases, the rate of cross-link breakage per cycle decreases. This trend continues till the number of cross-links eventually approaches a steady state. The observed lowering of peak stress as well as accumulation of residual strain in Fig. 4.4 appears to be a direct outcome of the rupturing of the cross-links which make the fibril more compliant.

We next quantify the time evolution of the characteristic parameters of the stress-strain response to cyclic loading. To do so, we obtain the mean value of the parameters by averaging over 10 realizations. As seen in the typical realization earlier, the average number of broken cross-links per cycle also decreases with increasing number of cycles (see Fig. 4.6). Further, the associated residual strain, shown in Fig. 4.7, exhibits a corresponding increase to a steady state value of  $\approx 10\%$  which falls within the range reported in experiment [7]. The dissipation, evaluated as the area of the hysteresis loop, is seen in Fig. 4.8 to have a marginal increase in the first two cycles before decreasing to a steady state value. The associated peak stress decreases monotonically with number of cycles to a steady state value, as seen in Fig. 4.9.

We now quantify the approach of the residual strain, energy dissipation, peak stress, and the number of broken cross-links per cycle to their corresponding steady-state values. As

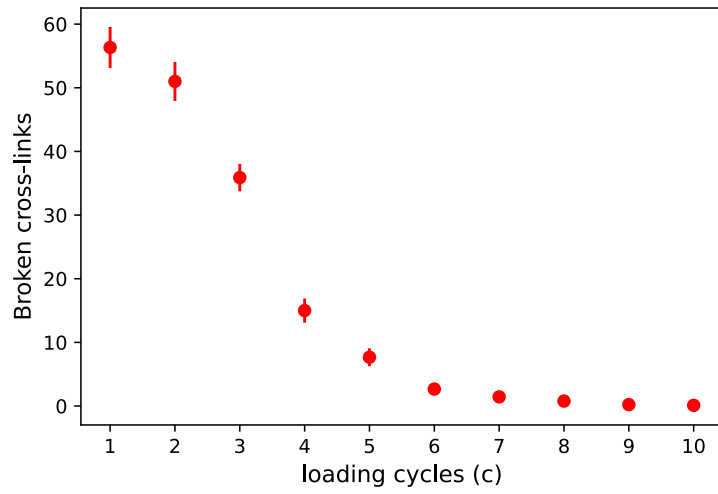


Figure 4.6: The average number of broken cross-links per cycle under cyclic loading, based on ten runs.

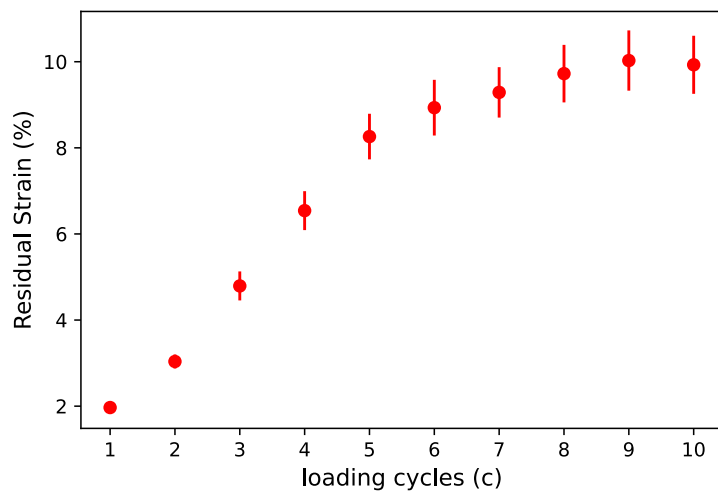


Figure 4.7: The evolution of residual strain with the number of loading cycles, averaged over ten runs.

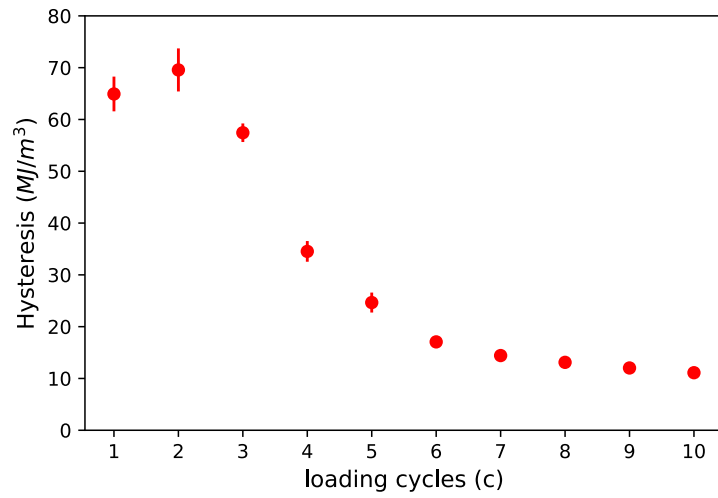


Figure 4.8: The evolution of energy dissipation with the number of loading cycles, averaged over ten runs.

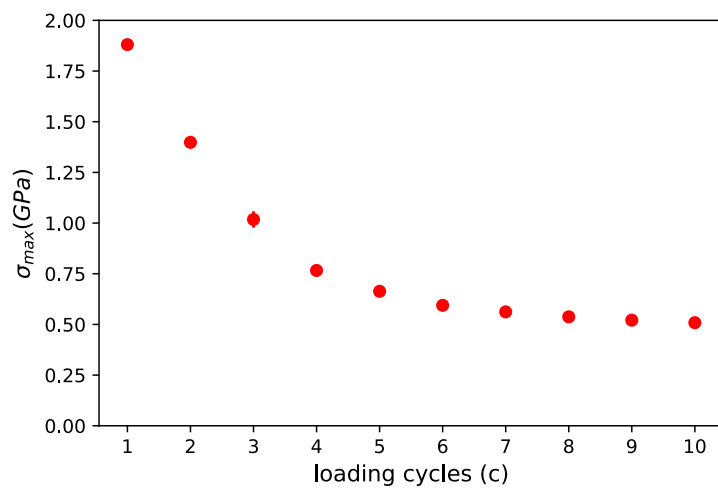


Figure 4.9: The variation of peak stress with the number of loading cycles, averaged over ten runs.

we found earlier for the kinetic model [97] and in the experimental data, we find that in the MD model too, the approach to the steady state is exponential with number of cycles  $c$  (see Appendix B).

$$q(c) - q(\infty) \propto e^{-c/c^*}, \quad (4.5)$$

where  $q(c)$  represents the value of the relevant parameter after  $c$  cycles. This allow us to extract the characteristic cycle number  $c^*$ . The value of  $c^*$  is only weakly dependent on the choice of parameter for fixed  $\lambda_{\max}$  (see Appendix B).

The characteristic cycle number  $c^*$  depends on the choice of  $\lambda_{\max}$ , as can be seen from Fig. 4.10 where  $c^*$  extracted from  $\sigma_{\max}$ , residual strain and dissipation are shown. If  $\lambda_{\max}$  is close to the lower boundary of the region of stretches when cross-links break, then value of  $c^*$  is relatively high. As  $\lambda_{\max}$  is increased and lies within the range when cross-links break, then  $c^*$  becomes independent of  $\lambda_{\max}$  and is approximately 5. The dependence of  $c^*$  on  $\lambda_{\max}$  is also compared with that seen for kinetic model with sacrificial bonds [97] and experimental data in Fig. 4.10. We note that the ranges of stretches were different for kinetic model and experiment, and we have done a linear extrapolation to make the ranges coincide. We conclude that the results of MD are in good agreement with that of kinetic model as well as experiment.

We further examine the dependence of  $c^*$  on the extent of cross-linking  $\beta$ , as shown in Fig. 4.11. We choose  $\lambda_{\max} = 1.345$  for which  $c^*$  is relatively high for  $\beta = 100\%$ . Cross-links are removed to achieve the desired  $\beta$ . When  $\beta$  is decreased,  $c^*$  quickly decreases to a  $\beta$ -independent value which coincides with the value of  $c^*$  for  $\beta = 100\%$  but higher  $\lambda_{\max}$ . This result can be understood by the rationale that while  $\lambda_{\max} = 1.345$  results in rupturing of only few cross-links for  $\beta = 100\%$ , it lies well within the range of stretch ratios where significant number of cross-links break for smaller  $\beta$ .

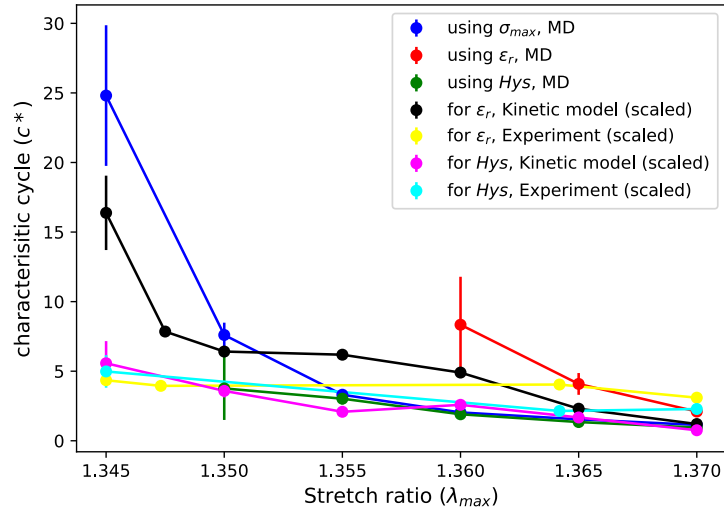


Figure 4.10: The variation of characteristic cycle,  $c^*$  with the maximum stretch,  $\lambda_{\max}$ . For the MD model,  $c^*$  extracted from  $\sigma_{\max}$ , residual strain and dissipation are shown. The stretch ratios for the kinetic model data and experimental data have been rescaled and are as reported in Ref. [97].

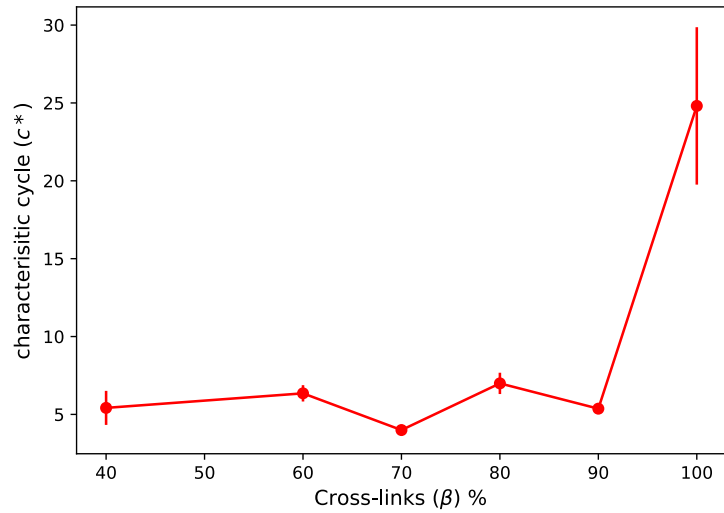
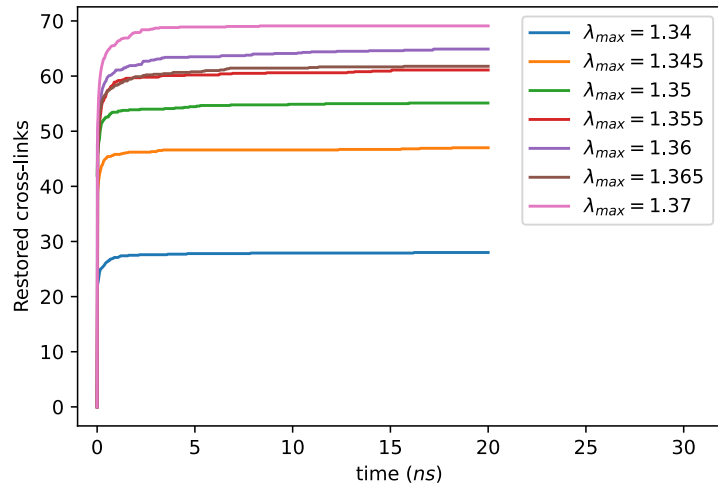


Figure 4.11: The variation of characteristic cycle,  $c^*$ , extracted from  $\sigma_{\max}$ , with the cross-link percentage,  $\beta$ , for  $\lambda_{\max} = 1.345$ .

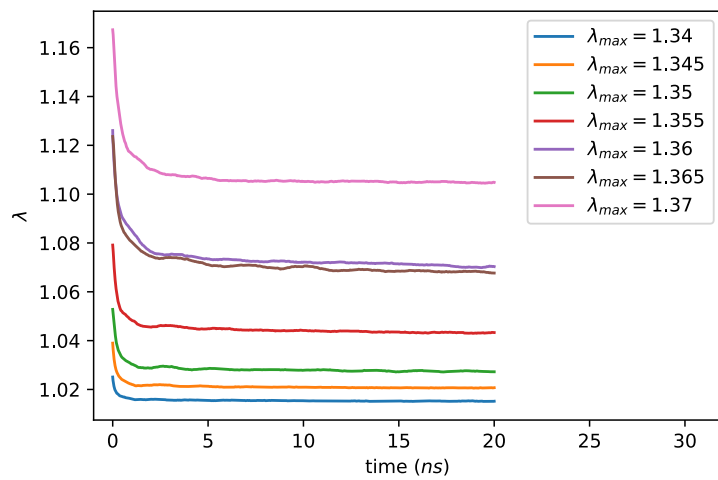
## 4.2.2 Role of cross-link reformation on fibril recovery

Having characterized the dissipation caused by cyclic loading, we now focus on the recovery when the fibril is allowed to relax at zero force after 10 cycles. Any pair of  $E$  and  $S$  atoms that approach less than a distance  $r' = 14\text{\AA}$  form a cross-link instantaneously, provided neither atom is already part of any cross-link. The number of cross-links that reform increase with time till they saturate while the associated stretch ratio decrease with time to a steady state value, as can be seen in Fig. 4.12(a) and (b) respectively. The saturation value of number of reformed cross-links increase with  $\lambda_{\max}$  while that of residual strain decrease with  $\lambda_{\max}$ . We find that the recovery in strain is approximately 50% for all  $\lambda_{\max}$ . This is comparable with the recovery seen in the experiment. We note that we could have introduced a time scale into the reformation process by associating a finite rate for the formation of cross-links. However, we find that saturation values are independent of the reformation rate. In the data shown in Fig. 4.12, we set reformation rate to infinity as it is not practical to simulate relaxation for 60 minutes as in the experiment.

To investigate the role of cross-link reformation on the macroscopic response of the fibril, we compare the following two cases. In case 1, the fibril is directly subjected to monotonic loading after 10 cycles. In case 2, after 10 cycles, we equilibrated the system for  $20\text{ns}$  at zero force and then subjected it to monotonic loading. During the equilibration process, the cross-links were allowed to reform. We find that after relaxation (case 2), the fibril shows increased strength and toughness (see Fig 4.13). The difference in peak stress and toughness between the two cases become more significant as the maximum strain,  $\lambda_{\max}$ , is increased. This can be attributed to the fact that at higher  $\lambda_{\max}$ , a larger number of cross-links are broken during the initial cyclic loading, resulting in more available free ends for cross-link reformation and recovery. It is important to note that while there is an increase in strength and toughness after the relaxation process, it does not exceed the original strength and toughness of the undamaged fibril. This observation indicates the presence of permanent plastic deformation resulting from cyclic loading, and it suggests



(a)



(b)

Figure 4.12: Time evolution of (a) number of cross-links and (b) stretch ratio for during relaxation at zero force after 10 cycles for different  $\lambda_{max}$ .

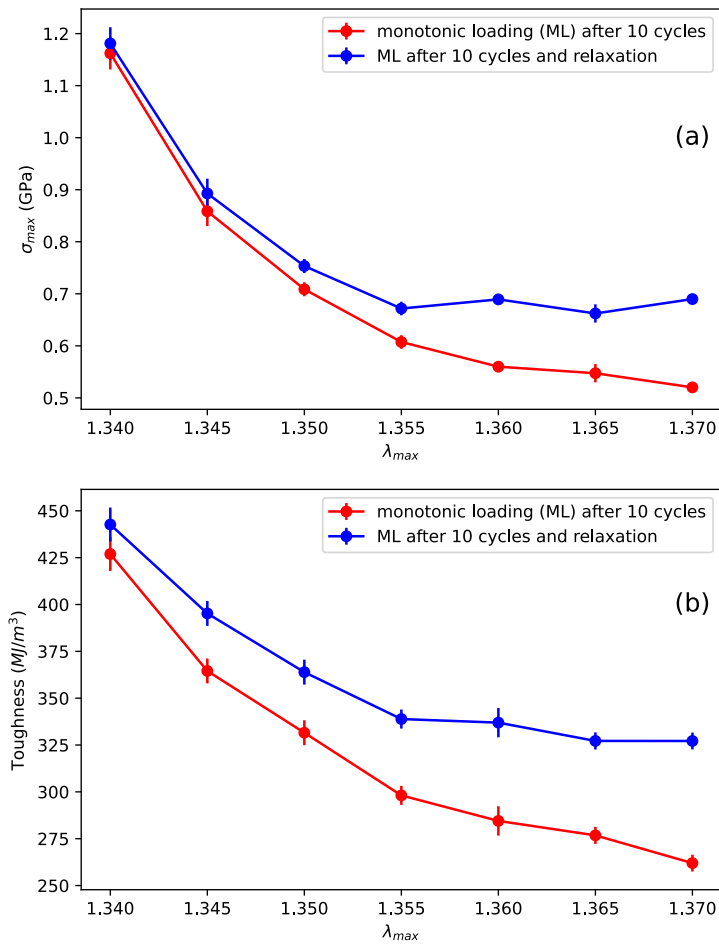


Figure 4.13: Comparison of (a) peak stress,  $\sigma_{max}$  and (b) toughness of a fibril subjected to monotonic loading with and without relaxation after being loaded for 10 cycles. Cross-links reform during the relaxation process.

that full recovery is not achievable within the framework of current model.

Similar features – improved characteristic parameters after relaxation – can be seen for both residual strain and total number of cross-links, as shown in Fig. 4.14. The change is more significant for larger  $\lambda_{max}$ .

### 4.3 Discussion and Conclusions

Collagen, a widely present biomaterial, is of great importance, but there is currently less research focusing on fatigue experimental studies of individual collagen fibrils [7, 52, 55]

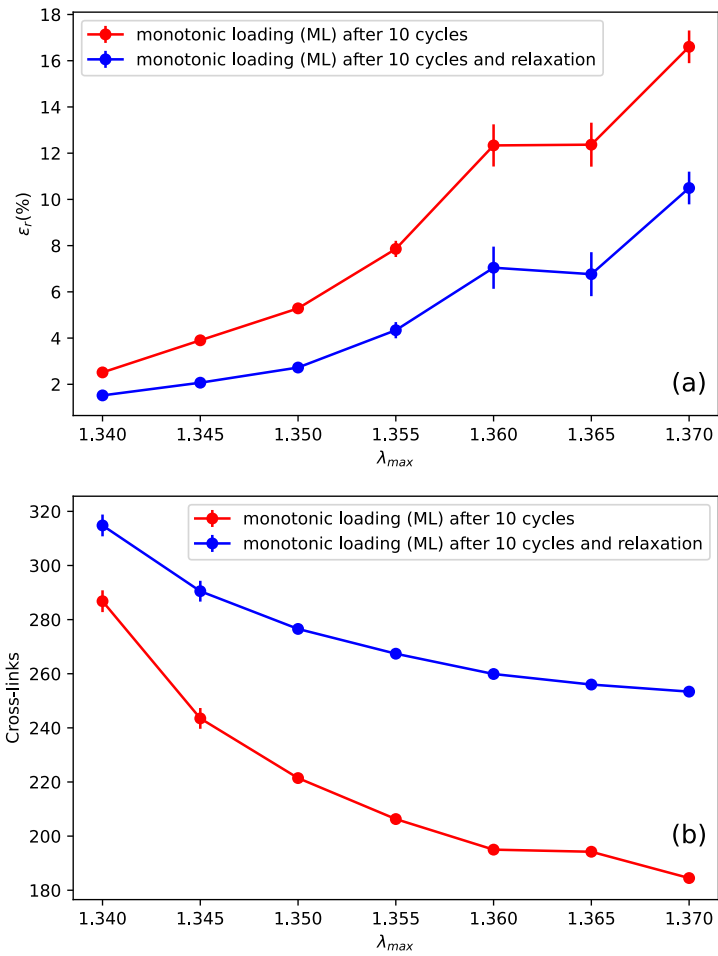


Figure 4.14: Comparison of (a) residual strain (b) total number of cross-links of a fibril subjected to monotonic loading with and without relaxation after being loaded for 10 cycles. Cross-links reform during the relaxation process.

when compared to the number of experiments on monotonic loading. In this paper, with emphasis on the experiment by Liu et. al [7], we studied the dissipation and recovery of a collagen fibril when subjected to cyclic loads using molecular dynamics simulations of coarse grained models. Existing models for collagen fibrils, that have been obtained by coarse graining atomistic models, were earlier able to reproduce the macroscopic response to monotonic loading. Here, we incorporated reformation of cross-links or sacrificial bonds that aids in recovery. We show that the simulations reproduce key features of the cyclic loading experiment of Ref. [7] such as moving hysteresis loops, residual strains, partial recovery on relaxation etc, and their dependence on different stretch ratios. The material parameters after relaxation were shown improve with relaxation bringing out the role of extent of cross-linking in determining the macroscopic response.

The different parameters of the macroscopic response, such as peak stress, residual strain, dissipation, and number of cross-links approach the steady state values exponentially fast, characterized by a characteristic cycle number  $c^*$ . This behavior is consistent with what was observed in the analysis of the kinetic model [97] as well as seen in the experiment [7]. We found that the  $c^*$ , becomes independent of the  $\lambda_{\max}$ , approximately equal to 5, when  $\lambda_{\max}$  lies within the regions where cross-links break, while it remains high at the lower boundary of this region. This observation is further supported by the dependence of  $c^*$  on cross-link density  $\beta$ . Further, the value of  $c^* \approx 5$  is same as that obtained for the kinetic model as well as in the experiment.

We investigated the post-cyclic loading recovery of the fibril model by allowing the fibril to relax and permitting cross-links to reform during the relaxation process. We observe  $\approx 50\%$  recovery in residual strain across different stretch ratios, comparable with the results of the experiment [7]. We do not find full recovery, thus there is plastic deformation. This is because, during relaxation at zero force, cross-links form between the closest possible cross-linking sites, thereby often arresting further decrease in strain. Additionally, the remaining free ends do not reach the reformation sites due to their interaction with

other beads. The plastic deformation is consistent with the viscoelastic-plastic continuum modeling approach of Ref. [11], as well as the experimental results [7], but differs from the results for the kinetic model [97] where full recovery occurs if the fibril is relaxed for infinite time. This is because the kinetic model is a minimal model that does not account for the complex geometrical structure of the collagen fibril.

The molecular dynamics model also reproduce additional features that are absent in kinetic models. The non-zero steady state hysteresis loops seen in experiments are well-reproduced in our simulations of the MD model, but absent in the existing kinetic models, where the steady state value of hysteresis approaches zero. This can be attributed to the realistic time-delays inherent in the MD model, but absent in the kinetic models.

To study the effect of cross-link reformation during relaxation, we compared the response to monotonic loading of two fibrils: one was subjected to monotonic loading immediately after cyclic loading, while the other was relaxed and then subjected to monotonic loading. We observed an increase in strength and toughness in the fibril that underwent relaxation compared to the other one. However, this increase did not exceed the strength of the undamaged fibril under monotonic loading. This gain in strength, compared to no relaxation, is as in the viscoelastic-plastic model [11]. However, in the experiment of Liu et al. [7], the fibril that was directly subjected to monotonic loading immediately after cyclic loading, without relaxation, exhibited an increase in strength compared to the original fibril. This aspect is not reproduced neither in our molecular dynamics simulations, nor in the viscoelastic-plastic model [11] or kinetic model [97]. Understanding this phenomenon within models is a promising area for future study. We note that in kinetic models for collagen molecules [10], an increase in the peak force with relaxation was observed due to restoration of more sacrificial bonds. However, the comparison of peak force is done with a configuration that has no sacrificial bonds. Within the MD model considered in this paper, one possible mechanism of increasing strength of fibrils subjected to cyclic loading is to allow reformation of cross-links during loading. This may allow for re-organisation

of cross-links that is optimised for withstanding larger strains, thus increasing strength. Understanding the phenomenon of increased strength post cyclic loading, within models, is a promising area for future study.

We also note that energy dissipation can show an increasing behavior with the loading cycles if the cyclic loading is done for small stretches ( $\lambda_{\max}$ ), within the range where cross-links break. For example, energy dissipation increases until 3 cycles for  $\lambda_{\max} = 1.35$  before exhibiting an exponential decline (see Appendix C).

In the MD model, the range of stretch ratio ( $\lambda_{\max}$ ) in which cross-links break is relatively narrow compared to both the kinetic model [97] and the experimental observations [7]. The majority of cross-links break within the range  $\lambda_{\max} \approx 1.34 - 1.37$ . In contrast, the kinetic model has a wider range for bond breaking, which is comparable to the experiment. This difference is due to the stochastic nature of the kinetic model where cross-links can break at different strain thresholds. In contrast, the cross-links in the MD model break at the same strain thresholds resulting in a narrower range of stretch ratios.

For the reformation, we could have introduced a new time scale in the form of rate of reformation. In the current study, we used an infinite rate, that is two atoms that are closer than the minimum distance form a bond instantaneously. Inclusion of a finite rate would slow down the reformation rate, but we have checked that the final number of cross-links is largely independent of this rate. Given that the relaxation times scale in the experiment is order of 60 minutes, our approach is justifiable provided we only analyze the steady state values and not the time-dependence.

The MD model that we studied has some limitations. Even though the MD model takes into account the three dimensional structure of the collagen fibril, it is still a simplification of the complex collagen fibril and its mechanics which also depends on several environmental factors like hydration etc. The parameters of these models are derived from atomistic simulation of small stretch of the collagen molecules with few bounded water molecules. The difference in parameters could arise because of intrinsic hetero-

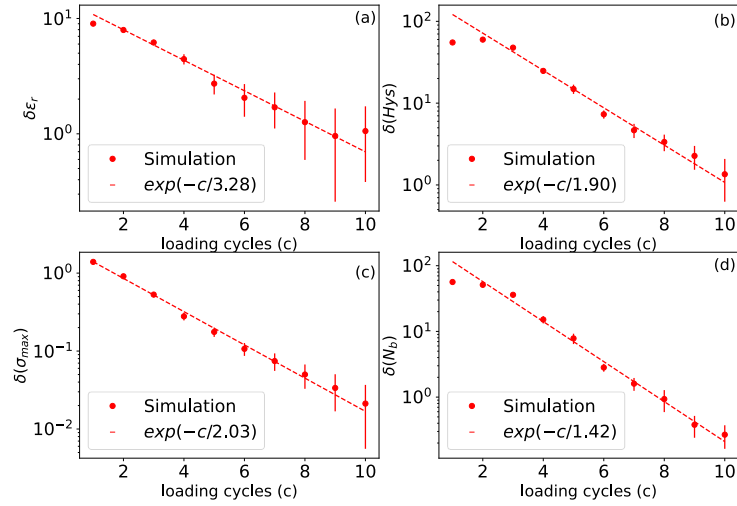


Figure 4.15: The (a) residual strain, (b) hysteresis, (c) peak stress and (d) number of broken bonds per cycle approach their respective steady state values exponentially fast. The data are for  $\lambda_{\max} = 1.36$ .

genercity of the collagen molecule itself. Further, the stress-strain response and hence the value of the  $c^*$  could depend on the distribution of the cross-link for  $\beta < 100\%$ . One could do the same analysis done in this paper including trivalent cross-links and combination of trivalent and divalent cross-links and/or Advanced Glycation Endproduct cross-links, which occur as a result of aging and diabetes [79].

## Appendix B: Approach of the characteristic parameters to steady state

We find that the differences of residual strain, energy dissipation, peak stress, and broken bonds per cycle from their steady state values decrease exponentially to zero with the number of loading cycles, as can be seen in Fig. 4.15.

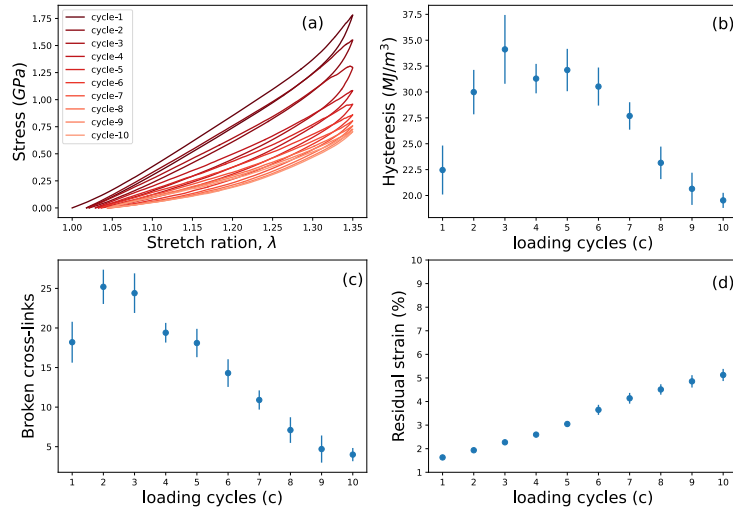


Figure 4.16: (a) The stress strain response (b) evolution of energy dissipation and (c) number of broken cross-links per cycle (d) residual strain under cyclic loading for  $\lambda_{max} = 1.35$ .

## Appendix C: Non-monotonic response for $\lambda_{max} = 1.35$

During cyclic loading, it is possible that hysteresis as well as number of cross-links can show a non-monotonic behaviour with cycle number, i.e., increasing for a few cycles before decaying exponentially to the steady state. This happens for smaller values of values of  $\lambda_{max}$  which are closer to lower boundary of the bond breaking regime. An example can be seen in Fig. 4.16, where the data for  $\lambda_{max} = 1.35$  is shown. As described in the main text, the initial transient behaviour disappears as  $\lambda_{max}$  is increased. However, residual strain shows monotonically increasing behaviour with the number of loading cycles for all values of  $\lambda_{max}$ .

# Chapter 5

## Conclusions

This thesis aims to comprehensively model and understand the mechanical response of individual collagen fibrils under cyclic loading. Collagen holds immense significance as a widely present biomaterial in living organisms. Experimentally, the stress-stretch response of a single collagen fibril subject to cyclic loading within a fixed stretch ratio  $\lambda$  is known to show moving hysteresis loops and residual strains that increase and saturate with number of cycles. The fibril is known to show recovery in energy dissipation as well as residual strains on relaxation. These features were thought to be related to the presence of sacrificial bonds within the fibril. Furthermore, the cyclically loaded fibrils exhibited greater strength and toughness compared to fibrils subjected to monotonic loading. This enhancement was believed to be due to permanent molecular rearrangements, although the specific mechanism behind these improvements was not fully understood.

In the first part of this thesis (Chapert-3), we develop a kinetic model for a collagen fibril incorporating presence of hidden loops and stochastic fragmentation as well as reformation of sacrificial bonds. We show that the model reproduces well the characteristic features of reported experimental data on cyclic response of collagen fibrils, such as moving hysteresis loops, time evolution of residual strains and energy dissipation, recovery on relaxation, etc. We show that the breaking of sacrificial bonds leads to hysteresis (energy

dissipation) and the release of hidden lengths, results in residual strain. The spontaneous formation and breaking of sacrificial bonds at zero force is a possible healing mechanism within the collagen fibril. We show that the approach to the steady state is controlled by a characteristic cycle number for both residual strain as well as energy dissipation, and is in good agreement with reported existing experimental data.

In the second part of this thesis (Chapter-4), we approach the same problem from microscopic point of view. We modify an existing coarse grained molecular dynamics model for collagen fibril with initially cross-linked collagen molecules by incorporating reformation of cross-links and evaluate its potential to explain possible recovery on relaxation and increased strength resulting from reformation and re-organization of cross-links. Using molecular dynamics simulations, we show that our model successfully replicates the key features observed in experimental data, including the movement of hysteresis loops, the time evolution of residual strains and energy dissipation, as well as the recovery observed during relaxation. It also explains the non-zero steady-state hysteresis and plastic deformation observed in the experiment. We also show that the characteristic cycle number, describing the approach towards steady state, has a value similar to that in experiments. We also emphasize the vital role of the degree of cross-linking on the key features of the macroscopic response to cyclic loading. We showed an increase in strength and toughness in the fibril that underwent relaxation after cyclic loading compared to the other one, which was not relaxed.

The kinetic model presented in the first part of the thesis is a minimal model without a specific geometry, yet it remarkably captures the essential physics, accurately representing observed experimental features. It yields a crucial quantity, the characteristic cycle number  $c^*$ , which is further validated by experimental results and a more detailed MD model (based on the full three-dimensional structure of the fibril) described in the second part of the thesis. The existence of this characteristic cycle number holds significance in understanding the time-dependent cyclic response of collagen. In particular, it has

the potential of being utilised for comparing fibril responses across various factors, such as animals, ages, disease stages, hierarchical levels, responses to medication, etc. This presents a promising area for future experimental investigations.

Furthermore, it is worth considering that the stress-strain response of the fibril, and consequently the value of  $c^*$ , might be influenced by the distribution of cross-links. A similar analysis using the MD model, as demonstrated in the second part of the thesis, could be conducted by incorporating various types of cross-links, such as trivalent cross-links, a combination of trivalent and divalent cross-links, and Advanced Glycation Endproducts (AGEs) cross-links that occur due to aging and diabetes. Exploring the impact of different cross-link distributions could provide valuable insights into how these structural variations affect the mechanical behavior of collagen fibrils.

The models described in this thesis primarily focus on simulating the immediate mechanical response of collagen fibrils to cyclic loading. It does not take into account the long-term effects of prolonged stress that could be due to aging or disease progression. To cover these aspects more comprehensively in the future, the models could include factors like biochemical changes, how sacrificial bond dynamics change over time, and potential structural modifications in collagen fibrils due to prolonged stress. At the level of the kinetic model, this should involve including time-dependent rates as well as macroscopic laws, and structural modification could be introduced at the level of the MD model. As biological tissues are living materials, it will also be important to consider active interactions, coupled physics, the role of water and fluids, and piezoelectric effects. These extensions of the models might be crucial for applications in biomedical research, particularly contributing to our understanding of disease progression and the development of therapeutic strategies.

Overall, the work presented in this thesis not only proposes future directions for experiments but also significantly contributes to the current understanding of the fundamental mechanical behaviour of collagen fibrils under cyclic loading. Additionally, it suggests

several avenues to extend the proposed models, which could lead to interesting and valuable results. The study opens up exciting possibilities for further research in the field of collagen mechanics and sheds light on offering valuable insights that could contribute to advancements in biomaterials and medical applications, particularly in understanding tissue mechanics and disease-related alterations.

# Bibliography

- [1] P. Fratzl, “Collagen: Structure and mechanics, an introduction.” *Springer:New York* (2008) .
- [2] K. E. Kadler, C. Baldock, J. Bella, and R. P. Boot-Handford, “Collagens at a glance,” *Journal of cell science* **120** no. 12, (2007) 1955–1958.
- [3] S. Bose, S. Li, E. Mele, and V. V. Silberschmidt, “Exploring the mechanical properties and performance of type-i collagen at various length scales: A progress report,” *Materials* **15** no. 8, (2022) 2753.
- [4] E. Rezvani Ghomi, N. Nourbakhsh, M. Akbari Kenari, M. Zare, and S. Ramakrishna, “Collagen-based biomaterials for biomedical applications,” *Journal of Biomedical Materials Research Part B: Applied Biomaterials* **109** no. 12, (2021) 1986–1999.
- [5] J. B. Thompson, J. H. Kindt, B. Drake, H. G. Hansma, D. E. Morse, and P. K. Hansma, “Bone indentation recovery time correlates with bond reforming time,” *Nature* **414** no. 6865, (2001) 773–776.
- [6] J. P. Orgel, T. J. Wess, and A. Miller, “The in situ conformation and axial location of the intermolecular cross-linked non-helical telopeptides of type i collagen,” *Structure* **8** no. 2, (2000) 137–142.
- [7] J. Liu, D. Das, F. Yang, A. G. Schwartz, G. M. Genin, S. Thomopoulos, and I. Chasiotis, “Energy dissipation in mammalian collagen fibrils: Cyclic

- strain-induced damping, toughening, and strengthening,” *Acta biomaterialia* **80** (2018) 217–227.
- [8] B. Depalle, Z. Qin, S. J. Shefelbine, and M. J. Buehler, “Influence of cross-link structure, density and mechanical properties in the mesoscale deformation mechanisms of collagen fibrils,” *Journal of the mechanical behavior of biomedical materials* **52** (2015) 1–13.
- [9] D. C. Malaspina, I. Szleifer, and Y. Dhaher, “Mechanical properties of a collagen fibril under simulated degradation,” *Journal of the mechanical behavior of biomedical materials* **75** (2017) 549–557.
- [10] C. K. Lieou, A. E. Elbanna, and J. M. Carlson, “Sacrificial bonds and hidden length in biomaterials: A kinetic constitutive description of strength and toughness in bone,” *Physical Review E* **88** no. 1, (2013) 012703.
- [11] F. F. Fontenele and N. Bouklas, “Understanding the inelastic response of collagen fibrils: A viscoelastic-plastic constitutive model,” *Acta Biomaterialia* **163** (2023) 78–90.
- [12] S. Ricard-Blum, “The collagen family,” *Cold Spring Harbor perspectives in biology* **3** no. 1, (2011) a004978.
- [13] R. Parenteau-Bareil, R. Gauvin, and F. Berthod, “Collagen-based biomaterials for tissue engineering applications,” *Materials* **3** no. 3, (2010) 1863–1887.
- [14] M. D. Shoulders and R. T. Raines, “Collagen structure and stability,” *Annual review of biochemistry* **78** (2009) 929–958.
- [15] M. Karsdal, *Biochemistry of collagens, laminins and elastin: structure, function and biomarkers*. Academic Press, 2019.
- [16] M. Wu, K. Cronin, and J. S. Crane, “Biochemistry, collagen synthesis,”

- [17] I. N. Amirrah, Y. Lokanathan, I. Zulkiflee, M. M. R. Wee, A. Motta, and M. B. Fauzi, “A comprehensive review on collagen type i development of biomaterials for tissue engineering: From biosynthesis to bioscaffold,” *Biomedicines* **10** no. 9, (2022) 2307.
- [18] J. Jokinen, E. Dadu, P. Nykvist, J. Kapyla, D. J. White, J. Ivaska, P. Vehvilainen, H. Reunanen, H. Larjava, L. Hakkinen, *et al.*, “Integrin-mediated cell adhesion to type i collagen fibrils,” *Journal of Biological Chemistry* **279** no. 30, (2004) 31956–31963.
- [19] E. Hadjipanayi, V. Mudera, and R. A. Brown, “Guiding cell migration in 3d: a collagen matrix with graded directional stiffness,” *Cell motility and the cytoskeleton* **66** no. 3, (2009) 121–128.
- [20] X. Liu, X. Long, W. Liu, Y. Zhao, T. Hayashi, M. Yamato, K. Mizuno, H. Fujisaki, S. Hattori, S.-i. Tashiro, *et al.*, “Type i collagen induces mesenchymal cell differentiation into myofibroblasts through yap-induced tgf- $\beta$ 1 activation,” *Biochimie* **150** (2018) 110–130.
- [21] E. Brauer, E. Lippens, O. Klein, G. Nebrich, S. Schreivogel, G. Korus, G. N. Duda, and A. Petersen, “Collagen fibrils mechanically contribute to tissue contraction in an in vitro wound healing scenario,” *Advanced Science* **6** no. 9, (2019) 1801780.
- [22] A. Gautieri, S. Vesentini, A. Redaelli, and M. J. Buehler, “Single molecule effects of osteogenesis imperfecta mutations in tropocollagen protein domains,” *Protein Science* **18** no. 1, (2009) 161–168.
- [23] O. Andriotis, S. Chang, M. Vanleene, P. Howarth, D. Davies, S. Shefelbine, M. Buehler, and P. Thurner, “Structure–mechanics relationships of collagen fibrils in the osteogenesis imperfecta mouse model,” *Journal of The Royal Society Interface* **12** no. 111, (2015) 20150701.

- [24] R. Dalgleish, “The human type i collagen mutation database,” *Nucleic acids research* **25** no. 1, (1997) 181–187.
- [25] H. Kuivaniemi, G. Tromp, and D. J. Prockop, “Mutations in collagen genes: causes of rare and some common diseases in humans,” *The FASEB journal* **5** no. 7, (1991) 2052–2060.
- [26] W. Yang, M. A. Meyers, and R. O. Ritchie, “Structural architectures with toughening mechanisms in nature: a review of the materials science of type-i collagenous materials,” *Progress in Materials Science* **103** (2019) 425–483.
- [27] N. F. Huang, T. S. Zaitseva, and M. V. Paukshto, “Biomedical applications of collagen,” 2023.
- [28] A. Gautieri, S. Vesentini, A. Redaelli, and M. J. Buehler, “Hierarchical structure and nanomechanics of collagen microfibrils from the atomistic scale up,” *Nano letters* **11** no. 2, (2011) 757–766.
- [29] A. V. Persikov, J. A. Ramshaw, A. Kirkpatrick, and B. Brodsky, “Amino acid propensities for the collagen triple-helix,” *Biochemistry* **39** no. 48, (2000) 14960–14967.
- [30] A. V. Persikov, J. A. Ramshaw, A. Kirkpatrick, and B. Brodsky, “Electrostatic interactions involving lysine make major contributions to collagen triple-helix stability,” *Biochemistry* **44** no. 5, (2005) 1414–1422.
- [31] T. J. Wess, A. Hammersley, L. Wess, and A. Miller, “A consensus model for molecular packing of type i collagen,” *Journal of structural biology* **122** no. 1-2, (1998) 92–100.
- [32] T. J. Wess, A. Hammersley, L. Wess, and A. Miller, “Molecular packing of type i collagen in tendon,” *Journal of molecular biology* **275** no. 2, (1998) 255–267.

- [33] J. A. Petruska and A. J. Hodge, "A subunit model for the tropocollagen macromolecule," *Proceedings of the National Academy of Sciences of the United States of America* **51** no. 5, (1964) 871.
- [34] J. Smith, "Molecular pattern in native collagen," *Nature* **219** no. 5150, (1968) 157–158.
- [35] D. M. Darvish, "Collagen fibril formation in vitro: From origin to opportunities," *Materials Today Bio* **15** (2022) 100322.
- [36] L. Knott and A. J. Bailey, "Collagen cross-links in mineralizing tissues: a review of their chemistry, function, and clinical relevance," *Bone* **22** no. 3, (1998) 181–187.
- [37] M. L. Tanzer, "Intermolecular cross-links in reconstituted collagen fibrils: evidence for the nature of the covalent bonds," *Journal of Biological Chemistry* **243** no. 15, (1968) 4045–4054.
- [38] N. Light and A. Bailey, "The chemistry of the collagen cross-links. purification and characterization of cross-linked polymeric peptide material from mature collagen containing unknown amino acids," *Biochemical Journal* **185** no. 2, (1980) 373–381.
- [39] A. J. Bailey, R. G. Paul, and L. Knott, "Mechanisms of maturation and ageing of collagen," *Mechanisms of ageing and development* **106** no. 1-2, (1998) 1–56.
- [40] J. P. Orgel, T. C. Irving, A. Miller, and T. J. Wess, "Microfibrillar structure of type i collagen in situ," *Proceedings of the National Academy of Sciences* **103** no. 24, (2006) 9001–9005.
- [41] S. G. Uzel and M. J. Buehler, "Molecular structure, mechanical behavior and failure mechanism of the c-terminal cross-link domain in type i collagen," *Journal of the Mechanical Behavior of Biomedical Materials* **4** no. 2, (2011) 153–161.

- [42] P. Kannus, "Structure of the tendon connective tissue," *Scandinavian journal of medicine & science in sports* **10** no. 6, (2000) 312–320.
- [43] Y. Liu, D. Luo, and T. Wang, "Hierarchical structures of bone and bioinspired bone tissue engineering," *Small* **12** no. 34, (2016) 4611–4632.
- [44] D. M. Maurice, "The structure and transparency of the cornea," *The Journal of physiology* **136** no. 2, (1957) 263.
- [45] C. Boote, S. Dennis, R. H. Newton, H. Puri, and K. M. Meek, "Collagen fibrils appear more closely packed in the prepupillary cornea: optical and biomechanical implications," *Investigative ophthalmology & visual science* **44** no. 7, (2003) 2941–2948.
- [46] Y.-L. Sun, Z.-P. Luo, A. Fertala, and K.-N. An, "Direct quantification of the flexibility of type i collagen monomer," *Biochemical and biophysical research communications* **295** no. 2, (2002) 382–386.
- [47] Y.-L. Sun, Z.-P. Luo, A. Fertala, and K.-N. An, "Stretching type ii collagen with optical tweezers," *Journal of biomechanics* **37** no. 11, (2004) 1665–1669.
- [48] L. Bozec and M. Horton, "Topography and mechanical properties of single molecules of type i collagen using atomic force microscopy," *Biophysical journal* **88** no. 6, (2005) 4223–4231.
- [49] T. Gutschmann, G. E. Fantner, J. H. Kindt, M. Venturoni, S. Danielsen, and P. K. Hansma, "Force spectroscopy of collagen fibers to investigate their mechanical properties and structural organization," *Biophysical journal* **86** no. 5, (2004) 3186–3193.
- [50] R. B. Svensson, H. Mulder, V. Kovanen, and S. P. Magnusson, "Fracture mechanics of collagen fibrils: influence of natural cross-links," *Biophysical journal* **104** no. 11, (2013) 2476–2484.

- [51] R. B. Svensson, T. Hassenkam, C. A. Grant, and S. P. Magnusson, “Tensile properties of human collagen fibrils and fascicles are insensitive to environmental salts,” *Biophysical journal* **99** no. 12, (2010) 4020–4027.
- [52] R. B. Svensson, T. Hassenkam, P. Hansen, and S. P. Magnusson, “Viscoelastic behavior of discrete human collagen fibrils,” *Journal of the Mechanical Behavior of Biomedical Materials* **3** no. 1, (2010) 112–115.
- [53] S. Eppell, B. Smith, H. Kahn, and R. Ballarini, “Nano measurements with micro-devices: mechanical properties of hydrated collagen fibrils,” *Journal of the Royal Society Interface* **3** no. 6, (2006) 117–121.
- [54] Z. L. Shen, M. R. Dodge, H. Kahn, R. Ballarini, and S. J. Eppell, “In vitro fracture testing of submicron diameter collagen fibril specimens,” *Biophysical journal* **99** no. 6, (2010) 1986–1995.
- [55] Z. L. Shen, M. R. Dodge, H. Kahn, R. Ballarini, and S. J. Eppell, “Stress-strain experiments on individual collagen fibrils,” *Biophysical journal* **95** no. 8, (2008) 3956–3963.
- [56] C. A. Grant, D. J. Brockwell, S. E. Radford, and N. H. Thomson, “Effects of hydration on the mechanical response of individual collagen fibrils,” *Applied Physics Letters* **92** no. 23, (2008) .
- [57] C. A. Grant, D. J. Brockwell, S. E. Radford, and N. H. Thomson, “Tuning the elastic modulus of hydrated collagen fibrils,” *Biophysical journal* **97** no. 11, (2009) 2985–2992.
- [58] A. Gautieri, A. Redaelli, M. J. Buehler, and S. Vesentini, “Age-and diabetes-related nonenzymatic crosslinks in collagen fibrils: candidate amino acids involved in advanced glycation end-products,” *Matrix Biology* **34** (2014) 89–95.

- [59] A. J. Bailey, “Molecular mechanisms of ageing in connective tissues,” *Mechanisms of ageing and development* **122** no. 7, (2001) 735–755.
- [60] E. A. Zimmermann, E. Schaible, H. Bale, H. D. Barth, S. Y. Tang, P. Reichert, B. Busse, T. Alliston, J. W. Ager III, and R. O. Ritchie, “Age-related changes in the plasticity and toughness of human cortical bone at multiple length scales,” *Proceedings of the National Academy of Sciences* **108** no. 35, (2011) 14416–14421.
- [61] G. Fessel, Y. Li, V. Diederich, M. Guizar-Sicairos, P. Schneider, D. R. Sell, V. M. Monnier, and J. G. Snedeker, “Advanced glycation end-products reduce collagen molecular sliding to affect collagen fibril damage mechanisms but not stiffness,” *PloS one* **9** no. 11, (2014) e110948.
- [62] A. Gautieri, F. S. Passini, U. Silván, M. Guizar-Sicairos, G. Carimati, P. Volpi, M. Moretti, H. Schoenhuber, A. Redaelli, M. Berli, *et al.*, “Advanced glycation end-products: Mechanics of aged collagen from molecule to tissue,” *Matrix Biology* **59** (2017) 95–108.
- [63] A. C. Lorenzo and E. R. Caffarena, “Elastic properties, young’s modulus determination and structural stability of the tropocollagen molecule: a computational study by steered molecular dynamics,” *Journal of biomechanics* **38** no. 7, (2005) 1527–1533.
- [64] S. Vesentini, C. F. Fitié, F. M. Montecchi, and A. Redaelli, “Molecular assessment of the elastic properties of collagen-like homotrimer sequences,” *Biomechanics and modeling in mechanobiology* **3** (2005) 224–234.
- [65] M. J. Buehler, “Nature designs tough collagen: explaining the nanostructure of collagen fibrils,” *Proceedings of the National Academy of Sciences* **103** no. 33, (2006) 12285–12290.

- [66] M. J. Buehler, “Nanomechanics of collagen fibrils under varying cross-link densities: atomistic and continuum studies,” *Journal of the mechanical behavior of biomedical materials* **1** no. 1, (2008) 59–67.
- [67] A. Gautieri, M. J. Buehler, and A. Redaelli, “Deformation rate controls elasticity and unfolding pathway of single tropocollagen molecules,” *Journal of the Mechanical Behavior of Biomedical Materials* **2** no. 2, (2009) 130–137.
- [68] A. Gautieri, S. Vesentini, A. Redaelli, and M. J. Buehler, “Viscoelastic properties of model segments of collagen molecules,” *Matrix Biology* **31** no. 2, (2012) 141–149.
- [69] M. J. Buehler and S. Y. Wong, “Entropic elasticity controls nanomechanics of single tropocollagen molecules,” *Biophysical journal* **93** no. 1, (2007) 37–43.
- [70] S. M. Pradhan, D. R. Katti, and K. S. Katti, “Steered molecular dynamics study of mechanical response of full length and short collagen molecules,” *Journal of nanomechanics and micromechanics* **1** no. 3, (2011) 104–110.
- [71] Z. Zhou, M. Minary-Jolandan, and D. Qian, “A simulation study on the significant nanomechanical heterogeneous properties of collagen,” *Biomechanics and modeling in mechanobiology* **14** (2015) 445–457.
- [72] M. Tang, T. Li, N. S. Gandhi, K. Burrage, and Y. Gu, “Heterogeneous nanomechanical properties of type i collagen in longitudinal direction,” *Biomechanics and modeling in mechanobiology* **16** (2017) 1023–1033.
- [73] I. Streeter and N. H. de Leeuw, “Atomistic modeling of collagen proteins in their fibrillar environment,” *The Journal of Physical Chemistry B* **114** no. 41, (2010) 13263–13270.

- [74] A. K. Nair, A. Gautieri, S.-W. Chang, and M. J. Buehler, “Molecular mechanics of mineralized collagen fibrils in bone,” *Nature communications* **4** no. 1, (2013) 1724.
- [75] M. Fielder and A. K. Nair, “Effects of hydration and mineralization on the deformation mechanisms of collagen fibrils in bone at the nanoscale,” *Biomechanics and modeling in mechanobiology* **18** (2019) 57–68.
- [76] A. E. Elbanna and J. M. Carlson, “Dynamics of polymer molecules with sacrificial bond and hidden length systems: towards a physically-based mesoscopic constitutive law,” *PloS one* **8** no. 4, (2013) e56118.
- [77] M. J. Buehler, “Nanomechanics of collagen fibrils under varying cross-link densities: atomistic and continuum studies,” *Journal of the mechanical behavior of biomedical materials* **1** no. 1, (2008) 59–67.
- [78] M. J. Buehler, “Atomistic and continuum modeling of mechanical properties of collagen: elasticity, fracture, and self-assembly,” *Journal of Materials Research* **21** no. 8, (2006) 1947–1961.
- [79] J. Kamml, C.-Y. Ke, C. Acevedo, and D. S. Kammer, “The influence of ages and enzymatic cross-links on the mechanical properties of collagen fibrils,” *journal of the mechanical behavior of biomedical materials* **143** (2023) 105870.
- [80] B. Depalle, Z. Qin, S. J. Shefelbine, and M. J. Buehler, “Large deformation mechanisms, plasticity, and failure of an individual collagen fibril with different mineral content,” *Journal of Bone and Mineral Research* **31** no. 2, (2016) 380–390.
- [81] M. Tavakol and T. J. Vaughan, “A coarse-grained molecular dynamics investigation of the role of mineral arrangement on the mechanical properties of mineralized collagen fibrils,” *Journal of the Royal Society Interface* **20** no. 198, (2023) 20220803.

- [82] J. A. Van Der Rijt, K. O. Van Der Werf, M. L. Bennink, P. J. Dijkstra, and J. Feijen, “Micromechanical testing of individual collagen fibrils,” *Macromolecular bioscience* **6** no. 9, (2006) 697–702.
- [83] T. L. Sellaro, D. Hildebrand, Q. Lu, N. Vyavahare, M. Scott, and M. S. Sacks, “Effects of collagen fiber orientation on the response of biologically derived soft tissue biomaterials to cyclic loading,” *Journal of Biomedical Materials Research Part A: An Official Journal of The Society for Biomaterials, The Japanese Society for Biomaterials, and The Australian Society for Biomaterials and the Korean Society for Biomaterials* **80** no. 1, (2007) 194–205.
- [84] S. P. Veres, J. M. Harrison, and J. M. Lee, “Repeated subrupture overload causes progression of nanoscaled discrete plasticity damage in tendon collagen fibrils,” *Journal of Orthopaedic Research* **31** no. 5, (2013) 731–737.
- [85] S. P. Veres, J. M. Harrison, and J. M. Lee, “Cross-link stabilization does not affect the response of collagen molecules, fibrils, or tendons to tensile overload,” *Journal of Orthopaedic Research* **31** no. 12, (2013) 1907–1913.
- [86] S. Bose, S. Li, E. Mele, and V. V. Silberschmidt, “Dry vs. wet: Properties and performance of collagen films. part ii. cyclic and time-dependent behaviours,” *Journal of the mechanical behavior of biomedical materials* **112** (2020) 104040.
- [87] M. E. Susilo, J. A. Paten, E. A. Sander, T. D. Nguyen, and J. W. Ruberti, “Collagen network strengthening following cyclic tensile loading,” *Interface focus* **6** no. 1, (2016) 20150088.
- [88] M. Milazzo, G. S. Jung, S. Danti, and M. J. Buehler, “Wave propagation and energy dissipation in collagen molecules,” *ACS Biomaterials Science & Engineering* **6** no. 3, (2020) 1367–1374.
- [89] M. Milazzo, G. S. Jung, S. Danti, and M. J. Buehler, “Mechanics of mineralized collagen fibrils upon transient loads,” *ACS nano* **14** no. 7, (2020) 8307–8316.

- [90] J. L. Zitnay, G. S. Jung, A. H. Lin, Z. Qin, Y. Li, S. M. Yu, M. J. Buehler, and J. A. Weiss, “Accumulation of collagen molecular unfolding is the mechanism of cyclic fatigue damage and failure in collagenous tissues,” *Science advances* **6** no. 35, (2020) eaba2795.
- [91] M. P. Allen and D. J. Tildesley, *Computer simulation of liquids*. Oxford university press, 2017.
- [92] A. P. J. Jansen, *An introduction to kinetic Monte Carlo simulations of surface reactions*, vol. 856. Springer, 2012.
- [93] A. F. Voter, “Introduction to the kinetic monte carlo method,” in *Radiation effects in solids*, pp. 1–23. Springer, 2007.
- [94] L. Verlet, “Computer" experiments" on classical fluids. i. thermodynamical properties of lennard-jones molecules,” *Physical review* **159** no. 1, (1967) 98.
- [95] S. Nosé, “A unified formulation of the constant temperature molecular dynamics methods,” *The Journal of chemical physics* **81** no. 1, (1984) 511–519.
- [96] W. G. Hoover, “Canonical dynamics: Equilibrium phase-space distributions,” *Physical review A* **31** no. 3, (1985) 1695.
- [97] A. Suhail, A. Banerjee, and R. Rajesh, “Kinetic model description of dissipation and recovery in collagen fibrils under cyclic loading,” *Physical Review E* **106** no. 4, (2022) 044407.
- [98] M. Rief, M. Gautel, F. Oesterhelt, J. M. Fernandez, and H. E. Gaub, “Reversible unfolding of individual titin immunoglobulin domains by afm,” *science* **276** no. 5315, (1997) 1109–1112.
- [99] M. Rief, J. M. Fernandez, and H. E. Gaub, “Elastically coupled two-level systems as a model for biopolymer extensibility,” *Physical Review Letters* **81** no. 21, (1998) 4764.

- [100] T. Su and P. K. Purohit, “Mechanics of forced unfolding of proteins,” *Acta biomaterialia* **5** no. 6, (2009) 1855–1863.
- [101] G. I. Bell, “Models for the specific adhesion of cells to cells: a theoretical framework for adhesion mediated by reversible bonds between cell surface molecules.” *Science* **200** no. 4342, (1978) 618–627.
- [102] K. Linka and M. Itskov, “Mechanics of collagen fibrils: A two-scale discrete damage model,” *Journal of the mechanical behavior of biomedical materials* **58** (2016) 163–172.
- [103] S. Plimpton, “Fast parallel algorithms for short-range molecular dynamics,” *Journal of computational physics* **117** no. 1, (1995) 1–19.
- [104] A. Suhail, A. Banerjee, and R. Rajesh, “Dissipation and recovery in collagen fibrils under cyclic loading: a molecular dynamics study,” *arXiv preprint arXiv:2307.13465* (2023) .
- [105] A. Stylianou, “Assessing collagen d-band periodicity with atomic force microscopy,” *Materials* **15** no. 4, (2022) 1608.
- [106] H.-N. Su, L.-Y. Ran, Z.-H. Chen, Q.-L. Qin, M. Shi, X.-Y. Song, X.-L. Chen, Y.-Z. Zhang, and B.-B. Xie, “The ultrastructure of type i collagen at nanoscale: large or small d-spacing distribution?” *Nanoscale* **6** no. 14, (2014) 8134–8139.
- [107] B. Erickson, M. Fang, J. M. Wallace, B. G. Orr, C. M. Les, and M. M. Banaszak Holl, “Nanoscale structure of type i collagen fibrils: quantitative measurement of d-spacing,” *Biotechnology journal* **8** no. 1, (2013) 117–126.